Advancing Organized Convection Representation in the Unified Model: Implementing and Enhancing Multiscale Coherent Structure Parameterization

Zhixiao Zhang[1], Hannah Christensen[1], Mark Muetzelfeldt[2], Tim Woollings[1], Robert Stephen Plant[2], Alison Stirling[3], Michael Whitall[4], Mitchell W Moncrieff[5], Chih-Chieh Chen[6], and Zhe Feng[7]

[1]University of Oxford
[2]University of Reading
[3]UK Met Office
[4]Met Office
[5]National Center for Atmospheric Research (UCAR)
[6]NCAR CGD
[7]Pacific Northwest National Laboratory (DOE)

April 16, 2024

Abstract

To address the effect of stratiform latent heating on meso- to large scale circulations, an enhanced implementation of the Multiscale Coherent Structure Parameterization (MCSP) is developed for the Met Office Unified Model. MCSP represents the top-heavy stratiform latent heating from under-resolved organized convection in general circulation models. We couple the MCSP with a mass-flux convection scheme (CoMorph-A) to improve storm lifecycle continuity. The improved MCSP trigger is specifically designed for mixed-phase deep convective cloud, combined with a background vertical wind shear, both known to be crucial for stratiform development. We also test a cloud top temperature dependent convective-stratiform heating partitioning, in contrast to the earlier fixed partitioning. Assessments from ensemble weather forecasts and decadal simulations demonstrate that MCSP directly reduces cloud deepening and precipitation areas by moderating mesoscale circulations. Indirectly, it amends tropical precipitation biases, notably correcting dry and wet biases over India and the Indian Ocean, respectively. Remarkably, the scheme outperforms a climate model ensemble by improving seasonal precipitation cycle predictions in these regions. This enhancement is partly due to the scheme's refinement of Madden-Julian Oscillation (MJO) spectra, achieving better alignment with reanalysis data by intensifying MJO events and maintaining their eastward propagation after passing the Maritime Continent. However, the scheme also increases precipitation overestimation over the Western Pacific. Shifting from fixed to temperature-dependent convective-stratiform partitioning reduces the Pacific precipitation overestimation but also lessens the improvements of seasonal cycle in India. Spatially correlated biases highlight the necessity for advancements beyond deterministic approaches to align MCSP with environmental conditions.

Advancing Organized Convection Representation in the Unified Model: Implementing and Enhancing Multiscale Coherent Structure Parameterization

Zhixiao Zhang[1], Hannah M. Christensen[1], Mark R. Muetzelfeldt[2], Tim Woollings[1], Robert S. Plant[2], Alison J. Stirling[3], Michael A. Whitall[3], Mitchell W. Moncrieff[4], Chih-Chieh Chen[4], and Zhe Feng[5]

[1]Department of Physics, University of Oxford, Oxford, Oxfordshire, UK.

[2]Department of Meteorology, University of Reading, Reading, Berkshire, UK.

[3]Met Office, Exeter, Devon, UK.

[4]Climate and Global Dynamics Division, National Center for Atmospheric Research, Boulder, Colorado, USA.

[5]Atmospheric, Climate, and Earth Sciences Division, Pacific Northwest National Laboratory, Richland, Washington, USA.

Corresponding author: Zhixiao Zhang (zhixiao.zhang@physics.ox.ac.uk)

Key Points:

- Organized convection scheme with realistic triggering and state-dependent partitioning between stratiform and convective heating is proposed
- Scheme leads to reduced storm area and shallower parameterized convection through lower-troposphere cooling from stratiform precipitation
- Scheme corrects systematic precipitation biases over India and the Indian Ocean through intensifying the Madden-Julian Oscillation

Abstract

To address the effect of stratiform latent heating on meso- to large scale circulations, an enhanced implementation of the Multiscale Coherent Structure Parameterization (MCSP) is developed for the Met Office Unified Model. MCSP represents the top-heavy stratiform latent heating from under-resolved organized convection in general circulation models. We couple the MCSP with a mass-flux convection scheme (CoMorph-A) to improve storm lifecycle continuity. The improved MCSP trigger is specifically designed for mixed-phase deep convective cloud, combined with a background vertical wind shear, both known to be crucial for stratiform development. We also test a cloud top temperature dependent convective-stratiform heating partitioning, in contrast to the earlier fixed partitioning. Assessments from ensemble weather forecasts and decadal simulations demonstrate that MCSP directly reduces cloud deepening and precipitation areas by moderating mesoscale circulations. Indirectly, it amends tropical precipitation biases, notably correcting dry and wet biases over India and the Indian Ocean, respectively. Remarkably, the scheme outperforms a climate model ensemble by improving seasonal precipitation cycle predictions in these regions. This enhancement is partly due to the scheme's refinement of Madden-Julian Oscillation (MJO) spectra, achieving better alignment with reanalysis data by intensifying MJO events and maintaining their eastward propagation after passing the Maritime Continent. However, the scheme also increases precipitation overestimation over the Western Pacific. Shifting from fixed to temperature-dependent convective-stratiform partitioning reduces the Pacific precipitation overestimation but also lessens the improvements of seasonal cycle in India. Spatially correlated biases highlight the necessity for advancements beyond deterministic approaches to align MCSP with environmental conditions.

Plain Language Summary

We improve a key component of the Met Office's climate model to better represent how widespread light rain in severe convective storms affects atmospheric patterns. We make the representation respond to different temperatures at the tops of clouds, which is a new approach compared to previous studies where the heavy-to-light rain partitioning was assumed constant. We find that the improved representation of the light rain associated with severe storms reduces the overall storm rainfall area and suppresses storm height. The changes are particularly effective in correcting rainfall forecasts in tropical regions like India and the Indian Ocean, outperforming other climate models. Notably, our model excels at predicting specific tropical climate patterns, enhancing wind and rainfall accuracy over the Maritime Continent. However, our model predicts too much rain over the Western Pacific. When we adjust how we calculate the heavy-to-light rain partitioning based on cloud top temperatures, it reduces this overestimation but also weakens our improvements elsewhere. This indicates that we need to keep exploring new approaches to consider the light rain probability in severe storms.

1 Introduction

Organized convection encompasses two distinct types of precipitation: intense convective precipitation, and quasi-steady, lighter stratiform precipitation, with this differentiation observed in both tropical (Cheng & Houze, 1979) and extratropical regions (Houze et al., 1990). The variation in organized convection, encompassing a spectral mix rather than a simple spatial separation between convective and stratiform precipitation, presents a significant challenge in weather and climate prediction (Schumacher & Rasmussen, 2020), as these precipitation types

differ substantially in redistributing moisture, momentum, and heat in the atmosphere (Houze, 2004). One representative type of organized convection is a Mesoscale Convective System (MCS), which has a length scale exceeding 100 km in at least one direction (Houze 2004).

A fundamental distinction lies in the vertical profile of latent heating. In convective regions, intense updrafts induce rapid condensation, resulting in a bottom-heavy heating profile marked by a concentration of heating in the lower and middle troposphere (Houze, 1989). Conversely, in stratiform regions, the majority of latent heating occurs higher up, usually in the upper troposphere above the freezing level (Houze, 1989). This heating aloft is predominantly driven by the deposition of vapor into ice, a process facilitated by ice hydrometeors transported from convective regions (Han et al., 2019). Additionally, most stratiform regions exhibit net latent cooling below the freezing level, resulting from weaker updrafts and reduced local condensate production. This leads to insufficient condensational heating in the lower troposphere to counteract cooling from microphysical processes such as ice melting and raindrop evaporation (Leary & Houze, 1979). These dynamical and microphysical processes collectively lead to a top-heavy heating profile in stratiform regions (Houze, 1989; Schumacher et al., 2004).

A higher ratio of stratiform to convective partitioning leads to more top-heavy latent heating, crucially reshaping large-scale atmospheric circulations (Houze, 2018). For example, satellite observations show a sharp increase in stratiform precipitation and its associated top-heavy latent heating during the active stage of the Madden-Julian Oscillation (MJO) over the Western Pacific (Barnes et al., 2015). The spatial variability of the El Niño-Southern Oscillation (ENSO) is significantly influenced by the gradient of the stratiform fraction over the Pacific (Schumacher et al., 2004). Additionally, a greater stratiform fraction aids the propagation of large-scale waves from the tropics to extra-tropical regions, a phenomenon also highlighted in the same study. Incorporating stratiform latent heating in simulations notably elevates the center of the Walker cell, enhancing its alignment with observations (Hartmann et al., 1984). Overall, the more top-heavy the latent heating profile is, the stronger the upscaling feedback becomes from organized convection to large-scale atmospheric circulations (Houze, 2018).

However, it is difficult to represent top-heavy stratiform heating in weather and climate models due to its dependence on multiscale processes (Schumacher & Rasmussen, 2020), ranging from microphysics and convective drafts to mesoscale and large-scale circulations. Climate models with coarse resolution utilizing convection parameterizations often fail to represent mesoscale circulations within organized convection (Kooperman et al., 2015). Convection-permitting models with computational grids of a few kilometers partially represent mesoscale circulations yet tend to overestimate convective precipitation (e.g., Becker et al. 2021) and updraft intensity (Varble et al., 2014), and underestimate stratiform fractions (Prein et al., 2020). Specifically, overly-intense updrafts are too efficient in producing rimed ice and precipitating moisture in convective regions, resulting in fewer ice hydrometers aloft for feeding stratiform precipitation (Varble et al., 2014; Zhang et al., 2021). Even when model grid spacings reach large-eddy resolutions, the overestimation in the partitioning of convective and stratiform precipitation persists (Zhang et al., 2024). This indicates that improving stratiform precipitation representation requires more than just better resolved dynamics. Effective representation demands a coherent paradigm that spans multiple scales.

To mitigate such biases, a promising strategy developed in past studies (Chen et al., 2021; Moncrieff, 2019; Moncrieff et al., 2017; Moncrieff & Liu, 2006) is the Multiscale Coherent Structure Parameterization (MCSP). This scheme posits that the stratiform heating aloft

and lower-level cooling are directly proportional to the column-integrated convective heating estimated by a convection parameterization. The scheme is typically triggered in situations where the grid-scale winds promote slantwise layer overturning, which favors the partially-resolved organization of convection for generating stratiform latent heating (Moncrieff & Liu, 2006). Incorporating top-heavy latent heating profiles associated with organized convection through the MCSP scheme enhances the capability of general circulation models to simulate the observed MJO, as evidenced by studies from Chen et al. (2021) and Moncrieff et al. (2017) for the E3SM and CAM models respectively. Moreover, the MCSP scheme contributes to an improvement in the representation of Kelvin wave spectra and a reduction in biases associated with tropical precipitation (Chen et al., 2021).

The coupling method between convection parameterization and the MCSP scheme presents opportunities for improvement. The recent implementation of MCSP by Moncrieff et al. (2017) employs the Zhang-McFarlane convection scheme (Zhang & McFarlane, 1995), using a rate of change of Convective Available Potential Energy (CAPE) threshold as the trigger for the convection scheme. However, this CAPE-based trigger can be disrupted by the introduction of stratiform aloft heating and lower-level cooling by MCSP. Such disruption may compromise the temporal continuity of both the convection and MCSP schemes, possibly leading to intermittent or on-off behavior for either or both schemes. In addition, shallower convective systems, especially those at or below the freezing level that do not efficiently produce ice hydrometeors for stratiform precipitation, might not be associated with MCS, such that the MCSP scheme is inappropriately triggered for those cases. An improvement is needed to specifically target those deep convective systems that efficiently produce stratiform components for coupling with the MCSP scheme.

A second limitation with previous implementations of MCSP is the partitioning between stratiform and convective heating. Past studies have assumed a fixed partitioning (e.g., 50%) between stratiform and convective heating. However, this does not necessarily reflect real-world conditions, where the influence of stratiform precipitation can vary significantly due to the melting of ice hydrometeors from convection regions. A suitably-varying stratiform to convective heating partitioning could offer a more realistic representation.

Aiming to progress beyond existing methods, this research is guided by the following objectives: 1) Couple the MCSP with advanced convection parameterization techniques to improve storm-lifecycle continuity and facilitate storm-track based assessment. 2) Tailor MCSP triggering conditions specifically for deep convection. 3) Develop an environmentally-conditioned partitioning to effectively relate stratiform and convective heating processes. 4) Understand the scheme's direct effect in weather simulations spanning several days as well as its indirect effect in decadal simulations.

This study is carried out in the Met Office Unified Model, focusing on general circulation scales and is conducted as part of the Mesoscale Convective Systems: PRobabilistic forecasting and upscale IMpacts in the grey zonE (MCS: PRIME) project. The scheme, referred to as PRIME-MCSP, couples to a novel mass-flux convection scheme (CoMorph-A) that explicitly parameterizes convective detrainment and entrainment and smoothly transits between shallow and deep clouds (Whitall et al., 2022; Daleu et al., 2023; Lavender et al., 2024). A valuable feature of the CoMorph-A convection scheme for the current study is that it makes use of an implicit solver for its detrainment calculations. This contrasts with many other convection schemes, which can suffer from numerical overshoots and on-off behavior at the timestep level.

Moreover, CoMorph allows convection to be initiated from any layer in the vertical, depending on the instability at each level. At least partly for these reasons, the CoMorph-A approach enhances temporal-spatial continuity of precipitation clusters, capturing storm lifecycles in the presence of the stratiform heating aloft and lower-level cooling introduced by PRIME-MCSP. This improved continuity is crucial for enabling storm tracking, facilitating the lifecycle analysis of PRIME-MCSP's effect on the internal cloud dynamics and the surrounding environments.

To evaluate the effectiveness of PRIME-MCSP, short-term weather ensemble simulations and decadal climate simulations on a global scale are both conducted. The structure of the remaining sections is as follows: Section 2 details the design of the PRIME-MCSP scheme; Section 3 describes the simulations, observations, and methodology for storm tracking; Section 4 presents an analysis of the PRIME-MCSP impact throughout the lifecycle of MCSs using short-term ensemble runs; Section 5 examines the long-term climatic impacts of the PRIME-MCSP on large-scale precipitation patterns and the MJO in decadal simulations; and Section 6 summarizes the conclusions drawn from these analyses.

2 Parameterization Scheme

The PRIME-MCSP parameterization is designed to represent the stratiform latent heating profile associated with an MCS, which is otherwise missing in models. Drawing from Moncrieff et al. (2017), Figure 1a depicts a schematic of a slantwise layer overturning pattern of wind, highlighted by the black streamlines. Additionally, the schematic shows the vertical shear of horizontal wind via straight vectors on the right, indicating a transition from westerly winds in the lower troposphere to easterly winds in the mid-troposphere. Affected by this vertical wind shear, an unstable atmospheric layer rises, culminating in a central slantwise updraft that reaches the tropopause. This principal updraft then continues horizontally as an eastward flow, with the subsequent subsidence manifesting as a mesoscale downdraft on the right, while a subsidiary branch of the updraft diverges to the left at the top.

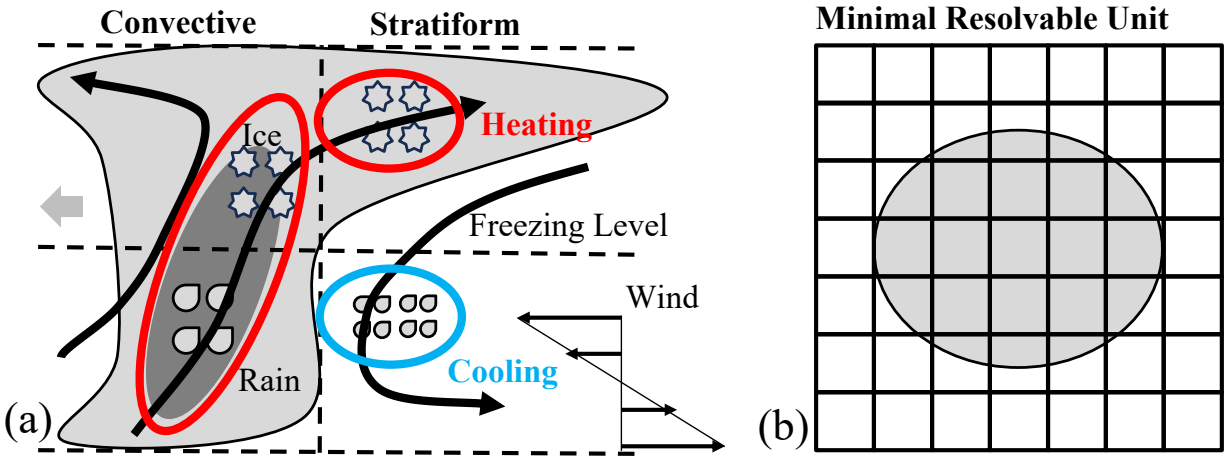

Figure 1. Schematic diagram for (a) stratiform and convective vertical cross sections in slantwise layer overturning scenario. Streamlines indicate wind directions. Red and blue circles represent the diabatic heating and cooling regions, respectively. The grey arrow represents the MCS propagation direction. Adapted from Moncrieff et al. (2017). (b) Top view of a 7 by 7 model-grid domain capable of minimally resolving the MCS (grey shading).

Figure 1a presents the dynamical correspondence with microphysical processes occurring within the convective and stratiform regions. The slantwise ascending layer in the center aligns with the convective region, where condensational heating is driven by updrafts loaded with raindrops below and ice condensates starting above the freezing level. The updrafts that curve horizontally to the right carry ice condensates aloft, aiding in the horizontal growth of the stratiform region. In the stratiform region, the ice condensates undergo depositional growth, which releases latent heat in the upper atmosphere. As these particles fall below the freezing level, they melt into raindrops. This melting process, followed by evaporation, induces cooling in the stratiform region's lower levels.

Figure 1b illustrates the MCS previously described in Figure 1a, highlighting its nature as an under-resolved phenomena for a given model resolution. Skamarock (2004) has shown that models are capable of resolving features with a minimum length scale approximately seven times the model's horizontal grid spacing. Thus, a climate model with a 100 km grid spacing could theoretically resolve MCS with a length scale of at least 700 km. However, a significant number of MCSs have at least one dimension shorter than this resolvable scale. For instance, Feng et al. (2021) demonstrated that more than 90% of MCSs over the continental United States have precipitation features shorter than 700 km, indicating a limitation in the model's ability to capture the full spectrum of MCS sizes. This complexity necessitates the use of the MCSP paradigm for multi-scale-coherent representation.

The potential temperature heating increment due to convective updrafts is parameterized by the CoMorph-A convection scheme, and denoted as $\Delta\theta_{CoMorph}$. Figure 2a shows an example temperature tendency profile from the CoMorph-A scheme: this is typically a net heating effect at nearly all height levels, aligning with the conceptual model in Figure 1a.

In an advancement over previous MCSP triggers, we have formulated triggering conditions that are designed to recognize slantwise layer overturning and mixed-phase deep clouds:

$$\left|\overrightarrow{V_{600}} - \vec{V_s}\right| > 3\ m\ s^{-1} \quad (1)$$

$$T_{top} < 0\ °C \quad (2)$$

$$p_{base} > 600\ hPa \quad (3)$$

$$p_{base} - p_{top} > 300\ hPa \quad (4)$$

Firstly, equation 1 identifies conditions suitable for slantwise layer overturning through the absolute value of the difference in horizontal wind speed between the surface and the 600hPa level. Note that Chen et al. (2021) computed only zonal wind shear when applying their triggering threshold, while this study computes wind shear based on both zonal and meridional wind components to depict the pattern of slantwise layer overturning. Secondly, the definition of mixed-phase deep cloud involves meeting three criteria, detailed in equations 2–4: 1) The cloud top temperature (T_{top}) must be below 0 °C, a threshold crucial for the production of ice condensates, which are key to generating stratiform precipitation. 2) The cloud base pressure (p_{base}) should be above 600 hPa, ensuring that there is adequate low-level moisture to support

and maintain deep convection. 3) The pressure difference between the cloud base and top ($p_{base} - p_{top}$) must exceed 300 hPa, confirming that the cloud has sufficient depth.

Building on Moncrieff (2017), the convective heating from CoMorph-A and the PRIME-MCSP stratiform heating are related through equations 5–7:

$$\overline{\overline{Q_{conv}}} = \frac{1}{p_s - p_{top}} \sum_{p_s}^{p_{top}} \Delta\theta_{CoMorph}(p) dp \quad (5)$$

$$Q_{strat}(p) = \alpha \sin\left(2\pi \frac{p_{top} - p}{p_s - p_{top}}\right) \overline{\overline{Q_{conv}}} \quad (6)$$

$$\alpha = 0.5 \text{ or } 0.5\left(\frac{T_{freeze} - T_{top}}{T_{freeze} - T_{ref}}\right) \quad (7)$$

where p_s and p_{top} represent the surface and cloud top pressure levels, respectively, while dp denotes the pressure difference between adjacent model levels. Equation 5 calculates the column-integrated convection scheme heating from the surface to the cloud top, normalized by the total pressure difference. Equation 6 posits that the amplitude of the stratiform aloft heating is proportional to the column-integrated convective heating and to a parameter α. The sinusoidal shape means that the column integral of stratiform heating aloft and low-level cooling balances out to approximately zero. Figure 2b illustrates the vertical distribution of the emulated stratiform latent heating that corresponds to the example CoMorph-A profile of Figure 2a.

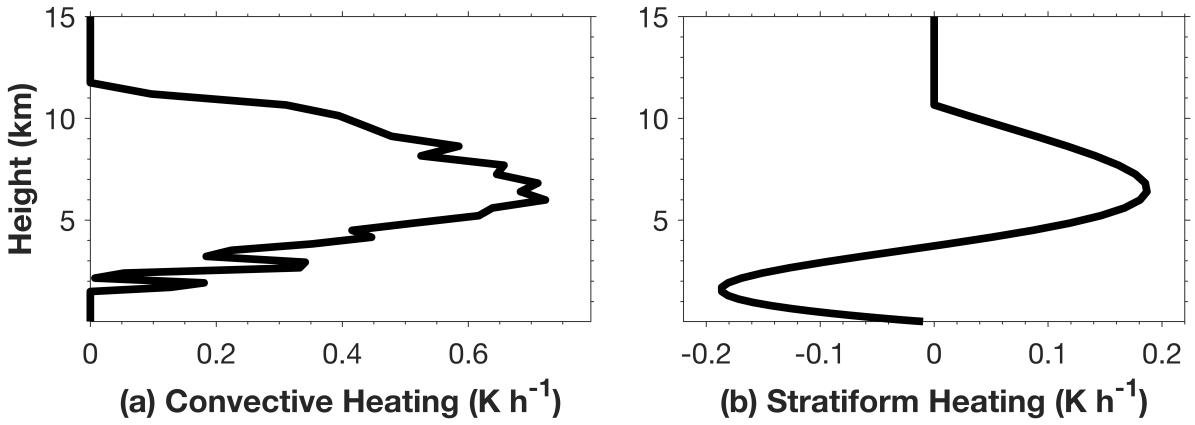

Figure 2. (a) Example tendency profile obtained from the CoMorph-A convection scheme, and (b) the corresponding stratiform tendency determined by PRIME-MCSP.

Previous studies (e.g., Chen et al. 2021) have used equation 6 with α set to a fixed value of 0.5. Here, we also consider a variable α dependent on the temperature difference between the freezing level T_{freeze} and the cloud top T_{top}, normalized by the temperature difference between T_{freeze} and a reference cloud top level T_{ref}, as shown in equation 7. The variable α is designed to reflect the idea that the growth of the stratiform region is proportional to the ice condensate flux from the convective to the stratiform region and that ice condensate production correlates with the temperature difference between the cloud top and the freezing level, indicated by Han et

al. (2019) and Zhang et al. (2024). T_{freeze} is set at 0°C, and T_{ref} to –80°C, representing the median value of the lifecycle-minimum cloud top temperature observed in global storm tracks (Feng et al., 2021).

The stratiform latent heating profile in equation 6 is intended to have a vertical integral of zero. However, due to the discrete nature of vertical levels in the model, a small residual may exist in practice. The residual in dry static energy is computed, and used to calculate the pressure-weighted residual error, denoted as $\overline{Q_{err}}$:

$$\overline{Q_{err}} = \frac{1}{p_s - p_{top}} \sum_{p_s}^{p_{top}} Q_{strat}(p) dp \quad (8)$$

The final potential temperature tendency $\Delta\theta_{org}(p)$ for a given grid at a specific level, resulting from the organized convection, is computed as the sum of $\Delta\theta_{CoMorph}(p)$ and $Q_{strat}(p)$, adjusted by subtracting $\overline{Q_{err}}$:

$$\Delta\theta_{org}(p) = \Delta\theta_{CoMorph}(p) + Q_{strat}(p) - \overline{Q_{err}} \quad (9)$$

The PRIME-MCSP tendency as represented in equation 9 ensures the conservation of dry static energy within a column, even after incorporating stratiform latent heating into the model.

3 Simulations, Observations, and Storm Tracking Methodology

The PRIME-MCSP scheme has been implemented into version 13.0 of the Unified Model (UM13.0), developed by the United Kingdom Met Office. Its critical modules are described in Davies et al. (2005). Both the weather ensemble and climate simulations utilize UM13.0 over a global domain. The PRIME-MCSP scheme is evaluated by comparing against control runs where PRIME-MCSP is deactivated.

Table 1. Weather Simulations Spanning from July 1st, 2020, 03Z to July 3rd, 2020, 03Z.

Name of Experiment	PRIME-MCSP Scheme	α	Resolution	Ensemble Members
Control Run	N/A	N/A	~60 km	8
PRIME-MCSP Run	Activated	0.5	~60 km	8

The weather ensemble, as detailed in Table 1, is employed to evaluate the direct, short-term effects of PRIME-MCSP on storm lifecycles and their surrounding environments from a Lagrangian perspective. It has a horizontal grid spacing of approximately 60 km (N216) and 70 vertical levels. The model's integration time step is 7.5 minutes. The simulations are restarted from 8 initial-condition perturbed ensemble members of the Met Office Global and Regional Ensemble Prediction System–Global (Inverarity et al. 2023), on July 1st, 2020, at 0Z, and undergo a 3-hour spin-up. The analyzed simulations span a duration of 48 hours, starting from July 1st, 2020, at 3Z and ending on July 3rd, 2020, at 3Z. Two sets of simulations are produced: a set of control runs and a set of PRIME-MCSP runs, with the latter implementing a fixed α value of 0.5. Except for the CoMorph-A convection scheme, all other physical parameterizations in these weather ensemble members align with those used in the Met Office's operational weather forecasts, as described in Bush et al. (2022).

283 **Table 2.** Climate Simulations Spanning September 1988 to August 2008.

Name of Experiment	**PRIME-MCSP Scheme**	**α**	**Resolution**
Control Run	N/A	N/A	~135 km
PRIME-MCSP Run	Activated	0.5	~135 km
PRIME-MCSP Variable α Run	Activated	Variable α	~135 km

284 The climate simulations, as detailed in Table 2, aim to assess the long-term effects of
285 PRIME-MCSP on the large-scale precipitation patterns and MJO. This evaluation is based on
286 three model runs, each spanning 20 years from September 1988 to August 2008. The simulations
287 employ a horizontal grid spacing of approximately 135 km (N96) and have 85 vertical levels.
288 The model's integration time step is 20 minutes. The set includes a control run where the
289 PRIME-MCSP scheme is deactivated, a standard PRIME-MCSP run with a fixed α value of 0.5,
290 and a PRIME-MCSP Variable α run. In the Variable α run, the stratiform-to-convective heating
291 fraction is dynamically adjusted based on the cloud top temperature, as described above. Except
292 for the adoption of the CoMorph-A convection scheme, the model setup adheres to the Met
293 Office Atmospheric Model Intercomparison Project Phase 6 (AMIP6) configuration, with the
294 atmospheric model being forced by climatological boundary conditions (Walters et al. 2019).

295 The reference dataset utilized for the global assessment comprises several key sources:
296 the Global Precipitation Climatology Project (GPCP; Pendergrass et al. (2022), is employed to
297 assess the accuracy of simulated monthly precipitation. Furthermore, we use 26 models from the
298 Coupled Model Intercomparison Project Phase 6 (CMIP6; Eyring et al. 2016a) to analyze the
299 seasonal cycle of precipitation. These 26 models were selected following the research of Lauer et
300 al. (2023) to include only the atmospheric components of the CMIP6 models and prescribed
301 observed SSTs. This selection, known as AMIP6, represents the state-of-the-art capability for
302 predicting the atmospheric climate state. The National Centers for Environmental Prediction
303 (NCEP) Reanalysis data (Kalnay et al. 1996) serves to evaluate the MJO. The observed global
304 MCS tracks, as identified by Feng et al. (2021), are applied to assess the frequency of PRIME-
305 MCSP scheme being called.

306 Customized MCS tracking in this project utilizes the PyFLEXTRKR software, as detailed
307 by Feng et al. (2023), employing hourly maps of Top-Of-Atmosphere (TOA) infrared brightness
308 temperatures (IR T_b) alongside the surface rain rates. The conversion of simulated TOA
309 Outgoing Longwave Radiation (OLR) to IR T_b is achieved through the empirical correlation
310 established by Yang and Slingo (2001), enabling MCS identification as depicted in Figure 3a.
311 The MCS cold cloud shield mask is defined as its IR T_b falling below 241 K. This mask is
312 subsequently used to estimate the rainfall area and the mean rain rate underneath the MCS. The
313 criteria for selecting representative MCSs are a minimum cold cloud shield size of 60,000 km^2 at
314 the peak of its lifecycle, coupled with a duration exceeding 6 hours. Tracking an MCS requires a
315 minimum 50% overlap in its cold cloud shields for two consecutive model output time steps of
316 half an hour. Additional tracking configurations are elaborated in Feng et al. (2023).

317 MCS track matching between the MCS masks in the control (Figure 3a, black contours)
318 and the PRIME-MCSP (Figure 3b, black contours) runs is performed by requiring an areal
319 overlap ratio above 80% at the MCS initiation time. The magenta dots and lines in Figure 3a
320 illustrate the centroids and the path of the MCS at later times within the control run. The MCS

cloud region is delineated by the cold cloud shield mask, and the surrounding area of interest is defined as a region within a 600 km radius around the centroid (marked by the black circle in Figure 3a), excluding the areas under the cold cloud shield mask. The MCS cloud region and its surrounding area in the control run serve as the spatial basis ranges for computing the difference between fields in the control run and the PRIME-MCSP run. These differences are used to evaluate the effect of the PRIME-MCSP scheme throughout the MCS lifecycle.

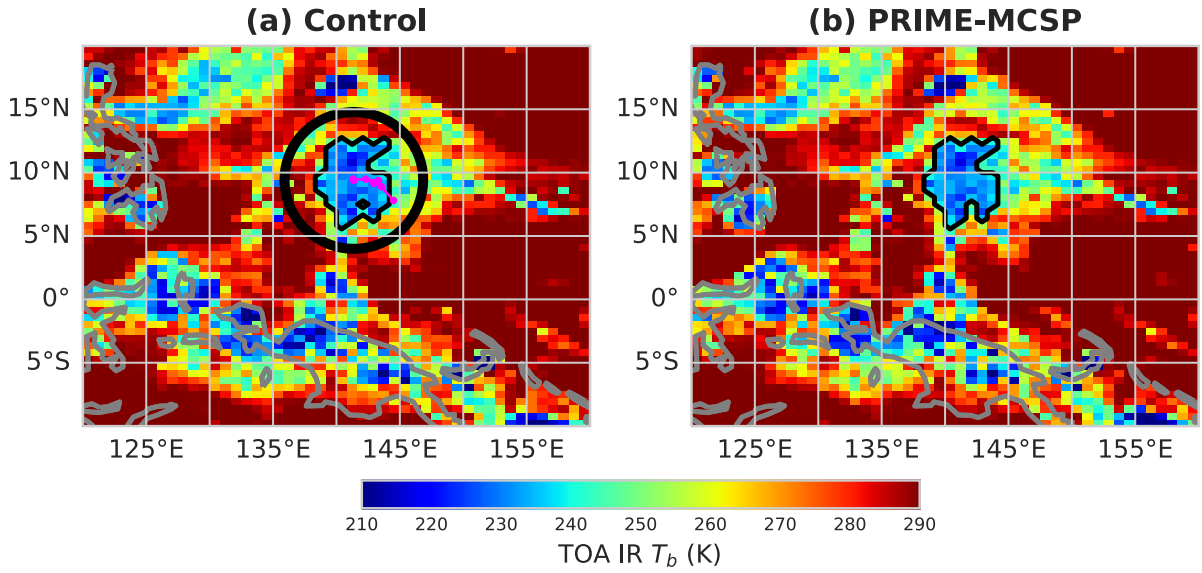

Figure 3. MCS track on July 1st, 2020, at 04:00 UTC. (a) The control run. The magenta dots and lines trace the MCS centroids and trajectory, respectively; the circle delineates the MCS surrounding environmental area of interest. (b) The PRIME-MCSP model run. The MCS boundaries in (a) and (b) are delineated by black contours. The grey contours delineate the coastlines over the Maritime Continent.

4 Direct Effects of the Scheme in Weather Ensembles

Figure 4a shows the count of global MCS tracks in both control and PRIME-MCSP ensemble runs across ensemble members 1 to 8, represented by blue and green bars, respectively. The PRIME-MCSP runs show a general concurrence with the control, albeit with a slight reduction in MCS track numbers. Approximately one-third to one-half of MCS tracks (indicated by red bars in Figure 4a) are matchable between control and PRIME-MCSP runs, totaling 163 MCS tracks across 8 ensemble members. The detailed MCS track matching method has been described in Section 3.

Figure 4b shows the frequency of PRIME-MCSP scheme activations throughout the normalized MCS lifecycle. The lifecycle of the MCS is normalized into 10 timesteps, ranging from 0 (initiation) to 9 (termination). The characteristics of the MCS are linearly interpolated across these 10 normalized timesteps to facilitate the combination of lifecycle evolutions. The calling frequency is defined as the ratio between grid points activating the PRIME-MCSP scheme and the grid points within the MCS mask area. Data from all MCS tracks in ensemble members is aggregated in Figure 4b. The median MCSP frequency exhibits a relatively stable evolution throughout the lifecycle with variations from 18% to 24% of the MCS area. This is in

agreement with the prior MCSP approach (e.g., Moncrieff & Liu, 2006), wherein the scheme is called in the convecting regions of the MCS, not the anvil. In addition to the combined statistics, Figure 4c shows a histogram of autocorrelation at a one-time-step lag, based on the calling frequency within each individual MCS lifecycle. The correlation coefficient is concentrated around 0.7, indicating the consistency of the calling frequency throughout each MCS lifecycle. This lifecycle continuity of calling frequency suggests effective coupling of the PRIME-MCSP scheme with the CoMorph-A convection scheme, avoiding abrupt activations or deactivations.

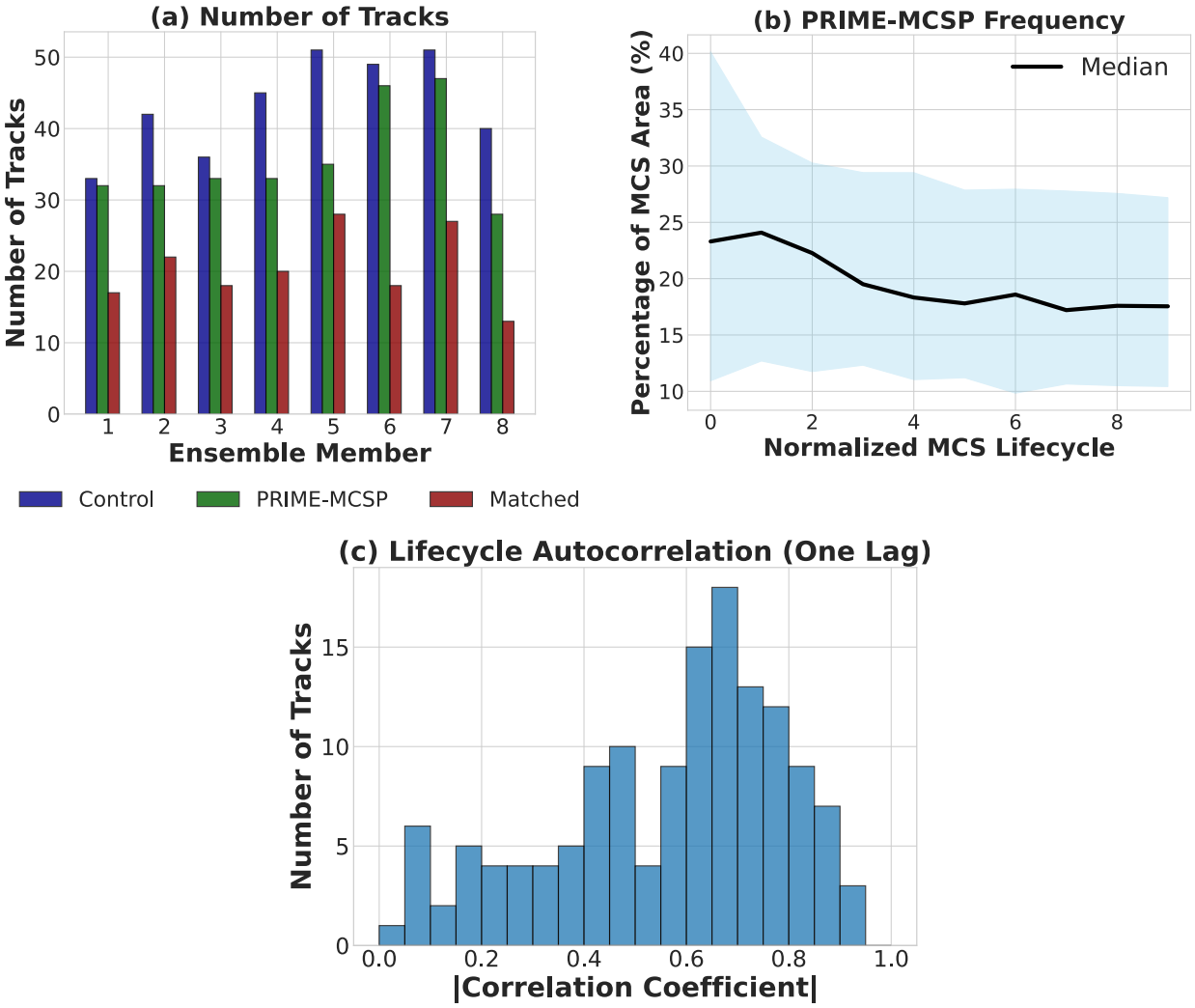

Figure 4. (a) MCS track counts, (b) invocation frequencies of the scheme across the MCS lifecycles. The shaded areas represent the Interquartile Range (IQR) in all matched tracks from all ensemble members, spanning the 25th to 75th percentiles, while the median value is depicted by the solid black line, and (c) histogram of the absolute values of MCS lifecycle autocorrelation with a one-time-step lag.

The PRIME-MCSP scheme primarily functions to transfer heat from the lower to the upper troposphere. We examine the evolution of spatially averaged temperature throughout the normalized lifecycles of the MCSs in both the cloud areas and surrounding environments. The normalized lifecycles, cloud areas, and MCS surrounding environments are based on the MCS

tracks in the control run that have corresponding matches in the PRIME-MCSP runs. It appears that the temperature does not change much throughout the lifecycle. Therefore, our analysis focuses on the temperature differences between the PRIME-MCSP run and the control run. In Figure 5 a–b, we observe a decrease in temperature for both the MCS cloud and the surrounding environment at 850 hPa as time progresses, with the rate of change in the MCS cloud being more pronounced. This indicates that the PRIME-MCSP scheme effectively induces cooling in the lower troposphere, as intended, and that over time, this cooling effect extends to the MCS's surrounding environment. Conversely, Figure 5 c–d shows an increase in temperature at 200 hPa for both the MCS cloud and the environment, again with a faster rate of change within the cloud. This demonstrates the scheme's role in upper tropospheric warming, with the additional heating in the cloud area gradually affecting the surrounding MCS environment over time.

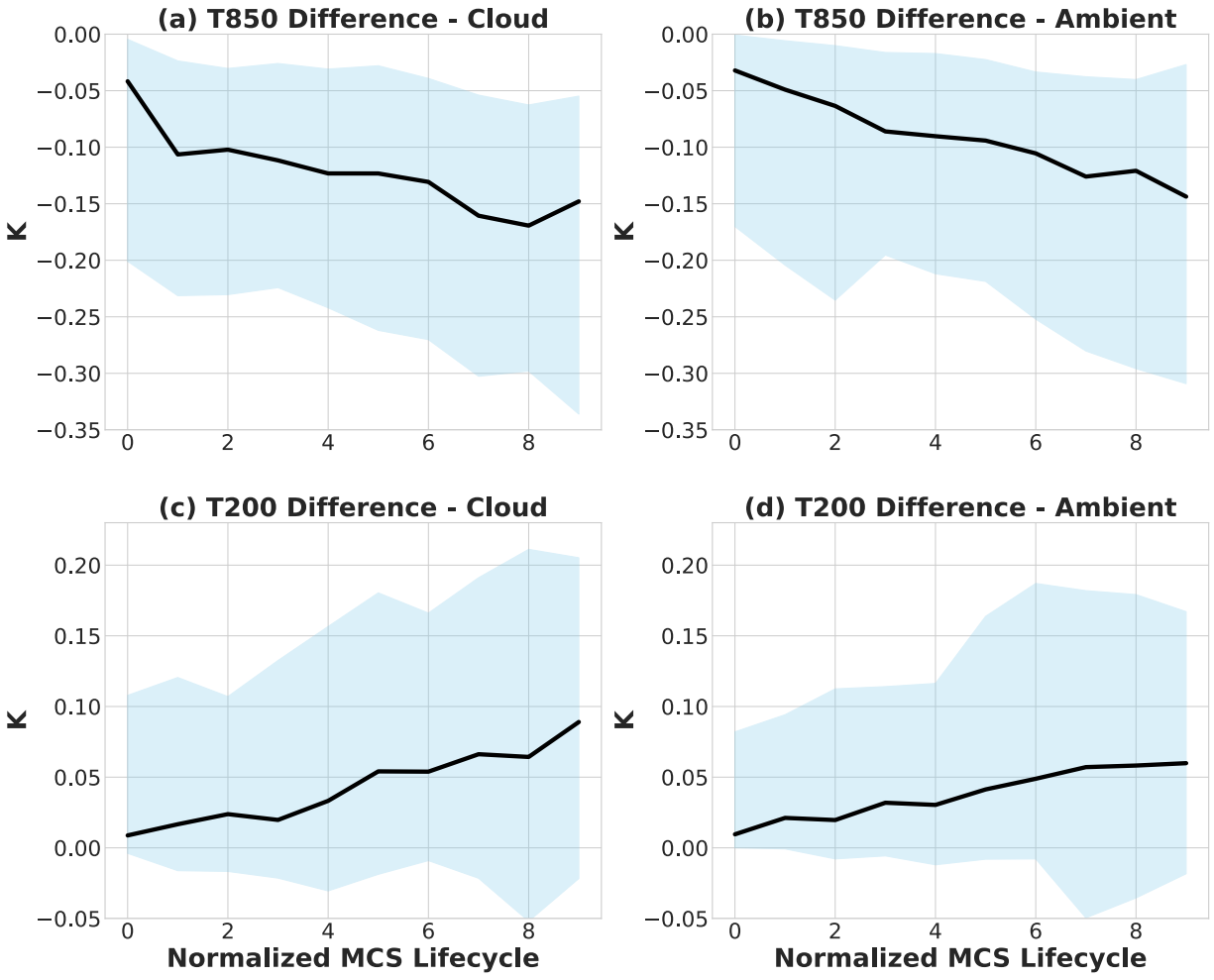

Figure 5. Temperature differences between the PRIME-MCSP and the control runs within MCS clouds and their surrounding environments at both 850 hPa (a–b) and 200 hPa (c–d) throughout the normalized MCS lifecycle, using the MCS tracks in the control run that have matches in the PRIME-MCSP runs. Shaded areas and lines follow the conventions from Figure 4b. Simulations span July 1st, 2020, 03Z to July 3rd, 2020, 03Z.

Figure 6 shows the response of 850 hPa vertical velocity to the lower tropospheric cooling induced by the PRIME-MCSP scheme. Within the MCS, a predominant positive vertical velocity is associated with ongoing convective updrafts throughout the lifecycle (Figure 6a). Conversely, in the surrounding environments of the MCS, a negative vertical velocity is also persistent, indicating the presence of environmental subsidence air (Figure 6c). When the PRIME-MCSP scheme is active, there is a weakening of convective updrafts (Figure 6b) and a corresponding weakening of the surrounding air subsidence (Figure 6d). These alterations highlight the PRIME-MCSP scheme's effect in moderating the explicit mesoscale circulations associated with the MCS. Additionally, an examination of the 200 hPa vertical velocity response (supplemental Figure S1) reveals no significant change, suggesting that the effects of the PRIME-MCSP upper tropospheric heating are nuanced, likely influenced by cloud top height and interactions with gravity waves.

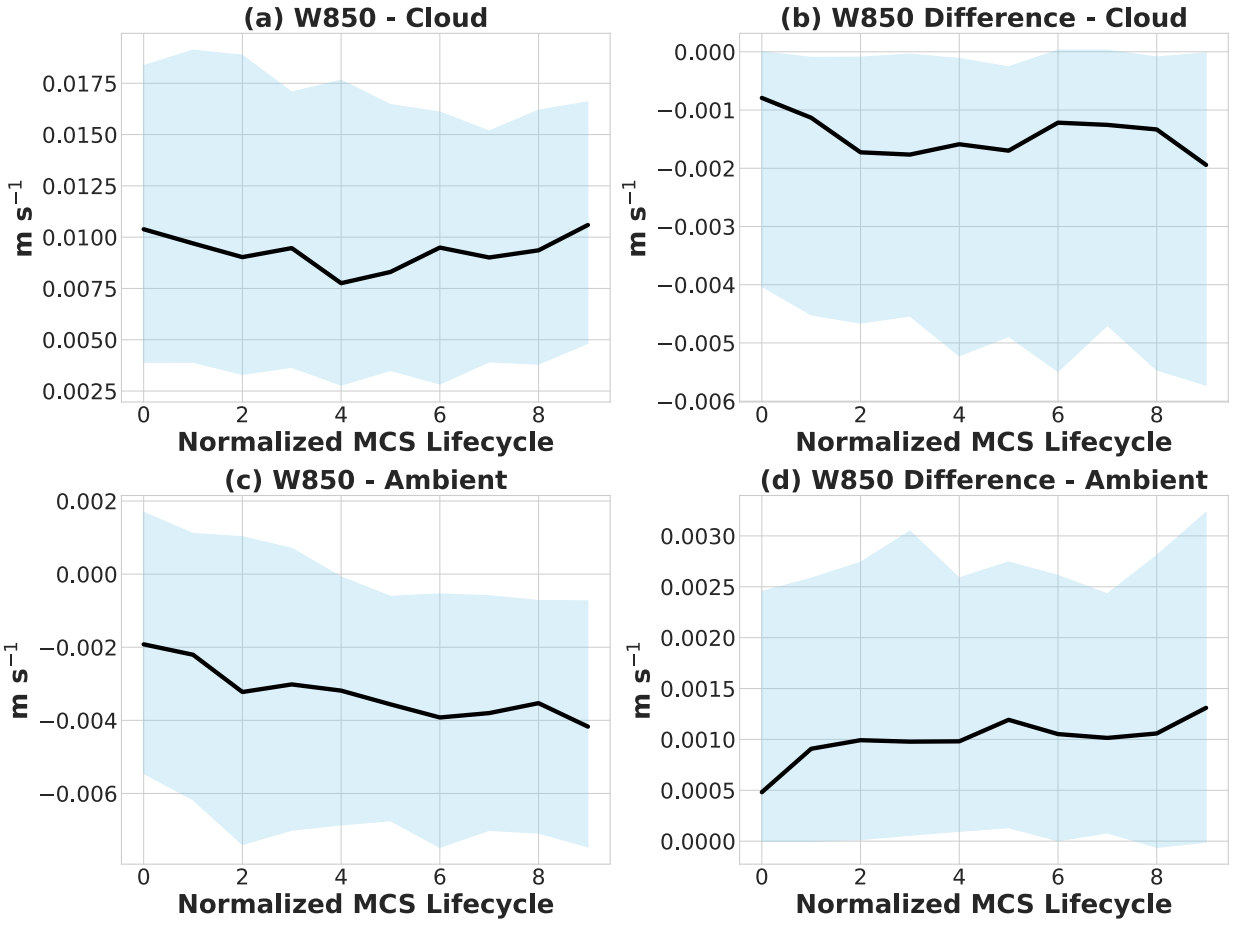

Figure 6. (a, c) 850 hPa vertical velocity in the control runs and (b, d) their changes following PRIME-MCSP activation, where a positive velocity indicates upward motion. Shaded areas and line conventions are as described in Figure 4b. Simulations span July 1st, 2020, 03Z to July 3rd, 2020, 03Z.

The impact of the PRIME-MCSP scheme on regional circulation is further demonstrated in Figure 7, which presents a global map highlighting the differences in 850 hPa vertical velocity between the MCSP run ensemble mean and the control run ensemble mean. Notably, over the

part of Intertropical Convergence Zone (ITCZ) between 10°–180°W, 0°–20°N and over various extratropical low-level jet regions, the formation of three parallel bands—central blue shading flanked by two red shading bands—mirrors the findings from Figure 6, indicating suppressed regional upward motion and reduced surrounding subsidence following the PRIME-MCSP scheme activation.

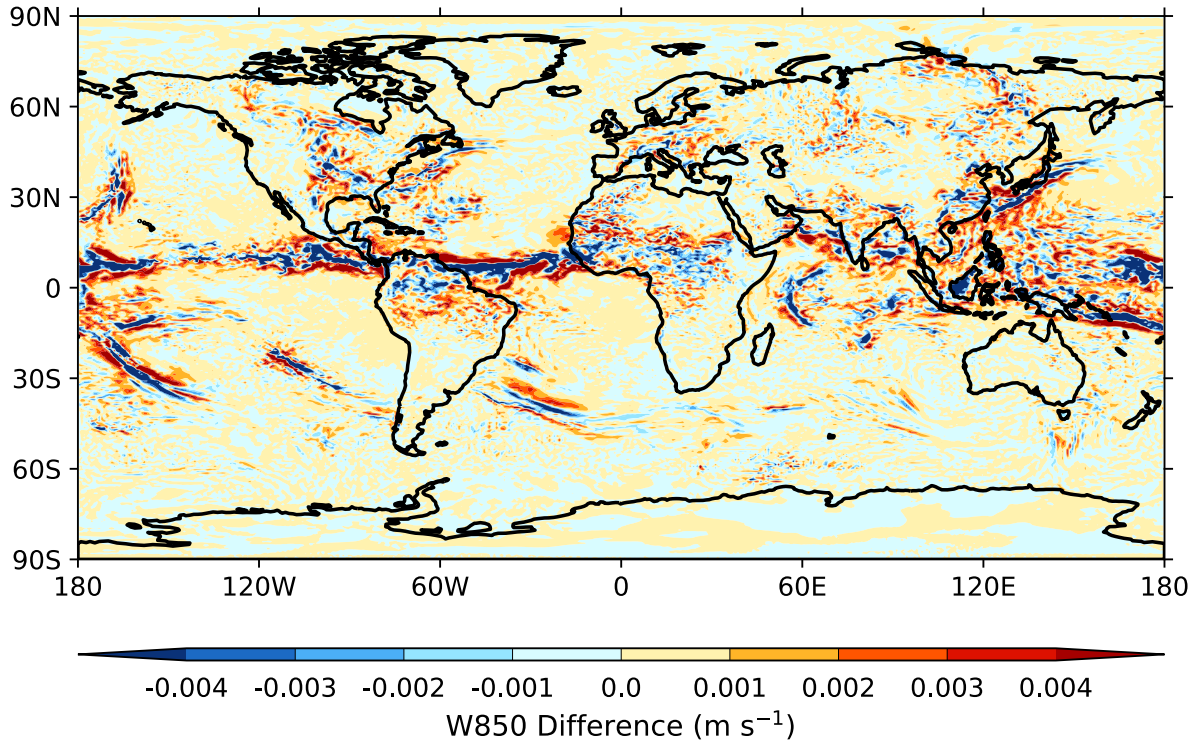

Figure 7. Ensemble mean difference in 850 hPa vertical velocity between the PRIME-MCSP and control runs, with black contours delineating coastlines. The averaging period is based on the entire 48 hours of the analyzed simulations.

The weakened circulations are linked to changes in MCS characteristics, including convective depth, rainfall area, and rain rate. Convective depth is represented by the minimum TOA IR T_b within the MCS's cold cloud shield, where colder TOA IR T_b values signify deeper MCS convective systems (Figure 8a). The PRIME-MCSP scheme results in a consistently positive TOA IR Tb difference throughout the MCS lifecycle (Figure 8b), suggesting a reduction in convective depth. The area covered by rainfall expands as the MCS matures, stabilizing in the latter part of the lifecycle (Figure 8c). The difference in rainfall area is consistently negative (Figure 8d), indicating the PRIME-MCSP scheme's tendency to reduce the rainfall area beneath the MCS's cold cloud shield. This explains the decrease in MCS track numbers as shown in Figure 4a, since a reduced MCS area impacts the number of cases meeting the lifecycle-maximum area threshold. Consistent with previous research indicating a positive correlation between convective depth and MCS area (Zhang et al., 2021), the decrease in convective depth is associated here with reduction in area. The PRIME-MCSP scheme's impact on rain rate is minimal, likely because rain rate is more influenced by large-scale microphysics, and the scheme primarily modifies heating tendencies without directly affecting rain rate. Combining reduced

rainfall area with an unchanged rain rate suggests a decrease in rainfall volume within MCSs following PRIME-MCSP activation. Accumulating these differences over time, along with changes in large-scale circulations, the long-term indirect effect of PRIME-MCSP on rainfall is assessed in Section 5.

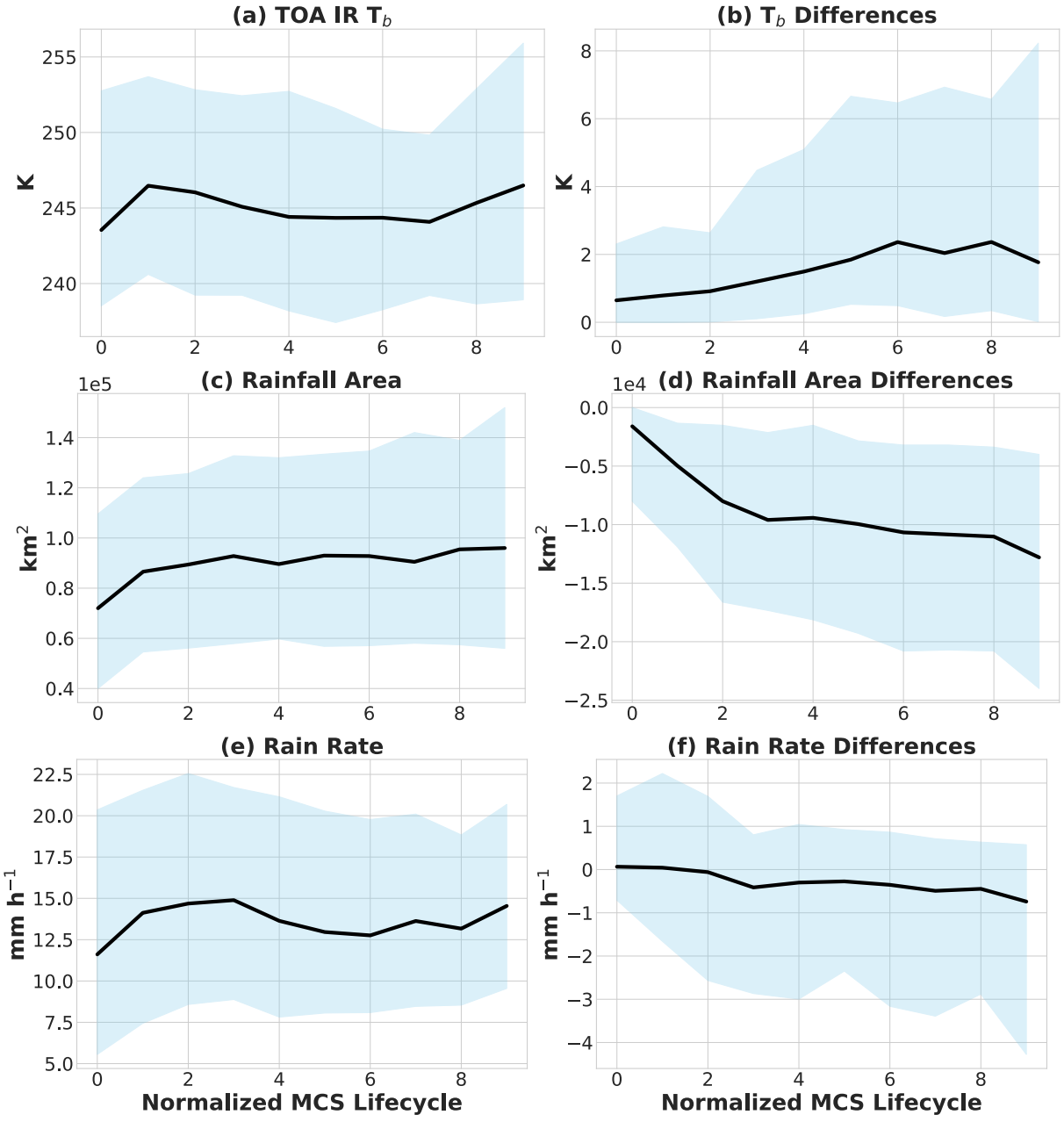

Figure 8. The lifecycles of (a) TOA IR T_b, (c) rainfall area, and (e) rain rate in the control run, and their changes (b, d, and f) following PRIME-MCSP activation. Simulations span July 1st, 2020, 03Z to July 3rd, 2020, 03Z.

5 Indirect Effects of the Scheme in Decadal Simulations

Before considering the indirect effects of the PRIME-MCSP scheme, we first compare the calling frequency of the scheme with real-world MCS occurrence frequencies. The comparison period spans from June 2000 to August 2008, coinciding with PRIME-MCSP runs and observed MCS track data from Feng et al. (2021). Figure 9a shows the MCS occurrence frequency using the observed global MCS track dataset, with color shading indicating the percentage of time the MCS cold cloud shield is present. Figure 9b illustrates the frequency of PRIME-MCSP scheme activation, defined by the percentage of timesteps on which the scheme is called. MCS frequencies generally exceed PRIME-MCSP activation frequencies (compare the color scales in Figures 9a and 9b). The relative spatial patterns show general agreement but with some regional discrepancies. PRIME-MCSP activation frequencies are relatively low over the Maritime Continent and slightly below those found in the ITCZ. Magenta rectangles in Figure 9 highlight areas where PRIME-MCSP frequencies strongly disagree with the MCS pattern, particularly over India and the Indian Ocean, with an expanded strong center further north over the Western Pacific.

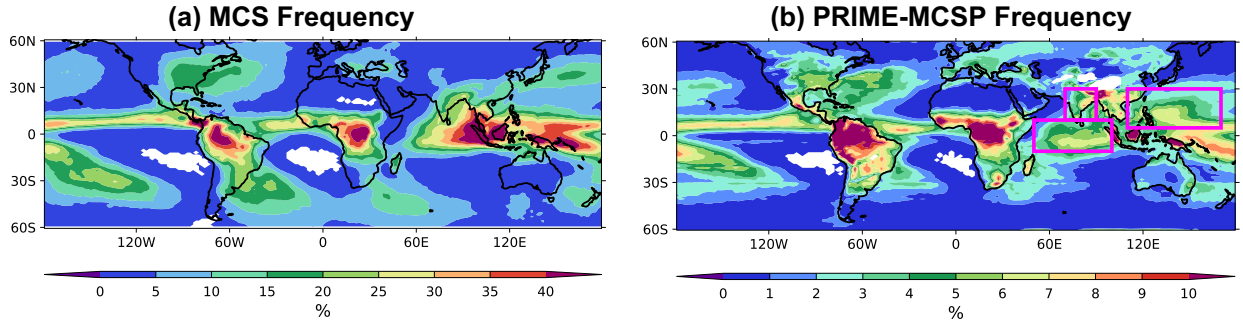

Figure 9. (a) Observed MCS occurrence frequency and (b) frequency of calling the PRIME-MCSP scheme in the decadal run. Magenta rectangles highlight regions of interest: India, the Indian Ocean, and the Western Pacific. The comparison period spans June 2000 to August 2008.

Figure 10 presents a comparison of the averaged global rain rate distributions as derived from satellite retrievals (GPCP), alongside those from the control, PRIME-MCSP, and PRIME-MCSP variable α runs over a 20-year period from September 1988 to August 2008. The Pearson correlation coefficients between the GPCP and these three simulations are 0.91, 0.91, and 0.92, respectively. These correlations indicate that the PRIME-MCSP scheme maintains the accuracy of global rainfall distribution.

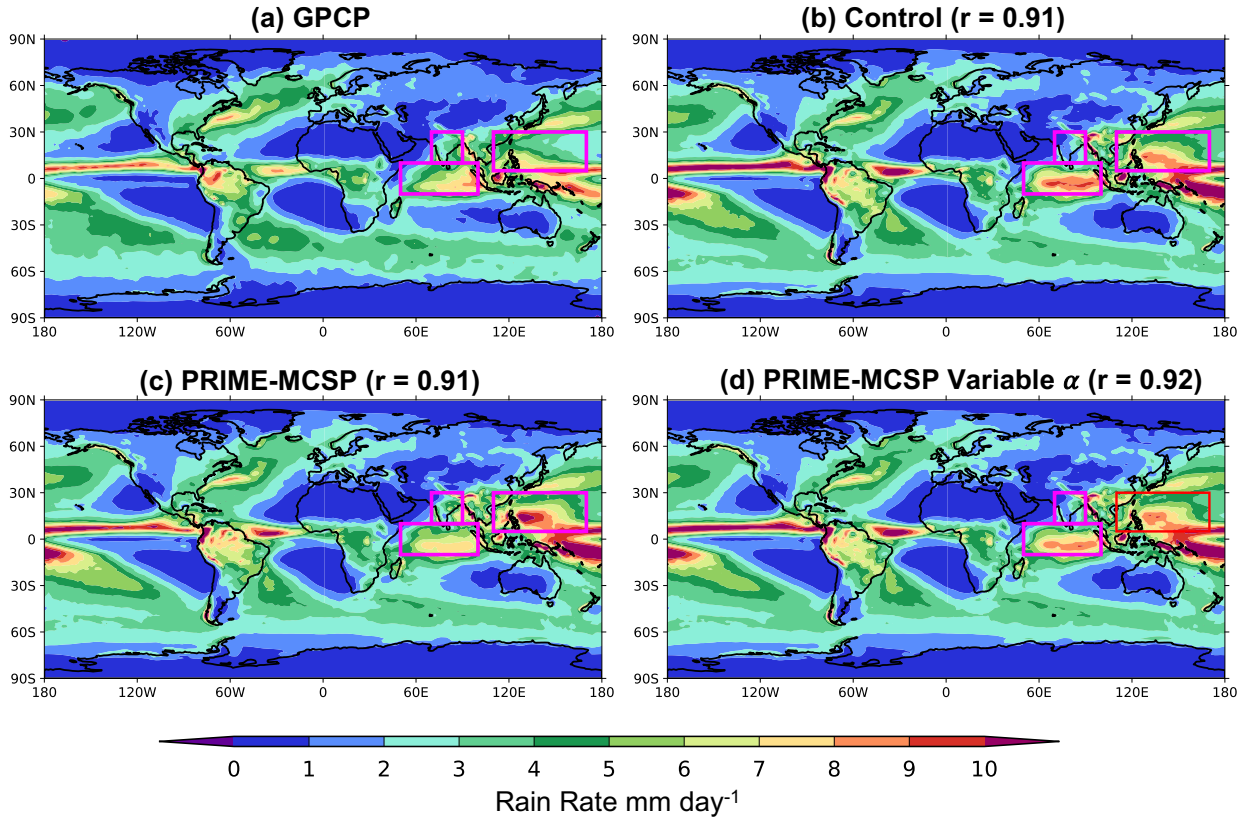

Figure 10. Average rain rate maps from (a) GPCP retrieval, (b) control, (c) PRIME-MCSP, and (d) PRIME-MCSP variable α runs. The Pearson correlation coefficient between the model runs and the GPCP retrieval is quoted for panels (b–d) as "r". All simulations and observations span September 1988 to August 2008.

Figure 11a presents the difference in rainfall between the control run and GPCP retrievals, with warm and cold colors indicating precipitation overestimation and underestimation, respectively. Predominantly, the control run overestimates rainfall across most tropical regions, especially within the ITCZ. Specifically, it overestimates rainfall over the Indian Ocean and Western Pacific, while underestimating it over India and the Bay of Bengal. These control run biases are consistent with Bush et al. (2014). Figure 11b demonstrates how PRIME-MCSP affects these biases, reducing the dry bias over India and mitigating the wet bias over the Indian Ocean, albeit amplifying it over the Western Pacific. The PRIME-MCSP variable α run generally mediates between the PRIME-MCSP and control runs, with a notable reduction in the wet bias over the Western Pacific compared to the PRIME-MCSP run, as indicated in supplemental Figure S2. However, improvements in rainfall accuracy over India and the Indian Ocean are more pronounced in the PRIME-MCSP run than in the PRIME-MCSP variable α run.

Figures 11c and 11d compare the absolute differences in rainfall biases (between the GPCP and model runs) before and after activating the PRIME-MCSP scheme, using a significance test based on 10,000 bootstrap resamples. Areas with significant changes (p values < 5%) in rainfall bias are marked with stipples, with cold and warm shadings indicating bias mitigation and amplification, respectively. The results suggest that improvements over India and the Indian Ocean are statistically significant. In contrast, the Western Pacific shows high internal

variability such that the apparent bias amplification in that region could be due to chance. The PRIME-MCSP variable α run shows a similar pattern to the PRIME-MCSP run but with a lesser magnitude of bias change and fewer significance stipples, indicating a balance between bias mitigation over the Indian Ocean and bias worsening over the Western Pacific, with a less significant improvement over the Indian Ocean compared to the PRIME-MCSP run.

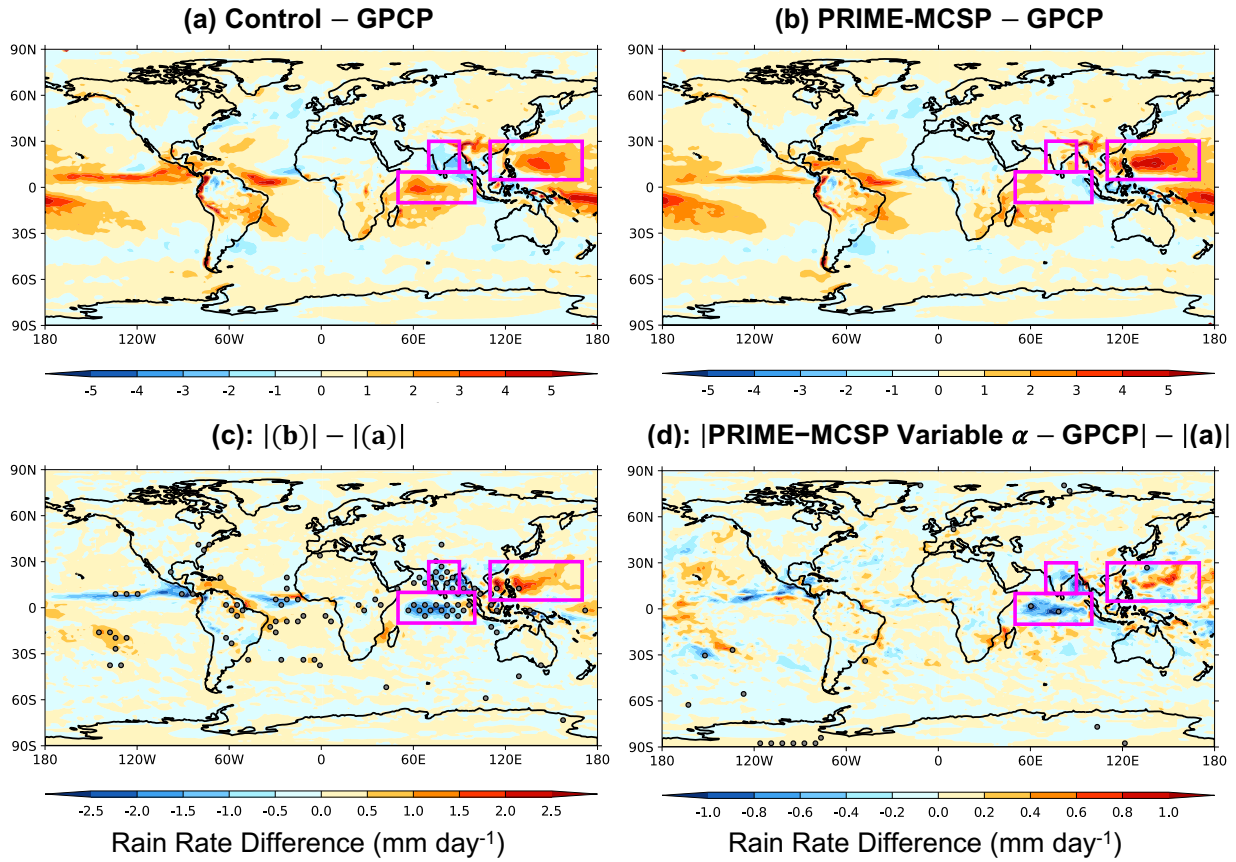

Figure 11. Rainfall difference between (a) the control run and GPCP, (b) the PRIME-MCSP run and GPCP, (c) the difference between the absolute values of (b) and (a), and (d) the same calculation as in (c) but for the PRIME-MCSP variable α run. The stippling in (c) and (d) indicates statistical significance, determined as described in the main text. Note the change of color scale between (c) and (d). All simulations and observations span September 1988 to August 2008.

In Figure 12, the annual cycles of precipitation seasonal cycles are used to diagnose further the rainfall changes over India and the Indian ocean in the PRIME-MCSP run and to compare with the control run and the CMIP6 ensemble simulations.

Over India, the control run significantly underestimates the rainfall, especially during the summer monsoon (Figure 12a). CMIP6 models agree better with the GPCP retrieval while overestimating the median precipitation from May to October (Figure 12b). The PRIME-MCSP run shows the closest agreement with the GPCP retrieval, outperforming both the control run and CMIP6 simulations, especially in correcting the underestimation of rainfall, as shown in Figure

12c. However, the IQRs in all these simulations are greater than those observed, highlighting the persistent model uncertainties across all models.

Over the Indian Ocean, the control run fails to capture the phase of the seasonal cycle and overestimates rainfall during all months (Figure 12d). CMIP6 performs better to agree with the observations in both timing and rainfall amounts from January to June, but significantly overestimates the precipitation from July to December (Figure 12e). The PRIME-MCSP run simulates both the phase and amplitude of the seasonal precipitation cycle, aligning closely with GPCP retrievals and markedly deviating from CMIP6 predictions (Figure 12f).

The PRIME-MCSP run suppassing CMIP6 predictions to agree with GPCP over the Indian ocean is particularly noteworthy given the run's coarser grid spacing relative to most CMIP6 simulations, suggesting the PRIME-MCSP scheme's upscaling effect plays a crucial role in capturing large-scale circulation patterns in this region. Consistently, the PRIME-MCSP variable α run also improves these seasonal cycles as for the PRIME-MCSP run, but with a muted amplitude alteration (shown in the supplemental Figure S3).

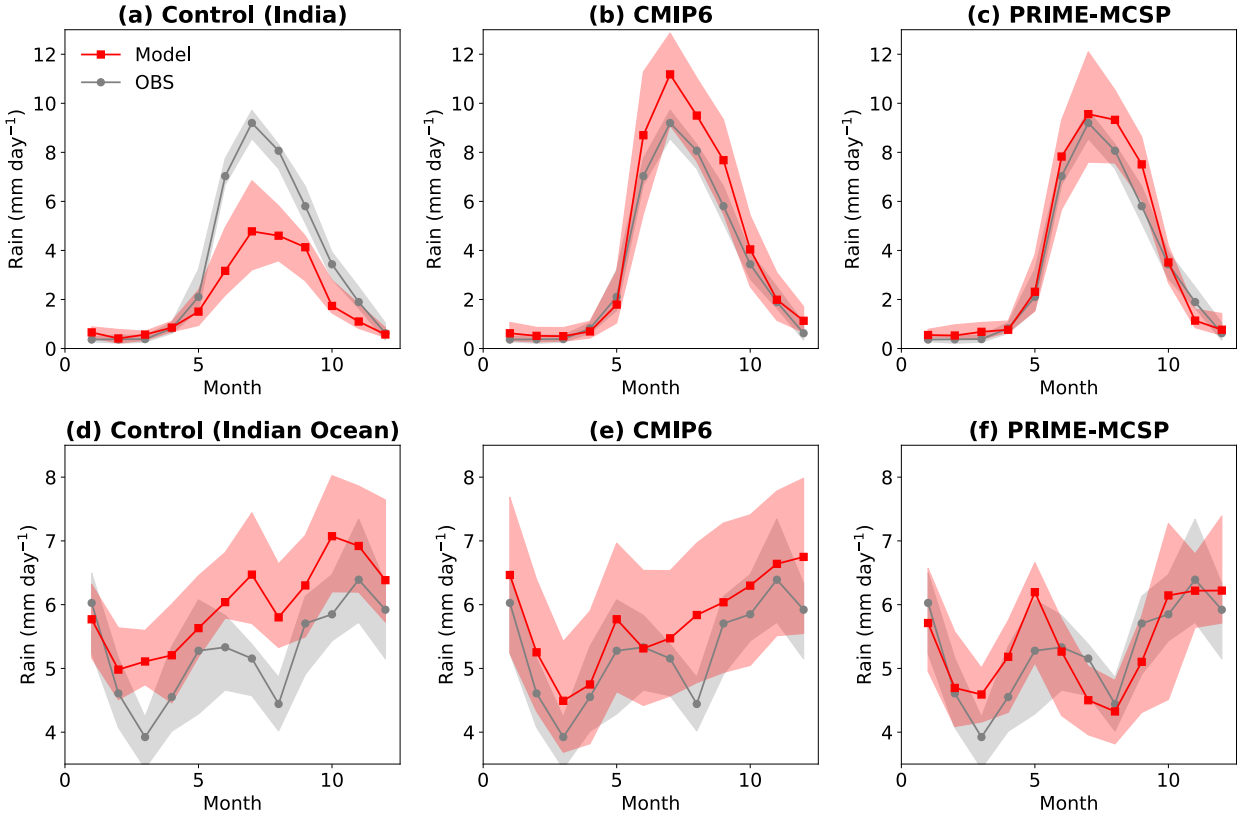

Figure 12. Simulated (red) and GPCP retrieved (grey) annual cycles of precipitation in the (a, d) control, (b, e) CMIP6, and (c, f) PRIME-MCSP run. The bands and lines indicate the IQR ranges and median values respectively. The India (a,b,c) and Indian ocean (d,e,f) regions are shown by the magenta boxes in Figure 10. All simulations and observations span September 1988 to August 2008.

The MJO plays a crucial role in influencing the annual precipitation cycle over India and the Indian Ocean, as proved in past studies (e.g., Hoell et al. 2018; Rushley et al. 2023). The

MJO's characteristics are analyzed for these climate runs in comparison with reanalysis, using the community software ESMValTool (Eyring et al. 2016b).

Figure 13 shows the symmetric wave cross spectra, derived from OLR and zonal wind data across the latitude range of 20°N to 20°S, following the methodology of Wheeler and Kiladis (1999). The spectral power density, depicted through color shading, highlights the presence of MJO signals. Specifically, Figure 13a identifies a peak at the MJO's characteristic period (20 to 100 days) and spatial scale (wavenumbers 1–2) with an orange color shading, indicating its typical spectral power density in reanalysis. The control run's spectra display a much weaker signal in this region. Conversely, both the PRIME-MCSP and the PRIME-MCSP variable α runs more successfully capture this spectral feature, indicating a more accurate representation of the MJO, with the PRIME-MCSP run exhibiting the closest match to reanalysis. Additionally, the Kelvin wave intensity is overestimated in the control run with the CoMorph-A convection scheme, but this overestimation is mitigated in the PRIME-MCSP run. This suggests that PRIME-MCSP might be promising in mitigating the pre-existing spectral bias inherited from the convection parameterization.

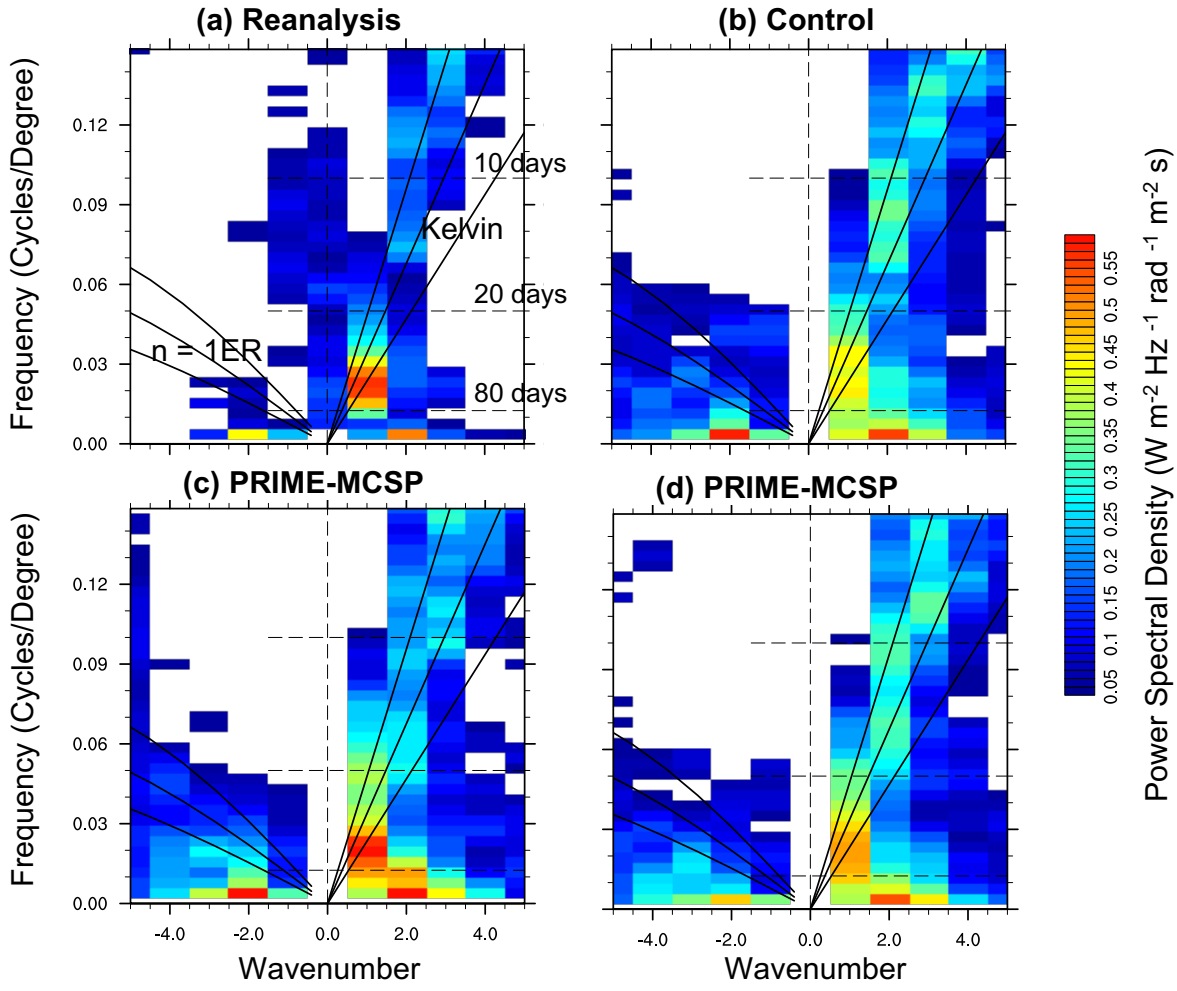

Figure 13. Symmetric wave cross spectra derived from OLR and zonal wind. The dashed lines, from top to bottom, indicate wave periods of 10, 20, and 80 days, respectively. The three black

lines on the left and right sides denote Equatorial Rossby (ER) waves and Kelvin waves, respectively. a) Reanalysis, b) Control simulation, c) PRIME-MCSP simulation, d) PRIME-MCSP variable α simulation. All simulations and observations span September 1988 to August 2008.

The MJO index is calculated following Wheeler and Hendon (2004) approach, which uses 15°S to 15°N averaged 850-hPa zonal wind, 200-hPa zonal wind, and OLR at the TOA. These daily fields in the reanalysis, control, PRIME-MCSP, and PRIME-MCSP variable α runs are filtered to leave the 20–100 days MJO components, before they are projected onto the same multiple-variable Empirical Orthogonal Functions computed from the reanalysis data. Two principal components are derived to depict the east-west and north-south progression of the MJO. The magnitude of the vector formed by these components serves as the MJO index, indicating the intensity of the MJO. When the MJO index exceeds a value of 1, these components are employed to categorize data into eight MJO phases, reflecting the spatial and temporal evolution of the MJO lifecycle.

Wintertime (November to April) MJO lifecycle composite maps are shown in Figure 14, again generated by ESMValTool. These maps use darker blue shading to indicate decreases in OLR, highlighting phases of enhanced rainfall and large-scale upward motion associated with the MJO. The sequence from Phase 1 (P1) to Phase 8 (P8) in Figure 14a illustrates the MJO's eastward propagation through its various phases in the reanalysis, with a consistent movement across the Maritime Continent. The control run (Figure 14b), however, shows discrepancies in capturing this propagation, particularly during Phase 6 (P6) when the anomaly dissipates too readily. The PRIME-MCSP and PRIME-MCSP variable α runs (Figure 14 c–d) both improve upon the control run's performance, with the former better at representing OLR anomalies before the MJO reaches the Maritime Continent and the latter being more accurate afterwards. Notably, the PRIME-MCSP variable α run depicts enhanced accuracy in P6, capturing the two strong centers of OLR anomalies over the Maritime Continent. This demonstrates the PRIME-MCSP scheme's effectiveness in improving MJO characteristics, aligning with findings from prior studies (e.g., Chen et al., 2021) and suggests sensitivity to variations of α in capturing spectral density and MJO lifecycles.

To quantify differences in wintertime MJO activity across the climate runs, histogram distributions of the MJO index are analyzed. A strong MJO event is defined as having an index greater than 1. According to this definition, the number of strong MJO events can vary between reanalysis and model runs. The control run exhibits too many weak MJO events (index less than one), as shown in Figure 15a. The PRIME-MCSP run reduces the occurrence of these weaker events (Figure 15b) while increasing the frequency of stronger events, indicating a mitigation of model biases in overestimating weak MJOs and underestimating strong MJOs. To assess the significance of Figure 15b, a Monte Carlo test was conducted, calculating the probability of changes in the 20-year total number of MJO occurrences between the control and the PRIME-MCSP run. This calculation was based on 100,000 resamplings using their respective annual counts of weak (index less than one) and strong (index greater than one) MJO occurrences. The significance test revealed that both the decrease in weak MJO occurrences and the increase in strong MJO occurrences are statistically significant, with p-values exceeding 94%. The comparison between the PRIME-MCSP run and reanalysis (Figure 15c) shows a closer alignment than that between the control run and reanalysis. The PRIME-MCSP variable α run

similarly improves the MJO index histogram distribution, aligning closely with reanalysis data (Figure 15d).

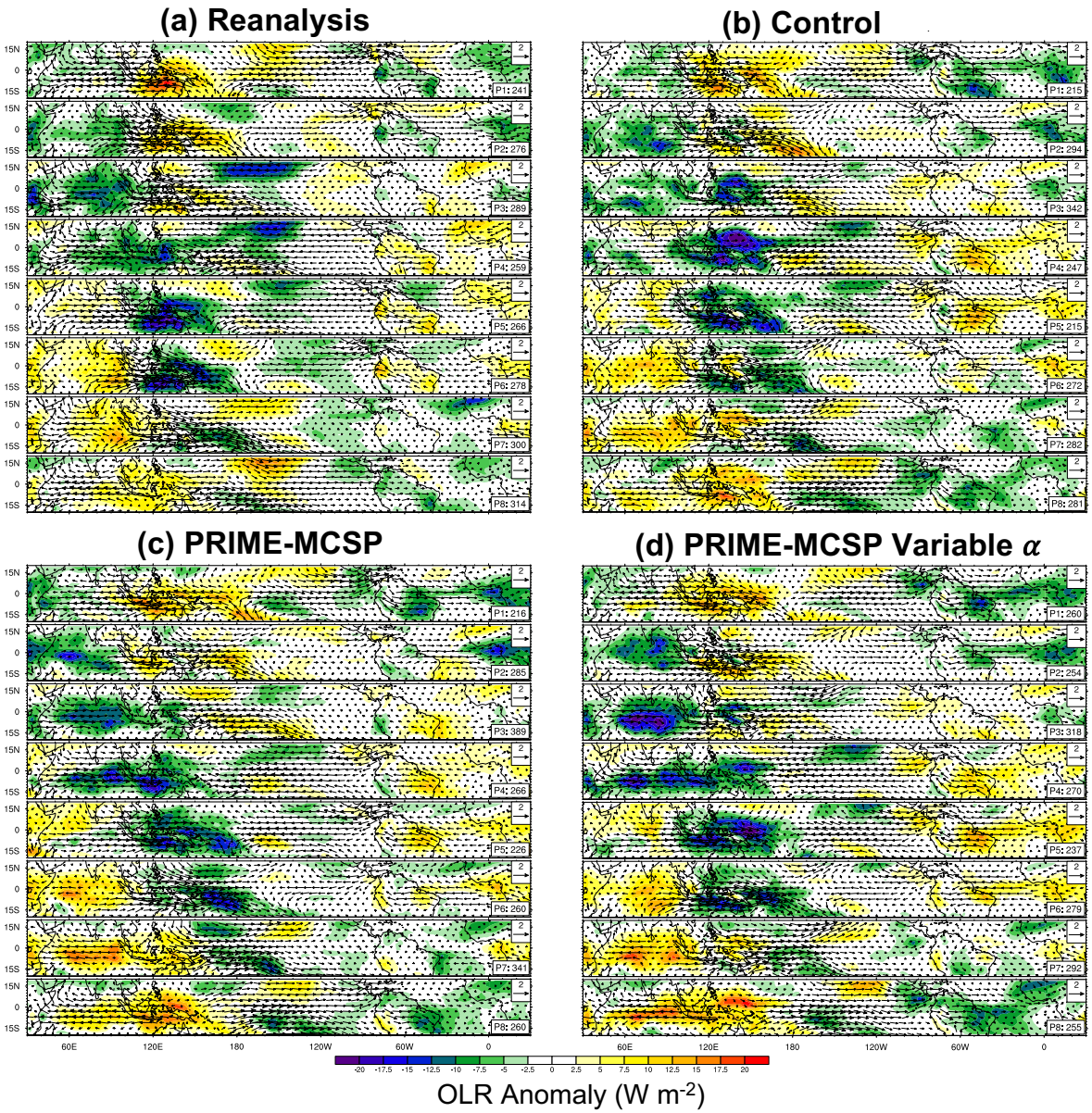

Figure 14. Wintertime (November–April) MJO lifecycle composites across different model runs: (a) Reanalysis, (b) Control, (c) PRIME-MCSP, and (d) PRIME-MCSP Variable α. The color shading indicates the OLR anomalies. Wind vectors represent the 850 hPa wind field. The subpanels, labeled P1 through P8, depict the sequential phases of the MJO lifecycle and the number of days identified as that phase, used to create the composite. All simulations and observations span September 1988 to August 2008.

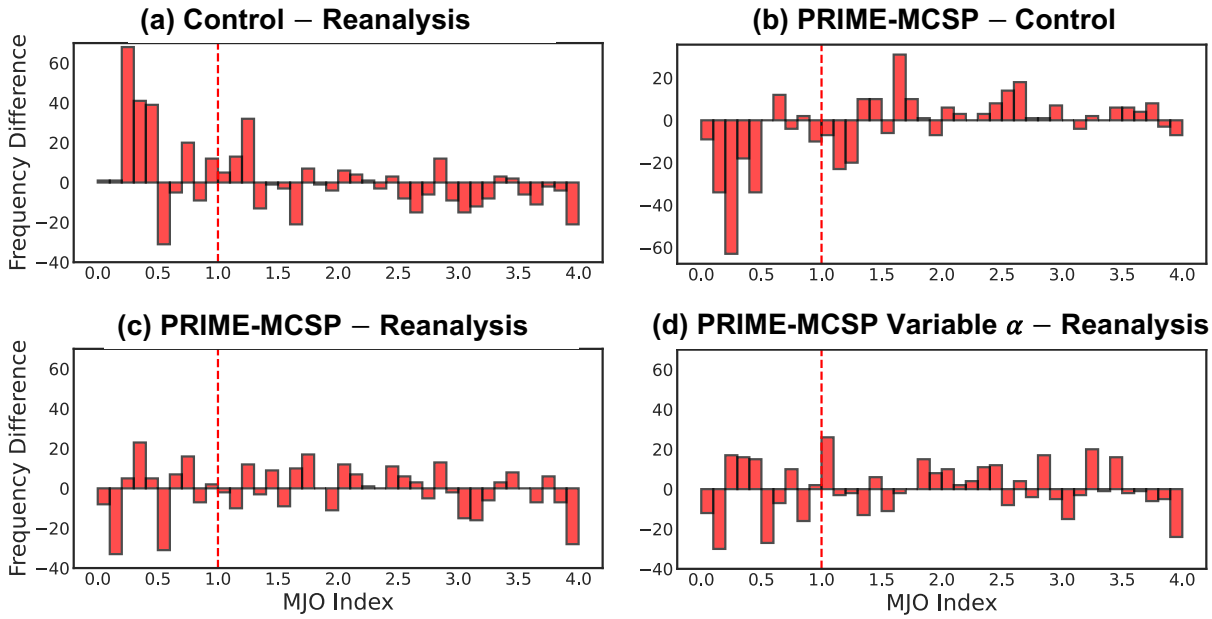

596

597 **Figure 15.** Comparative histogram distributions of wintertime (November–April) MJO index
598 differences. (a) between the control run and reanalysis, (b) PRIME-MCSP run versus control run,
599 (c) PRIME-MCSP run against reanalysis, and (d) PRIME-MCSP variable α against reanalysis.
600 The value in each bin represents the total number of MJOs that occur during the winter over the
601 20 years and fall within the index range.

602 **6 Conclusions**

603 This study implements the organized convection parameterization PRIME-MCSP in the
604 Unified Model in order to represent the stratiform heating associated with MCS. The scheme
605 incorporates several improvements over previous studies including:

606 1) Specialization of MCSP triggers: The PRIME-MCSP scheme features specialized
607 triggers for mixed-phase deep convection, incorporating ice condensate production into its
608 determination of whether the stratiform increment should be applied. This is achieved by only
609 triggering the scheme if the cloud top is above the freezing level. 2) Variable heating
610 partitioning: The study explores both a constant and a variable convective-to-stratiform heating
611 partitioning in the scheme, the latter being conditioned by cloud top temperature. 3) Leveraging
612 the mass-flux convection parameterization: The scheme's coupling with the Comorph-A scheme
613 is well suited to an MCS representation because CoMorph-A has a smooth numerical behavior in
614 time because of its allows convecting air parcels to ascend from any level, thereby promoting
615 continuity in the MCS evolution.

616 The scheme's evaluation is a comprehensive analysis of both its direct effects in weather
617 ensembles and its indirect effects in decadal simulations.

618 Direct effects: through an innovative use of MCS tracking, we showed that the scheme
619 acts to suppress MCS deepening and reduce MCS precipitation area. This is attributed to the
620 weakening of low-level mesoscale circulations associated with suppressed convective updrafts in
621 response to the stratiform lower-tropospheric cooling.

Indirect Effects: 20-year climate simulations assess the scheme's long-term impact, exhibiting a general agreement with global observed MCS frequencies, with regional variations over the tropical regions. Key results include 1) a reduction in precipitation bias across the Maritime time continent, effectively mitigating the dry bias over India and wet bias over the Indian Ocean; 2) The precipitation bias reduction is associated with a significant improvement in the representation of the precipitation seasonal cycle over the Indian and Indian Ocean, correcting a systematic bias observed across CMIP6 ensemble members; and 3) These precipitation improvements could be linked to the scheme's improvement on MJO spectra, aligning more closely with the reanalysis dataset by enhancing MJO intensity and continuing MJO eastward propagation during the post-Maritime Continent transit.

Despite these advances, the scheme's tendency to overestimate precipitation over the Western Pacific remains a challenge, echoing limitations in prior MCSP implementations (e.g., Moncrieff et al. 2019). Over the Western Pacific, Liu & Moncrieff (2017) found that MCS ascending airflows are often parallel to the environmental wind shear, in contrast with MCSP's slantwise layer overturning assumption. This suggests that the MCSP slantwise layer overturning paradigm might not apply to all MCSs. Additionally, the exploration of variable convective and stratiform partitioning proved to be a successful bias mitigation strategy over the Western Pacific but inadvertently reduced the improved precipitation representation over India and the Indian Ocean, indicating a spatially correlated bias pattern. Notably, Khouider et al. (2023) suggested that stochastic parameterization could potentially improve the representation of convective organization by refining the predicted mass flux of convective updrafts. This presents intriguing possibilities for future investigations into the stochastic parameterization of MCSP triggering and convective-to-stratiform partitioning probabilities, conditioned by various environmental patterns (Muetzelfeldt et al, 2024), which might reduce the Western Pacific's wet bias while maintaining the desirable improvements to seasonal precipitation predictability over India and the Indian Ocean.

Acknowledgments

This research is supported by the UK Research and Innovation (UKRI) Natural Environment Research Council (NERC) grant number NE/W005530/1 "Mesoscale Convective Systems: PRobabilistic forecasting and upscale IMpacts in the grey zonE (MCS: PRIME)". HMC was also funded by NERC grant number NE/P018238/1. Weather ensemble runs and decadal climate simulations were performed on the Monsoon2, a joint supercomputer system of the Met Office and NERC. Scheme assessments were carried out on the JASMIN UK high-performance computing clusters, funded by the Science and Technology Facilities Council on behalf of NERC. We extend our gratitude to Dr. Anne McCabe and Dr. Adrian Lock from the UK Met Office for their invaluable support in providing the necessary setup to conduct the Unified Model runs.

Open Research

Monthly global precipitation data are provided by the Global Precipitation Climatology Project (GPCP) at the National Center for Atmospheric Research (NCAR), available at https://climatedataguide.ucar.edu/climate-data/gpcp-monthly-global-precipitation-climatology-

project. CMIP6 simulated precipitation datasets are accessible via https://pcmdi.llnl.gov/CMIP6/. The observed global storm tracks dataset is available at https://doi.org/10.5281/zenodo.4244985. MCS tracks are generated using the PyFLEXTRKR software, available at https://github.com/FlexTRKR/PyFLEXTRKR. NCEP reanalysis data can be found at https://psl.noaa.gov/data/gridded/data.ncep.reanalysis.html. Please contact the authors directly for access to the PRIME-MCSP scheme and the model runs.

References

Barnes, H. C., M. D. Zuluaga, and R. A. Houze Jr. (2015), Latent heating characteristics of the MJO computed from TRMM observations, *J. Geophys. Res. Atmos.*, **120**, 1322–1334, doi:10.1002/2014JD022530

Becker, T., Bechtold, P., & Sandu, I. (2021). Characteristics of convective precipitation over tropical Africa in storm-resolving global simulations. *Quarterly Journal of the Royal Meteorological Society*, **147**(741), 4388–4407. https://doi.org/10.1002/qj.4185

Bush, S. J., Turner, A. G., Woolnough, S. J., Martin, G. M., & Klingaman, N. P. (2015). The effect of increased convective entrainment on Asian monsoon biases in the MetUM general circulation model. *Quarterly Journal of the Royal Meteorological Society*, **141**(686), 311–326. https://doi.org/10.1002/qj.2371

Bush, M., Boutle, I., Edwards, J., Finnenkoetter, A., Franklin, C., Hanley, K., et al. (2022). The second met office unified model/jules regional atmosphere and land configuration, RAL2. Geoscientific Model Development Discussions, 2022, 1–35. https://doi.org/10.5194/gmd-2022-209

Chen, C. C., Richter, J. H., Liu, C., Moncrieff, M. W., Tang, Q., Lin, W., et al. (2021). Effects of Organized Convection Parameterization on the MJO and Precipitation in E3SMv1. Part I: Mesoscale Heating. *Journal of Advances in Modeling Earth Systems*, ***13***(6). https://doi.org/10.1029/2020MS002401

Cheng, C. P., & Houze, R. A. (1979). The distribution of convective and mesoscale precipitation in GATE radar echo patterns. *Monthly Weather Review*, ***107***(10). https://doi.org/10.1175/1520-0493(1979)107<1370:TDOCAM>2.0.CO;2

Daleu, C. L., Plant, R. S., Stirling, A. J., & Whitall, M. (2023). Evaluating the CoMorph-A parametrization using idealized simulations of the two-way coupling between convection and large-scale dynamics. *Quarterly Journal of the Royal Meteorological Society,* **149**(757), 3087–3109. https://doi.org/10.1002/qj.4547

Davies, T., Cullen, M. J. P., Malcolm, A. J., Mawson, M. H., Staniforth, A., White, A. A., and Wood, N. (2005), A new dynamical core for the Met Office's global and regional modelling of the atmosphere, *Quarterly Journal of the Royal Meteorological Society*, **131**(608), 1759–1782

Eyring, V., Bony, S., Meehl, G. A., Senior, C. A., Stevens, B., Stouffer, R. J., and Taylor, K. E. (2016). Overview of the Coupled Model Intercomparison Project Phase 6 (CMIP6) experimental design and organization. *Geoscientific Model Development*, **9**, 1937–1958, https://doi.org/10.5194/gmd-9-1937-2016

Eyring, V., Righi, M., Lauer, A., Evaldsson, M., Wenzel, S., Jones, C., Anav, A., Andrews, O., Cionni, I., Davin, E. L., Deser, C., Ehbrecht, C., Friedlingstein, P., Gleckler, P., Gottschaldt, K.-D., Hagemann, S., Juckes, M., Kindermann, S., Krasting, J., Kunert, D., Levine, R., Loew, A., Mäkelä, J., Martin, G., Mason, E., Phillips, A. S., Read, S., Rio, C., Roehrig, R., Senftleben, D., Sterl, A., van Ulft, L. H., Walton, J., Wang, S., Williams, K. D. (2016). ESMValTool (v1.0)—A community diagnostic and performance metrics tool for routine evaluation of Earth system models in CMIP. *Geoscientific Model Development*, **9**(5), 1747–1802. https://doi.org/10.5194/gmd-9-1747-2016

Feng, Z., Leung, L. R., Liu, N., Wang, J., Houze, R. A., Li, J., et al. (2021). A global high-resolution mesoscale convective system database using satellite-derived cloud tops, surface precipitation, and tracking. *Journal of Geophysical Research: Atmospheres*, **126**(8). https://doi.org/10.1029/2020JD034202

Feng, Z., Hardin, J., Barnes, H. C., Li, J., Leung, L. R., Varble, A., & Zhang, Z. (2023). PyFLEXTRKR: A flexible feature tracking Python software for convective cloud analysis. *Geoscientific Model Development*, **16**, 2753–2776. https://doi.org/10.5194/gmd-16-2753-2023

Han, B., Fan, J., Varble, A., Morrison, H., Williams, C. R., Chen, B., et al. (2019). Cloud-Resolving model intercomparison of an MC3E squall line case: Part II. Stratiform precipitation properties. *Journal of Geophysical Research: Atmospheres*, **124**(2), 1090–1117. https://doi.org/10.1029/2018JD029596

Hartmann, D. L., H. H. Hendon, and R. A. Houze Jr. (1984), Some implications of the mesoscale circulations in tropical cloud clusters for large-scale dynamics and climate, J. Atmos. Sci., 41, 113–121. https://doi.org/10.1175/1520-0469(1984)041<0113:SIOTMC>2.0.CO;2

Hoell, A., Cannon, F., & Barlow, M. (2018). Middle East and Southwest Asia daily precipitation characteristics associated with the Madden–Julian Oscillation during Boreal Winter. *Journal of Climate*, **31**(21), 8843–8860. https://doi.org/10.1175/JCLI-D-18-0059.1

Houze, R. A., Smull, B. F., & Dodge, P. (1990). Mesoscale organization of springtime rainstorms in Oklahoma. *Monthly Weather Review*, ***118***(3). https://doi.org/10.1175/1520-0493(1990)118<0613:MOOSRI>2.0.CO;2

Houze, Robert A. (1989). Observed structure of mesoscale convective systems and implications for large-scale heating. *Quarterly Journal of the Royal Meteorological Society*, ***115***(487). https://doi.org/10.1002/qj.49711548702

Houze, R. A. (2004), Mesoscale convective systems, *Reviews of Geophysics*, **42**, RG4003, doi:10.1029/2004RG000150

Houze Jr, R. A. (2018). 100 years of research on mesoscale convective systems. *Meteorological Monographs*, 59, 17–1. https://doi.org/10.1175/AMSMONOGRAPHS-D-18-0001.1

Inverarity, G. W., Tennant, W. J., Anton, L., Bowler, N. E., Clayton, A. M., Jardak, M., Lorenc, A. C., Rawlins, F., Thompson, S. A., Thurlow, M. S., Walters, D. N., & Wlasak, M. A. (2023), Met Office MOGREPS-G initialisation using an ensemble of hybrid four-dimensional ensemble variational (En-4DEnVar) data assimilations, *Quarterly Journal of the Royal Meteorological Society*, **149**(753), 1138–1164, https://doi.org/10.1002/qj.4431

Kalnay, E., Kanamitsu, M., Kistler, R., Collins, W., Deaven, D., Gandin, L., et al. (1996). The NCEP/NCAR 40-year reanalysis project [Dataset]. *Bulletin of the American Meteorological Society*, **77**(3), 437–472. https://doi.org/10.1175/1520-0477(1996)077<0437:TNYRP>2.0.CO;2

Khouider, B., Goswami, B. B., Phani, R., & Majda, A. J. (2023). A shallow-deep unified stochastic mass flux cumulus parameterization in the single column Community Climate Model. *Journal of Advances in Modeling Earth Systems*, **15**, e2022MS003391. https://doi.org/10.1029/2022MS003391

Kooperman, G. J., Pritchard, M. S., & Somerville, R. C. J. (2014). The response of US summer rainfall to quadrupled CO2 climate change in conventional and superparameterized versions of the NCAR community atmosphere model. *Journal of Advances in Modeling Earth Systems*, **6**(3), 859–882. https://doi.org/10.1002/2014MS000306

Lauer, A., Bock, L., Hassler, B., Schröder, M., & Stengel, M. (2023). Cloud climatologies from global climate models—A comparison of CMIP5 and CMIP6 models with satellite data. *Journal of Climate*, **36**(2), 281–311. https://doi.org/10.1175/JCLI-D-22-0181.1

Lavender, S. L., Stirling, A. J., Whitall, M., Stratton, R., Daleu, C. L., Plant, R. S., Lock, A. & Gu, J.-F. (2024) The use of idealised experiments in testing a new convective parameterization: Performance of CoMorph-A. To appear in: *Quarterly Journal of the Royal Meteorological Society*. https://doi.org/10.1002/qj.4660

Leary, C. A., & Houze, R. A. (1979). Melting and evaporation of hydrometeors in precipitation from the anvil clouds of deep tropical convection. *Journal of the Atmospheric Sciences*, ***36***(4), 669–679. https://doi.org/10.1175/1520-0469(1979)036<0669:MAEOHI>2.0.CO;2

Liu, C. & Moncrieff, M. W. (2017) Shear-parallel mesoscale convective systems in a moist low-inhibition Mei-Yu front environment. *Journal of the Atmospheric Sciences*, **74**(12), 4213–4228. https://doi.org/10.1175/JAS-D-17-0121.1

Moncrieff, M. W. (2019). Toward a dynamical foundation for organized convection parameterization in GCMs. *Geophysical Research Letters*, **46**(14),103–14,108. https://doi.org/10.1029/2019GL085316

Moncrieff, M. W., & Liu, C. (2006). Representing convective organization in prediction models by a hybrid strategy. *Journal of the Atmospheric Sciences*, **63**(12). https://doi.org/10.1175/JAS3812.1

Moncrieff, M. W., Liu, C., & Bogenschutz, P. (2017). Simulation, modeling, and dynamically based parameterization of organized tropical convection for global climate models. *Journal of the Atmospheric Sciences*, **74**(5). https://doi.org/10.1175/JAS-D-16-0166.1

Muetzelfeldt, M. R., Plant, R. S., Christensen, H. M., Zhang, Z., Woollings, T., Feng, Z. & Li, P. (2024), Environmental Conditions Affecting Global Mesoscale Convective System Occurrence. Submitted to: *Journal of the Atmospheric Sciences*

Pendergrass, A. &, Wang, J. & National Center for Atmospheric Research Staff (Eds). Last modified 2022-11-07 "The Climate Data Guide: GPCP (Monthly): Global Precipitation Climatology Project." Retrieved from https://climatedataguide.ucar.edu/climate-data/gpcp-monthly-global-precipitation-climatology-project on 2024-03-13

Prein, A. F., Liu, C., Ikeda, K., Bullock, R., Rasmussen, R. M., Holland, G. J., & Clark, M. (2020). Simulating North American mesoscale convective systems with a convection-permitting climate model. *Climate Dynamics*, **55**(1), 95–110. https://doi.org/10.1007/s00382-017-3993-2

Rushley, S. S., Kang, D., Kim, D., An, S.-I., & Wang, T. (2023). MJO in different orbital regimes: Role of the mean state on the MJO's amplitude during boreal winter. *Journal of Climate*, **36**(13), 1–41. https://doi.org/10.1175/JCLI-D-22-0725.1

Schumacher, C., Houze, R. A., & Kraucunas, I. (2004). The Tropical Dynamical Response to Latent Heating Estimates Derived from the TRMM Precipitation Radar. *Journal of the Atmospheric Sciences*, **61**(12), 1341–1358. https://doi.org/10.1175/1520-0469(2004)061<1341:TTDRTL>2.0.CO;2

Schumacher, R. S., & Rasmussen, K. L. (2020). The formation, character and changing nature of mesoscale convective systems. *Nature Reviews Earth & Environment*, **1**, 300–314. https://doi.org/10.1038/s43017-020-0057-7

Varble, A., Zipser, E. J., Fridlind, A. M., Zhu, P., Ackerman, A. S., Chaboureau, J.-P., Collis, S., et al. (2014). Evaluation of cloud-resolving and limited area model intercomparison simulations using TWP-ICE observations: 1. Deep convective updraft properties. *Journal of Geophysical Research: Atmospheres*, **119**(24), 13,891–13,918. https://doi.org/10.1002/2013JD021371

Varble, A., Zipser, E. J., Fridlind, A. M., Zhu, P., Ackerman, A. S., Chaboureau, J.-P., et al. (2014b). Evaluation of cloud-resolving and limited area model intercomparison simulations using TWP-ICE observations: 2. Precipitation microphysics. *Journal of Geophysical Research: Atmospheres*, **119**(24), 13919–13945. https://doi.org/10.1002/2013JD021372

Walters, D., Baran, A. J., Boutle, I., Brooks, M., Earnshaw, P., Edwards, J., Furtado, K., Hill, P., Lock, A., Manners, J., & Morcrette, C. (2019). The Met Office Unified Model global atmosphere 7.0/7.1 and JULES global land 7.0 configurations. *Geoscientific Model Development*, **12**(5), 1909–1963.

Wheeler, M. C., & Hendon, H. H. (2004). An all-season real-time multivariate MJO index: Development of an index for monitoring and prediction. *Monthly Weather Review*, **132**(8), 1917–1932. https://doi.org/10.1175/1520-0493(2004)132<1917:AARMMI>2.0.CO;2

Wheeler, M., and G. N. Kiladis (1999), Convectively coupled equatorial waves: Analysis of clouds and temperature in the wavenumber-frequency domain, *Journal of the Atmospheric Sciences*, **56**, 374–399.

Whitall, M., Stirling, A., Lock, A., Lavender, S., Stratton, R. & Matsubayashi, K. (2022) The CoMorph convection scheme. UM Documentation Paper 043.

Yang, G.-Y., & Slingo, J. (2001). The diurnal cycle in the tropics. *Monthly Weather Review*, **129**(4), 784–801. https://doi.org/10.1175/1520-0493(2001)129<0784:TDCITT>2.0.CO;2

Zhang, G. J., & McFarlane, N. A. (1995). Sensitivity of climate simulations to the parameterization of cumulus convection in the Canadian climate centre general

827 circulation model. *Atmosphere - Ocean*, **33**(3).
828 https://doi.org/10.1080/07055900.1995.9649539

829 Zhang, Z., Varble, A., Feng, Z., Hardin, J., & Zipser, E. (2021). Growth of mesoscale convective
830 systems in observations and a seasonal convection-permitting simulation over Argentina.
831 *Monthly Weather Review*, **149**(10), 3469–3490. https://doi.org/10.1175/MWR-D-20-
832 0411.1

833 Zhang, Z., Varble, A., Feng, Z., Marquis, J., Hardin, J., & Zipser, E. (2024). Dependencies of
834 Simulated Convective Cell and System Growth Biases on Atmospheric Instability and
835 Model Resolution. Submitted to *Journal of Geophysical Research: Atmospheres*.

Advancing Organized Convection Representation in the Unified Model: Implementing and Enhancing Multiscale Coherent Structure Parameterization

Zhixiao Zhang[1], Hannah M. Christensen[1], Mark R. Muetzelfeldt[2], Tim Woollings[1], Robert S. Plant[2], Alison J. Stirling[3], Michael A. Whitall[3], Mitchell W. Moncrieff[4], Chih-Chieh Chen[4], and Zhe Feng[5]

[1]Department of Physics, University of Oxford, Oxford, Oxfordshire, UK.

[2]Department of Meteorology, University of Reading, Reading, Berkshire, UK.

[3]Met Office, Exeter, Devon, UK.

[4]Climate and Global Dynamics Division, National Center for Atmospheric Research, Boulder, Colorado, USA.

[5]Atmospheric, Climate, and Earth Sciences Division, Pacific Northwest National Laboratory, Richland, Washington, USA.

Corresponding author: Zhixiao Zhang (zhixiao.zhang@physics.ox.ac.uk)

Key Points:

- Organized convection scheme with realistic triggering and state-dependent partitioning between stratiform and convective heating is proposed
- Scheme leads to reduced storm area and shallower parameterized convection through lower-troposphere cooling from stratiform precipitation
- Scheme corrects systematic precipitation biases over India and the Indian Ocean through intensifying the Madden-Julian Oscillation

Abstract

To address the effect of stratiform latent heating on meso- to large scale circulations, an enhanced implementation of the Multiscale Coherent Structure Parameterization (MCSP) is developed for the Met Office Unified Model. MCSP represents the top-heavy stratiform latent heating from under-resolved organized convection in general circulation models. We couple the MCSP with a mass-flux convection scheme (CoMorph-A) to improve storm lifecycle continuity. The improved MCSP trigger is specifically designed for mixed-phase deep convective cloud, combined with a background vertical wind shear, both known to be crucial for stratiform development. We also test a cloud top temperature dependent convective-stratiform heating partitioning, in contrast to the earlier fixed partitioning. Assessments from ensemble weather forecasts and decadal simulations demonstrate that MCSP directly reduces cloud deepening and precipitation areas by moderating mesoscale circulations. Indirectly, it amends tropical precipitation biases, notably correcting dry and wet biases over India and the Indian Ocean, respectively. Remarkably, the scheme outperforms a climate model ensemble by improving seasonal precipitation cycle predictions in these regions. This enhancement is partly due to the scheme's refinement of Madden-Julian Oscillation (MJO) spectra, achieving better alignment with reanalysis data by intensifying MJO events and maintaining their eastward propagation after passing the Maritime Continent. However, the scheme also increases precipitation overestimation over the Western Pacific. Shifting from fixed to temperature-dependent convective-stratiform partitioning reduces the Pacific precipitation overestimation but also lessens the improvements of seasonal cycle in India. Spatially correlated biases highlight the necessity for advancements beyond deterministic approaches to align MCSP with environmental conditions.

Plain Language Summary

We improve a key component of the Met Office's climate model to better represent how widespread light rain in severe convective storms affects atmospheric patterns. We make the representation respond to different temperatures at the tops of clouds, which is a new approach compared to previous studies where the heavy-to-light rain partitioning was assumed constant. We find that the improved representation of the light rain associated with severe storms reduces the overall storm rainfall area and suppresses storm height. The changes are particularly effective in correcting rainfall forecasts in tropical regions like India and the Indian Ocean, outperforming other climate models. Notably, our model excels at predicting specific tropical climate patterns, enhancing wind and rainfall accuracy over the Maritime Continent. However, our model predicts too much rain over the Western Pacific. When we adjust how we calculate the heavy-to-light rain partitioning based on cloud top temperatures, it reduces this overestimation but also weakens our improvements elsewhere. This indicates that we need to keep exploring new approaches to consider the light rain probability in severe storms.

1 Introduction

Organized convection encompasses two distinct types of precipitation: intense convective precipitation, and quasi-steady, lighter stratiform precipitation, with this differentiation observed in both tropical (Cheng & Houze, 1979) and extratropical regions (Houze et al., 1990). The variation in organized convection, encompassing a spectral mix rather than a simple spatial separation between convective and stratiform precipitation, presents a significant challenge in weather and climate prediction (Schumacher & Rasmussen, 2020), as these precipitation types

differ substantially in redistributing moisture, momentum, and heat in the atmosphere (Houze, 2004). One representative type of organized convection is a Mesoscale Convective System (MCS), which has a length scale exceeding 100 km in at least one direction (Houze 2004).

A fundamental distinction lies in the vertical profile of latent heating. In convective regions, intense updrafts induce rapid condensation, resulting in a bottom-heavy heating profile marked by a concentration of heating in the lower and middle troposphere (Houze, 1989). Conversely, in stratiform regions, the majority of latent heating occurs higher up, usually in the upper troposphere above the freezing level (Houze, 1989). This heating aloft is predominantly driven by the deposition of vapor into ice, a process facilitated by ice hydrometeors transported from convective regions (Han et al., 2019). Additionally, most stratiform regions exhibit net latent cooling below the freezing level, resulting from weaker updrafts and reduced local condensate production. This leads to insufficient condensational heating in the lower troposphere to counteract cooling from microphysical processes such as ice melting and raindrop evaporation (Leary & Houze, 1979). These dynamical and microphysical processes collectively lead to a top-heavy heating profile in stratiform regions (Houze, 1989; Schumacher et al., 2004).

A higher ratio of stratiform to convective partitioning leads to more top-heavy latent heating, crucially reshaping large-scale atmospheric circulations (Houze, 2018). For example, satellite observations show a sharp increase in stratiform precipitation and its associated top-heavy latent heating during the active stage of the Madden-Julian Oscillation (MJO) over the Western Pacific (Barnes et al., 2015). The spatial variability of the El Niño-Southern Oscillation (ENSO) is significantly influenced by the gradient of the stratiform fraction over the Pacific (Schumacher et al., 2004). Additionally, a greater stratiform fraction aids the propagation of large-scale waves from the tropics to extra-tropical regions, a phenomenon also highlighted in the same study. Incorporating stratiform latent heating in simulations notably elevates the center of the Walker cell, enhancing its alignment with observations (Hartmann et al., 1984). Overall, the more top-heavy the latent heating profile is, the stronger the upscaling feedback becomes from organized convection to large-scale atmospheric circulations (Houze, 2018).

However, it is difficult to represent top-heavy stratiform heating in weather and climate models due to its dependence on multiscale processes (Schumacher & Rasmussen, 2020), ranging from microphysics and convective drafts to mesoscale and large-scale circulations. Climate models with coarse resolution utilizing convection parameterizations often fail to represent mesoscale circulations within organized convection (Kooperman et al., 2015). Convection-permitting models with computational grids of a few kilometers partially represent mesoscale circulations yet tend to overestimate convective precipitation (e.g., Becker et al. 2021) and updraft intensity (Varble et al., 2014), and underestimate stratiform fractions (Prein et al., 2020). Specifically, overly-intense updrafts are too efficient in producing rimed ice and precipitating moisture in convective regions, resulting in fewer ice hydrometers aloft for feeding stratiform precipitation (Varble et al., 2014; Zhang et al., 2021). Even when model grid spacings reach large-eddy resolutions, the overestimation in the partitioning of convective and stratiform precipitation persists (Zhang et al., 2024). This indicates that improving stratiform precipitation representation requires more than just better resolved dynamics. Effective representation demands a coherent paradigm that spans multiple scales.

To mitigate such biases, a promising strategy developed in past studies (Chen et al., 2021; Moncrieff, 2019; Moncrieff et al., 2017; Moncrieff & Liu, 2006) is the Multiscale Coherent Structure Parameterization (MCSP). This scheme posits that the stratiform heating aloft

and lower-level cooling are directly proportional to the column-integrated convective heating estimated by a convection parameterization. The scheme is typically triggered in situations where the grid-scale winds promote slantwise layer overturning, which favors the partially-resolved organization of convection for generating stratiform latent heating (Moncrieff & Liu, 2006). Incorporating top-heavy latent heating profiles associated with organized convection through the MCSP scheme enhances the capability of general circulation models to simulate the observed MJO, as evidenced by studies from Chen et al. (2021) and Moncrieff et al. (2017) for the E3SM and CAM models respectively. Moreover, the MCSP scheme contributes to an improvement in the representation of Kelvin wave spectra and a reduction in biases associated with tropical precipitation (Chen et al., 2021).

The coupling method between convection parameterization and the MCSP scheme presents opportunities for improvement. The recent implementation of MCSP by Moncrieff et al. (2017) employs the Zhang-McFarlane convection scheme (Zhang & McFarlane, 1995), using a rate of change of Convective Available Potential Energy (CAPE) threshold as the trigger for the convection scheme. However, this CAPE-based trigger can be disrupted by the introduction of stratiform aloft heating and lower-level cooling by MCSP. Such disruption may compromise the temporal continuity of both the convection and MCSP schemes, possibly leading to intermittent or on-off behavior for either or both schemes. In addition, shallower convective systems, especially those at or below the freezing level that do not efficiently produce ice hydrometeors for stratiform precipitation, might not be associated with MCS, such that the MCSP scheme is inappropriately triggered for those cases. An improvement is needed to specifically target those deep convective systems that efficiently produce stratiform components for coupling with the MCSP scheme.

A second limitation with previous implementations of MCSP is the partitioning between stratiform and convective heating. Past studies have assumed a fixed partitioning (e.g., 50%) between stratiform and convective heating. However, this does not necessarily reflect real-world conditions, where the influence of stratiform precipitation can vary significantly due to the melting of ice hydrometeors from convection regions. A suitably-varying stratiform to convective heating partitioning could offer a more realistic representation.

Aiming to progress beyond existing methods, this research is guided by the following objectives: 1) Couple the MCSP with advanced convection parameterization techniques to improve storm-lifecycle continuity and facilitate storm-track based assessment. 2) Tailor MCSP triggering conditions specifically for deep convection. 3) Develop an environmentally-conditioned partitioning to effectively relate stratiform and convective heating processes. 4) Understand the scheme's direct effect in weather simulations spanning several days as well as its indirect effect in decadal simulations.

This study is carried out in the Met Office Unified Model, focusing on general circulation scales and is conducted as part of the Mesoscale Convective Systems: PRobabilistic forecasting and upscale IMpacts in the grey zonE (MCS: PRIME) project. The scheme, referred to as PRIME-MCSP, couples to a novel mass-flux convection scheme (CoMorph-A) that explicitly parameterizes convective detrainment and entrainment and smoothly transits between shallow and deep clouds (Whitall et al., 2022; Daleu et al., 2023; Lavender et al., 2024). A valuable feature of the CoMorph-A convection scheme for the current study is that it makes use of an implicit solver for its detrainment calculations. This contrasts with many other convection schemes, which can suffer from numerical overshoots and on-off behavior at the timestep level.

Moreover, CoMorph allows convection to be initiated from any layer in the vertical, depending on the instability at each level. At least partly for these reasons, the CoMorph-A approach enhances temporal-spatial continuity of precipitation clusters, capturing storm lifecycles in the presence of the stratiform heating aloft and lower-level cooling introduced by PRIME-MCSP. This improved continuity is crucial for enabling storm tracking, facilitating the lifecycle analysis of PRIME-MCSP's effect on the internal cloud dynamics and the surrounding environments.

To evaluate the effectiveness of PRIME-MCSP, short-term weather ensemble simulations and decadal climate simulations on a global scale are both conducted. The structure of the remaining sections is as follows: Section 2 details the design of the PRIME-MCSP scheme; Section 3 describes the simulations, observations, and methodology for storm tracking; Section 4 presents an analysis of the PRIME-MCSP impact throughout the lifecycle of MCSs using short-term ensemble runs; Section 5 examines the long-term climatic impacts of the PRIME-MCSP on large-scale precipitation patterns and the MJO in decadal simulations; and Section 6 summarizes the conclusions drawn from these analyses.

2 Parameterization Scheme

The PRIME-MCSP parameterization is designed to represent the stratiform latent heating profile associated with an MCS, which is otherwise missing in models. Drawing from Moncrieff et al. (2017), Figure 1a depicts a schematic of a slantwise layer overturning pattern of wind, highlighted by the black streamlines. Additionally, the schematic shows the vertical shear of horizontal wind via straight vectors on the right, indicating a transition from westerly winds in the lower troposphere to easterly winds in the mid-troposphere. Affected by this vertical wind shear, an unstable atmospheric layer rises, culminating in a central slantwise updraft that reaches the tropopause. This principal updraft then continues horizontally as an eastward flow, with the subsequent subsidence manifesting as a mesoscale downdraft on the right, while a subsidiary branch of the updraft diverges to the left at the top.

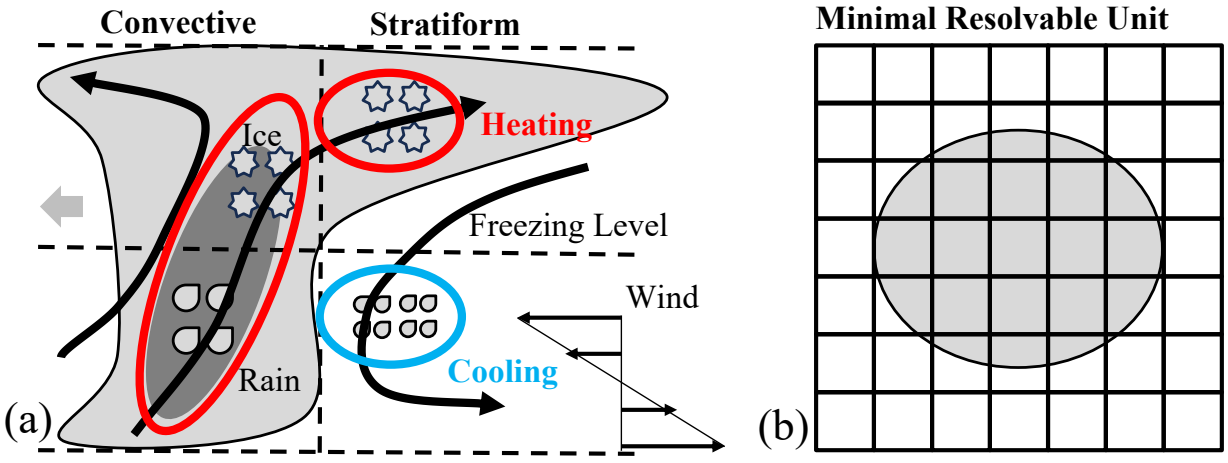

Figure 1. Schematic diagram for (a) stratiform and convective vertical cross sections in slantwise layer overturning scenario. Streamlines indicate wind directions. Red and blue circles represent the diabatic heating and cooling regions, respectively. The grey arrow represents the MCS propagation direction. Adapted from Moncrieff et al. (2017). (b) Top view of a 7 by 7 model-grid domain capable of minimally resolving the MCS (grey shading).

Figure 1a presents the dynamical correspondence with microphysical processes occurring within the convective and stratiform regions. The slantwise ascending layer in the center aligns with the convective region, where condensational heating is driven by updrafts loaded with raindrops below and ice condensates starting above the freezing level. The updrafts that curve horizontally to the right carry ice condensates aloft, aiding in the horizontal growth of the stratiform region. In the stratiform region, the ice condensates undergo depositional growth, which releases latent heat in the upper atmosphere. As these particles fall below the freezing level, they melt into raindrops. This melting process, followed by evaporation, induces cooling in the stratiform region's lower levels.

Figure 1b illustrates the MCS previously described in Figure 1a, highlighting its nature as an under-resolved phenomena for a given model resolution. Skamarock (2004) has shown that models are capable of resolving features with a minimum length scale approximately seven times the model's horizontal grid spacing. Thus, a climate model with a 100 km grid spacing could theoretically resolve MCS with a length scale of at least 700 km. However, a significant number of MCSs have at least one dimension shorter than this resolvable scale. For instance, Feng et al. (2021) demonstrated that more than 90% of MCSs over the continental United States have precipitation features shorter than 700 km, indicating a limitation in the model's ability to capture the full spectrum of MCS sizes. This complexity necessitates the use of the MCSP paradigm for multi-scale-coherent representation.

The potential temperature heating increment due to convective updrafts is parameterized by the CoMorph-A convection scheme, and denoted as $\Delta\theta_{CoMorph}$. Figure 2a shows an example temperature tendency profile from the CoMorph-A scheme: this is typically a net heating effect at nearly all height levels, aligning with the conceptual model in Figure 1a.

In an advancement over previous MCSP triggers, we have formulated triggering conditions that are designed to recognize slantwise layer overturning and mixed-phase deep clouds:

$$\left|\overrightarrow{V_{600}} - \vec{V_s}\right| > 3\ m\ s^{-1} \quad (1)$$

$$T_{top} < 0\ °C \quad (2)$$

$$p_{base} > 600\ hPa \quad (3)$$

$$p_{base} - p_{top} > 300\ hPa \quad (4)$$

Firstly, equation 1 identifies conditions suitable for slantwise layer overturning through the absolute value of the difference in horizontal wind speed between the surface and the 600hPa level. Note that Chen et al. (2021) computed only zonal wind shear when applying their triggering threshold, while this study computes wind shear based on both zonal and meridional wind components to depict the pattern of slantwise layer overturning. Secondly, the definition of mixed-phase deep cloud involves meeting three criteria, detailed in equations 2–4: 1) The cloud top temperature (T_{top}) must be below 0 °C, a threshold crucial for the production of ice condensates, which are key to generating stratiform precipitation. 2) The cloud base pressure (p_{base}) should be above 600 hPa, ensuring that there is adequate low-level moisture to support

and maintain deep convection. 3) The pressure difference between the cloud base and top ($p_{base} - p_{top}$) must exceed 300 hPa, confirming that the cloud has sufficient depth.

Building on Moncrieff (2017), the convective heating from CoMorph-A and the PRIME-MCSP stratiform heating are related through equations 5–7:

$$\overline{\overline{Q_{conv}}} = \frac{1}{p_s - p_{top}} \sum_{p_s}^{p_{top}} \Delta\theta_{CoMorph}(p) dp \quad (5)$$

$$Q_{strat}(p) = \alpha \sin\left(2\pi \frac{p_{top} - p}{p_s - p_{top}}\right) \overline{\overline{Q_{conv}}} \quad (6)$$

$$\alpha = 0.5 \text{ or } 0.5\left(\frac{T_{freeze} - T_{top}}{T_{freeze} - T_{ref}}\right) \quad (7)$$

where p_s and p_{top} represent the surface and cloud top pressure levels, respectively, while dp denotes the pressure difference between adjacent model levels. Equation 5 calculates the column-integrated convection scheme heating from the surface to the cloud top, normalized by the total pressure difference. Equation 6 posits that the amplitude of the stratiform aloft heating is proportional to the column-integrated convective heating and to a parameter α. The sinusoidal shape means that the column integral of stratiform heating aloft and low-level cooling balances out to approximately zero. Figure 2b illustrates the vertical distribution of the emulated stratiform latent heating that corresponds to the example CoMorph-A profile of Figure 2a.

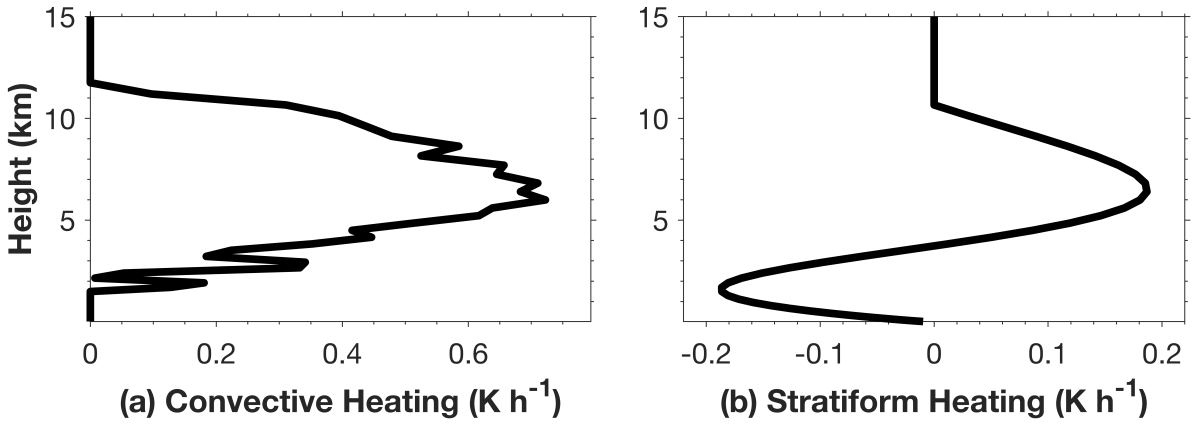

Figure 2. (a) Example tendency profile obtained from the CoMorph-A convection scheme, and (b) the corresponding stratiform tendency determined by PRIME-MCSP.

Previous studies (e.g., Chen et al. 2021) have used equation 6 with α set to a fixed value of 0.5. Here, we also consider a variable α dependent on the temperature difference between the freezing level T_{freeze} and the cloud top T_{top}, normalized by the temperature difference between T_{freeze} and a reference cloud top level T_{ref}, as shown in equation 7. The variable α is designed to reflect the idea that the growth of the stratiform region is proportional to the ice condensate flux from the convective to the stratiform region and that ice condensate production correlates with the temperature difference between the cloud top and the freezing level, indicated by Han et

al. (2019) and Zhang et al. (2024). T_{freeze} is set at 0°C, and T_{ref} to –80°C, representing the median value of the lifecycle-minimum cloud top temperature observed in global storm tracks (Feng et al., 2021).

The stratiform latent heating profile in equation 6 is intended to have a vertical integral of zero. However, due to the discrete nature of vertical levels in the model, a small residual may exist in practice. The residual in dry static energy is computed, and used to calculate the pressure-weighted residual error, denoted as $\overline{Q_{err}}$:

$$\overline{Q_{err}} = \frac{1}{p_s - p_{top}} \sum_{p_s}^{p_{top}} Q_{strat}(p) dp \quad (8)$$

The final potential temperature tendency $\Delta\theta_{org}(p)$ for a given grid at a specific level, resulting from the organized convection, is computed as the sum of $\Delta\theta_{CoMorph}(p)$ and $Q_{strat}(p)$, adjusted by subtracting $\overline{Q_{err}}$:

$$\Delta\theta_{org}(p) = \Delta\theta_{CoMorph}(p) + Q_{strat}(p) - \overline{Q_{err}} \quad (9)$$

The PRIME-MCSP tendency as represented in equation 9 ensures the conservation of dry static energy within a column, even after incorporating stratiform latent heating into the model.

3 Simulations, Observations, and Storm Tracking Methodology

The PRIME-MCSP scheme has been implemented into version 13.0 of the Unified Model (UM13.0), developed by the United Kingdom Met Office. Its critical modules are described in Davies et al. (2005). Both the weather ensemble and climate simulations utilize UM13.0 over a global domain. The PRIME-MCSP scheme is evaluated by comparing against control runs where PRIME-MCSP is deactivated.

Table 1. Weather Simulations Spanning from July 1st, 2020, 03Z to July 3rd, 2020, 03Z.

Name of Experiment	PRIME-MCSP Scheme	α	Resolution	Ensemble Members
Control Run	N/A	N/A	~60 km	8
PRIME-MCSP Run	Activated	0.5	~60 km	8

The weather ensemble, as detailed in Table 1, is employed to evaluate the direct, short-term effects of PRIME-MCSP on storm lifecycles and their surrounding environments from a Lagrangian perspective. It has a horizontal grid spacing of approximately 60 km (N216) and 70 vertical levels. The model's integration time step is 7.5 minutes. The simulations are restarted from 8 initial-condition perturbed ensemble members of the Met Office Global and Regional Ensemble Prediction System–Global (Inverarity et al. 2023), on July 1st, 2020, at 0Z, and undergo a 3-hour spin-up. The analyzed simulations span a duration of 48 hours, starting from July 1st, 2020, at 3Z and ending on July 3rd, 2020, at 3Z. Two sets of simulations are produced: a set of control runs and a set of PRIME-MCSP runs, with the latter implementing a fixed α value of 0.5. Except for the CoMorph-A convection scheme, all other physical parameterizations in these weather ensemble members align with those used in the Met Office's operational weather forecasts, as described in Bush et al. (2022).

283 **Table 2.** Climate Simulations Spanning September 1988 to August 2008.

Name of Experiment	**PRIME-MCSP Scheme**	**α**	**Resolution**
Control Run	N/A	N/A	~135 km
PRIME-MCSP Run	Activated	0.5	~135 km
PRIME-MCSP Variable α Run	Activated	Variable α	~135 km

284 The climate simulations, as detailed in Table 2, aim to assess the long-term effects of
285 PRIME-MCSP on the large-scale precipitation patterns and MJO. This evaluation is based on
286 three model runs, each spanning 20 years from September 1988 to August 2008. The simulations
287 employ a horizontal grid spacing of approximately 135 km (N96) and have 85 vertical levels.
288 The model's integration time step is 20 minutes. The set includes a control run where the
289 PRIME-MCSP scheme is deactivated, a standard PRIME-MCSP run with a fixed α value of 0.5,
290 and a PRIME-MCSP Variable α run. In the Variable α run, the stratiform-to-convective heating
291 fraction is dynamically adjusted based on the cloud top temperature, as described above. Except
292 for the adoption of the CoMorph-A convection scheme, the model setup adheres to the Met
293 Office Atmospheric Model Intercomparison Project Phase 6 (AMIP6) configuration, with the
294 atmospheric model being forced by climatological boundary conditions (Walters et al. 2019).

295 The reference dataset utilized for the global assessment comprises several key sources:
296 the Global Precipitation Climatology Project (GPCP; Pendergrass et al. (2022), is employed to
297 assess the accuracy of simulated monthly precipitation. Furthermore, we use 26 models from the
298 Coupled Model Intercomparison Project Phase 6 (CMIP6; Eyring et al. 2016a) to analyze the
299 seasonal cycle of precipitation. These 26 models were selected following the research of Lauer et
300 al. (2023) to include only the atmospheric components of the CMIP6 models and prescribed
301 observed SSTs. This selection, known as AMIP6, represents the state-of-the-art capability for
302 predicting the atmospheric climate state. The National Centers for Environmental Prediction
303 (NCEP) Reanalysis data (Kalnay et al. 1996) serves to evaluate the MJO. The observed global
304 MCS tracks, as identified by Feng et al. (2021), are applied to assess the frequency of PRIME-
305 MCSP scheme being called.

306 Customized MCS tracking in this project utilizes the PyFLEXTRKR software, as detailed
307 by Feng et al. (2023), employing hourly maps of Top-Of-Atmosphere (TOA) infrared brightness
308 temperatures (IR T_b) alongside the surface rain rates. The conversion of simulated TOA
309 Outgoing Longwave Radiation (OLR) to IR T_b is achieved through the empirical correlation
310 established by Yang and Slingo (2001), enabling MCS identification as depicted in Figure 3a.
311 The MCS cold cloud shield mask is defined as its IR T_b falling below 241 K. This mask is
312 subsequently used to estimate the rainfall area and the mean rain rate underneath the MCS. The
313 criteria for selecting representative MCSs are a minimum cold cloud shield size of 60,000 km^2 at
314 the peak of its lifecycle, coupled with a duration exceeding 6 hours. Tracking an MCS requires a
315 minimum 50% overlap in its cold cloud shields for two consecutive model output time steps of
316 half an hour. Additional tracking configurations are elaborated in Feng et al. (2023).

317 MCS track matching between the MCS masks in the control (Figure 3a, black contours)
318 and the PRIME-MCSP (Figure 3b, black contours) runs is performed by requiring an areal
319 overlap ratio above 80% at the MCS initiation time. The magenta dots and lines in Figure 3a
320 illustrate the centroids and the path of the MCS at later times within the control run. The MCS

cloud region is delineated by the cold cloud shield mask, and the surrounding area of interest is defined as a region within a 600 km radius around the centroid (marked by the black circle in Figure 3a), excluding the areas under the cold cloud shield mask. The MCS cloud region and its surrounding area in the control run serve as the spatial basis ranges for computing the difference between fields in the control run and the PRIME-MCSP run. These differences are used to evaluate the effect of the PRIME-MCSP scheme throughout the MCS lifecycle.

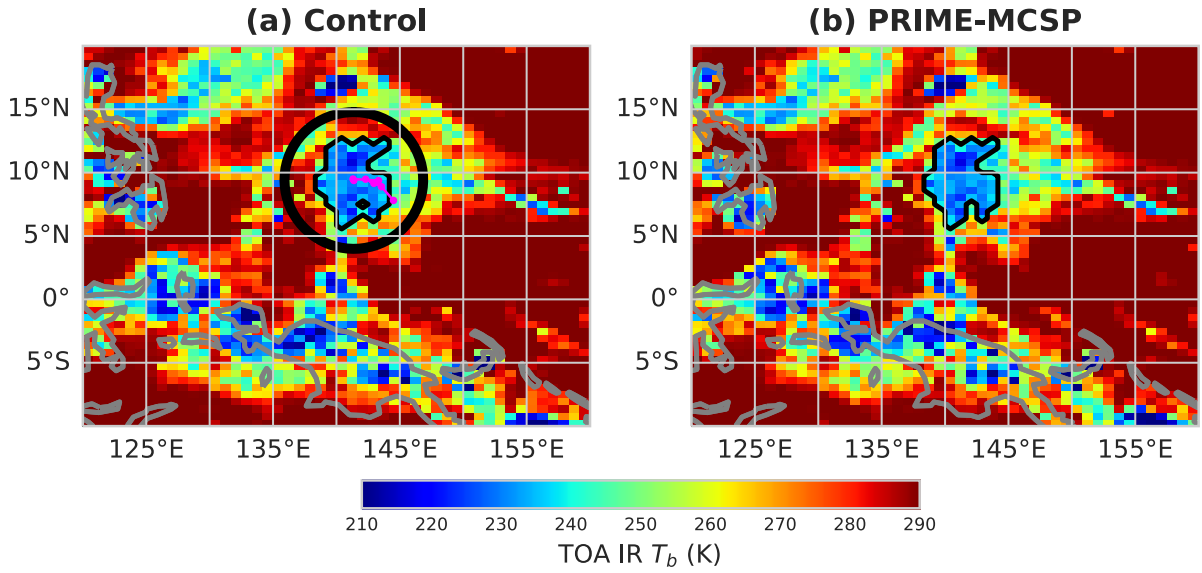

Figure 3. MCS track on July 1st, 2020, at 04:00 UTC. (a) The control run. The magenta dots and lines trace the MCS centroids and trajectory, respectively; the circle delineates the MCS surrounding environmental area of interest. (b) The PRIME-MCSP model run. The MCS boundaries in (a) and (b) are delineated by black contours. The grey contours delineate the coastlines over the Maritime Continent.

4 Direct Effects of the Scheme in Weather Ensembles

Figure 4a shows the count of global MCS tracks in both control and PRIME-MCSP ensemble runs across ensemble members 1 to 8, represented by blue and green bars, respectively. The PRIME-MCSP runs show a general concurrence with the control, albeit with a slight reduction in MCS track numbers. Approximately one-third to one-half of MCS tracks (indicated by red bars in Figure 4a) are matchable between control and PRIME-MCSP runs, totaling 163 MCS tracks across 8 ensemble members. The detailed MCS track matching method has been described in Section 3.

Figure 4b shows the frequency of PRIME-MCSP scheme activations throughout the normalized MCS lifecycle. The lifecycle of the MCS is normalized into 10 timesteps, ranging from 0 (initiation) to 9 (termination). The characteristics of the MCS are linearly interpolated across these 10 normalized timesteps to facilitate the combination of lifecycle evolutions. The calling frequency is defined as the ratio between grid points activating the PRIME-MCSP scheme and the grid points within the MCS mask area. Data from all MCS tracks in ensemble members is aggregated in Figure 4b. The median MCSP frequency exhibits a relatively stable evolution throughout the lifecycle with variations from 18% to 24% of the MCS area. This is in

agreement with the prior MCSP approach (e.g., Moncrieff & Liu, 2006), wherein the scheme is called in the convecting regions of the MCS, not the anvil. In addition to the combined statistics, Figure 4c shows a histogram of autocorrelation at a one-time-step lag, based on the calling frequency within each individual MCS lifecycle. The correlation coefficient is concentrated around 0.7, indicating the consistency of the calling frequency throughout each MCS lifecycle. This lifecycle continuity of calling frequency suggests effective coupling of the PRIME-MCSP scheme with the CoMorph-A convection scheme, avoiding abrupt activations or deactivations.

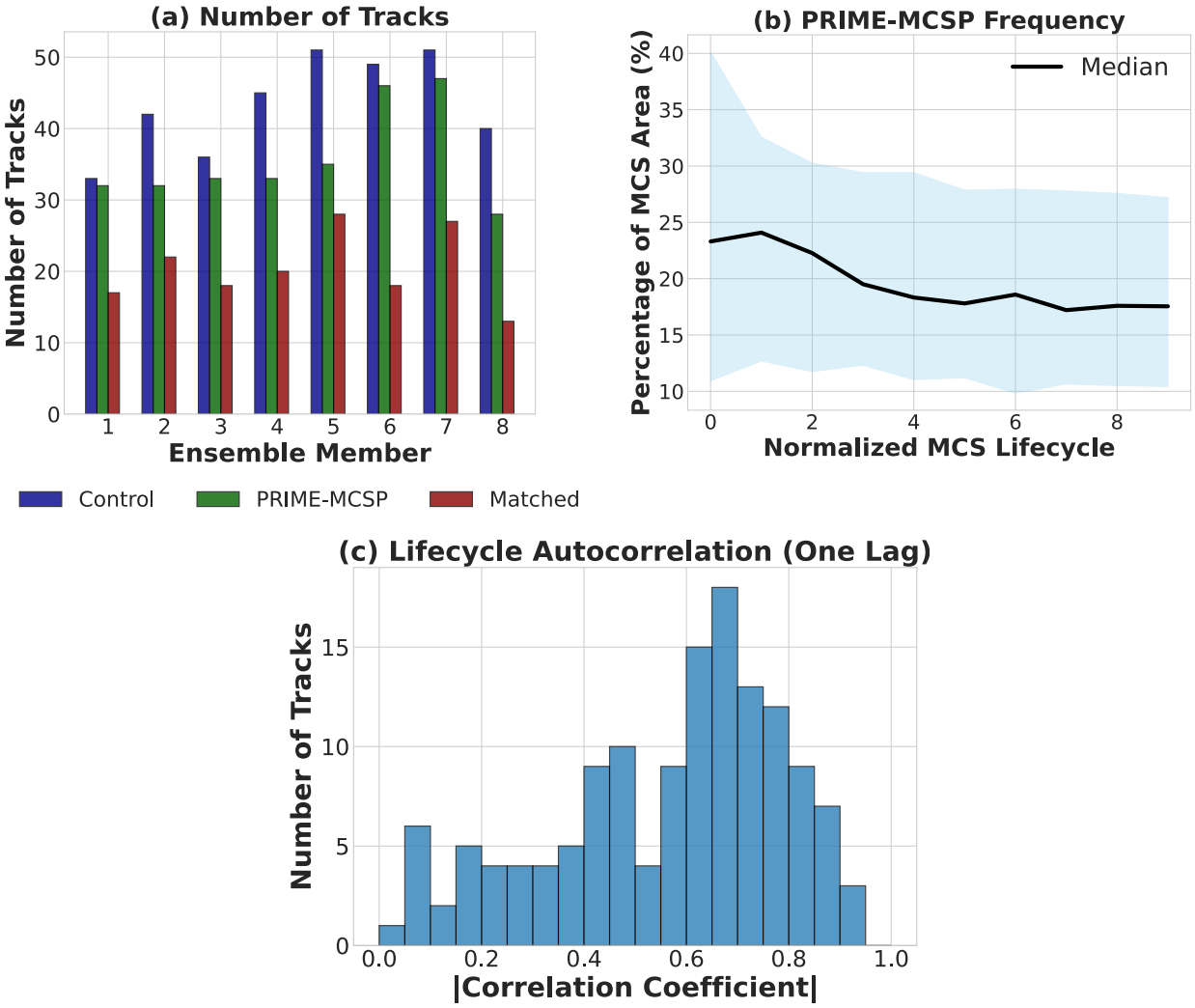

Figure 4. (a) MCS track counts, (b) invocation frequencies of the scheme across the MCS lifecycles. The shaded areas represent the Interquartile Range (IQR) in all matched tracks from all ensemble members, spanning the 25th to 75th percentiles, while the median value is depicted by the solid black line, and (c) histogram of the absolute values of MCS lifecycle autocorrelation with a one-time-step lag.

The PRIME-MCSP scheme primarily functions to transfer heat from the lower to the upper troposphere. We examine the evolution of spatially averaged temperature throughout the normalized lifecycles of the MCSs in both the cloud areas and surrounding environments. The normalized lifecycles, cloud areas, and MCS surrounding environments are based on the MCS

tracks in the control run that have corresponding matches in the PRIME-MCSP runs. It appears that the temperature does not change much throughout the lifecycle. Therefore, our analysis focuses on the temperature differences between the PRIME-MCSP run and the control run. In Figure 5 a–b, we observe a decrease in temperature for both the MCS cloud and the surrounding environment at 850 hPa as time progresses, with the rate of change in the MCS cloud being more pronounced. This indicates that the PRIME-MCSP scheme effectively induces cooling in the lower troposphere, as intended, and that over time, this cooling effect extends to the MCS's surrounding environment. Conversely, Figure 5 c–d shows an increase in temperature at 200 hPa for both the MCS cloud and the environment, again with a faster rate of change within the cloud. This demonstrates the scheme's role in upper tropospheric warming, with the additional heating in the cloud area gradually affecting the surrounding MCS environment over time.

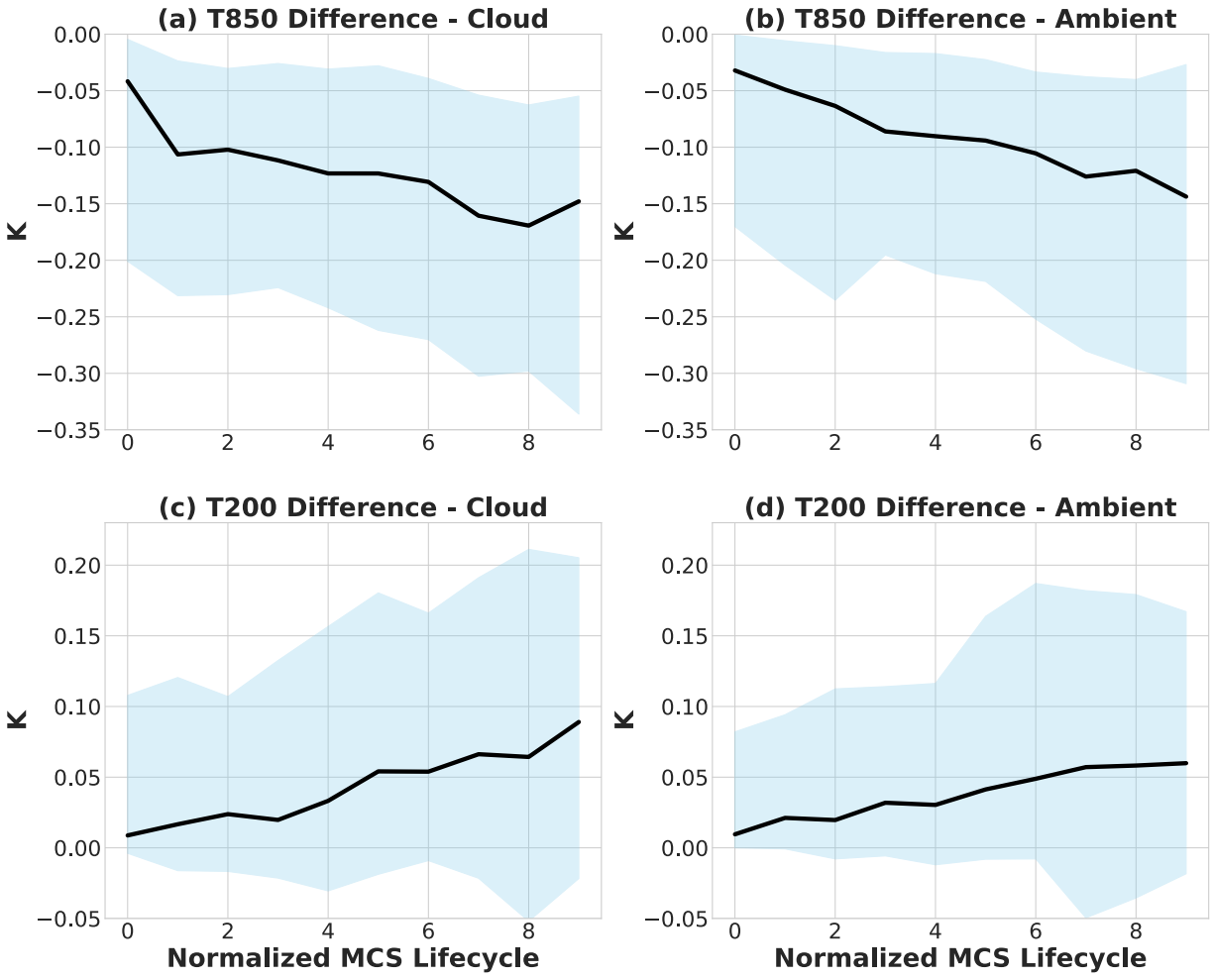

Figure 5. Temperature differences between the PRIME-MCSP and the control runs within MCS clouds and their surrounding environments at both 850 hPa (a–b) and 200 hPa (c–d) throughout the normalized MCS lifecycle, using the MCS tracks in the control run that have matches in the PRIME-MCSP runs. Shaded areas and lines follow the conventions from Figure 4b. Simulations span July 1st, 2020, 03Z to July 3rd, 2020, 03Z.

Figure 6 shows the response of 850 hPa vertical velocity to the lower tropospheric cooling induced by the PRIME-MCSP scheme. Within the MCS, a predominant positive vertical velocity is associated with ongoing convective updrafts throughout the lifecycle (Figure 6a). Conversely, in the surrounding environments of the MCS, a negative vertical velocity is also persistent, indicating the presence of environmental subsidence air (Figure 6c). When the PRIME-MCSP scheme is active, there is a weakening of convective updrafts (Figure 6b) and a corresponding weakening of the surrounding air subsidence (Figure 6d). These alterations highlight the PRIME-MCSP scheme's effect in moderating the explicit mesoscale circulations associated with the MCS. Additionally, an examination of the 200 hPa vertical velocity response (supplemental Figure S1) reveals no significant change, suggesting that the effects of the PRIME-MCSP upper tropospheric heating are nuanced, likely influenced by cloud top height and interactions with gravity waves.

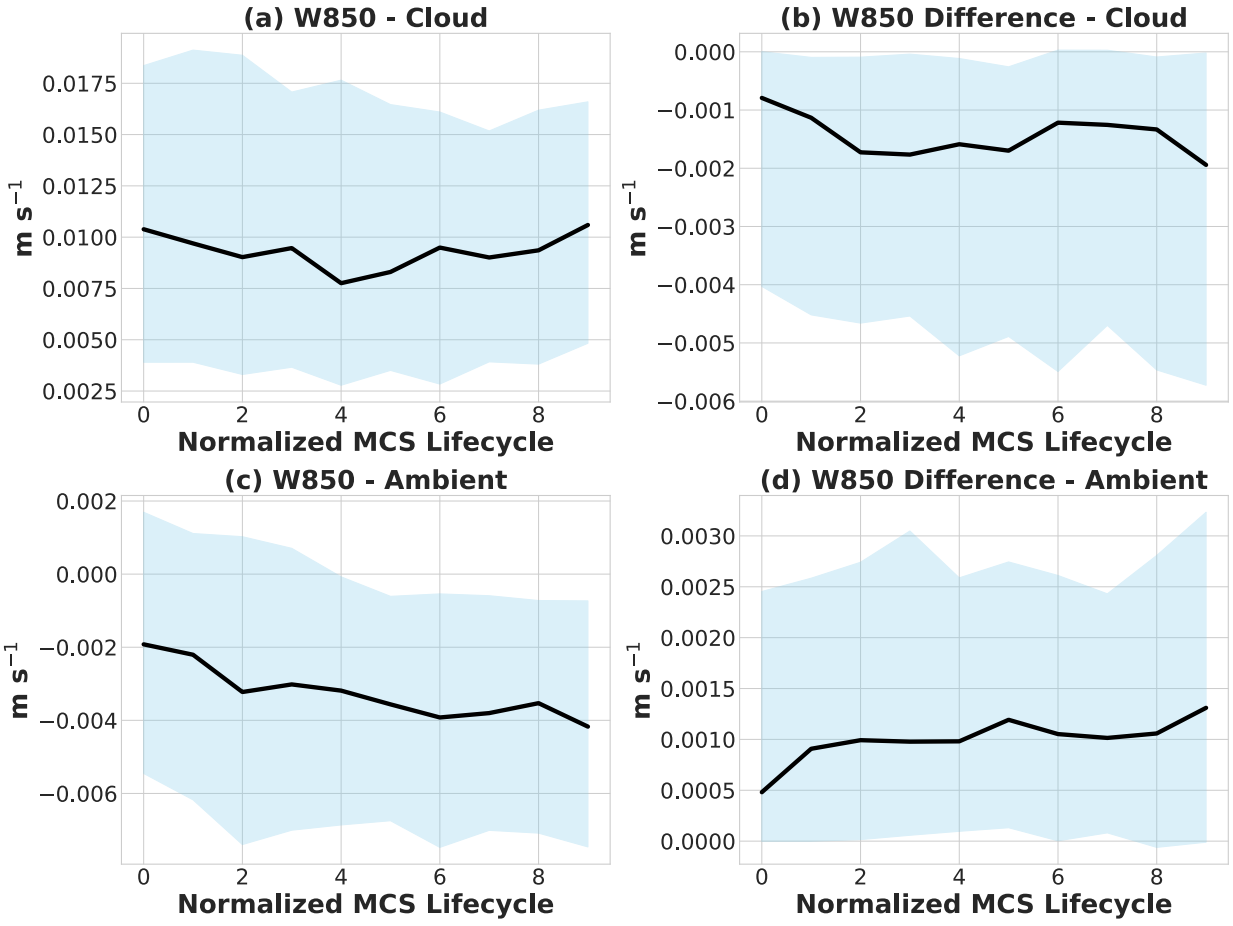

Figure 6. (a, c) 850 hPa vertical velocity in the control runs and (b, d) their changes following PRIME-MCSP activation, where a positive velocity indicates upward motion. Shaded areas and line conventions are as described in Figure 4b. Simulations span July 1st, 2020, 03Z to July 3rd, 2020, 03Z.

The impact of the PRIME-MCSP scheme on regional circulation is further demonstrated in Figure 7, which presents a global map highlighting the differences in 850 hPa vertical velocity between the MCSP run ensemble mean and the control run ensemble mean. Notably, over the

part of Intertropical Convergence Zone (ITCZ) between 10°–180°W, 0°–20°N and over various extratropical low-level jet regions, the formation of three parallel bands—central blue shading flanked by two red shading bands—mirrors the findings from Figure 6, indicating suppressed regional upward motion and reduced surrounding subsidence following the PRIME-MCSP scheme activation.

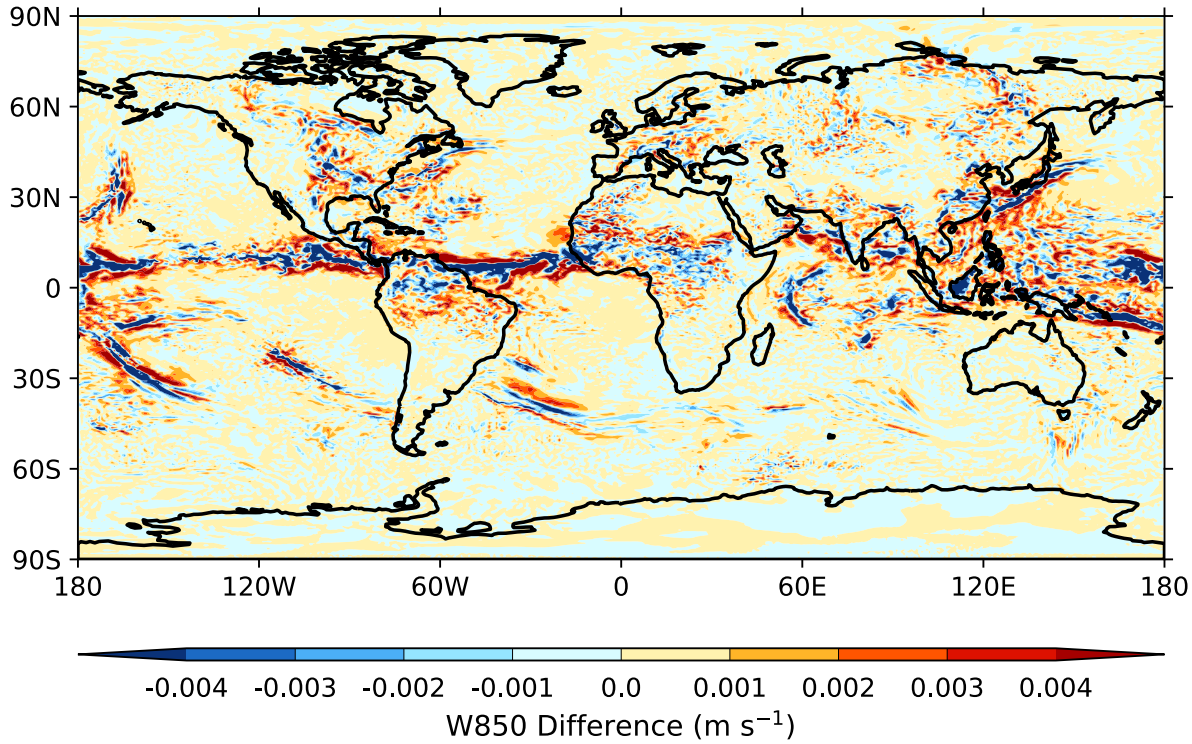

Figure 7. Ensemble mean difference in 850 hPa vertical velocity between the PRIME-MCSP and control runs, with black contours delineating coastlines. The averaging period is based on the entire 48 hours of the analyzed simulations.

The weakened circulations are linked to changes in MCS characteristics, including convective depth, rainfall area, and rain rate. Convective depth is represented by the minimum TOA IR T_b within the MCS's cold cloud shield, where colder TOA IR T_b values signify deeper MCS convective systems (Figure 8a). The PRIME-MCSP scheme results in a consistently positive TOA IR Tb difference throughout the MCS lifecycle (Figure 8b), suggesting a reduction in convective depth. The area covered by rainfall expands as the MCS matures, stabilizing in the latter part of the lifecycle (Figure 8c). The difference in rainfall area is consistently negative (Figure 8d), indicating the PRIME-MCSP scheme's tendency to reduce the rainfall area beneath the MCS's cold cloud shield. This explains the decrease in MCS track numbers as shown in Figure 4a, since a reduced MCS area impacts the number of cases meeting the lifecycle-maximum area threshold. Consistent with previous research indicating a positive correlation between convective depth and MCS area (Zhang et al., 2021), the decrease in convective depth is associated here with reduction in area. The PRIME-MCSP scheme's impact on rain rate is minimal, likely because rain rate is more influenced by large-scale microphysics, and the scheme primarily modifies heating tendencies without directly affecting rain rate. Combining reduced

rainfall area with an unchanged rain rate suggests a decrease in rainfall volume within MCSs following PRIME-MCSP activation. Accumulating these differences over time, along with changes in large-scale circulations, the long-term indirect effect of PRIME-MCSP on rainfall is assessed in Section 5.

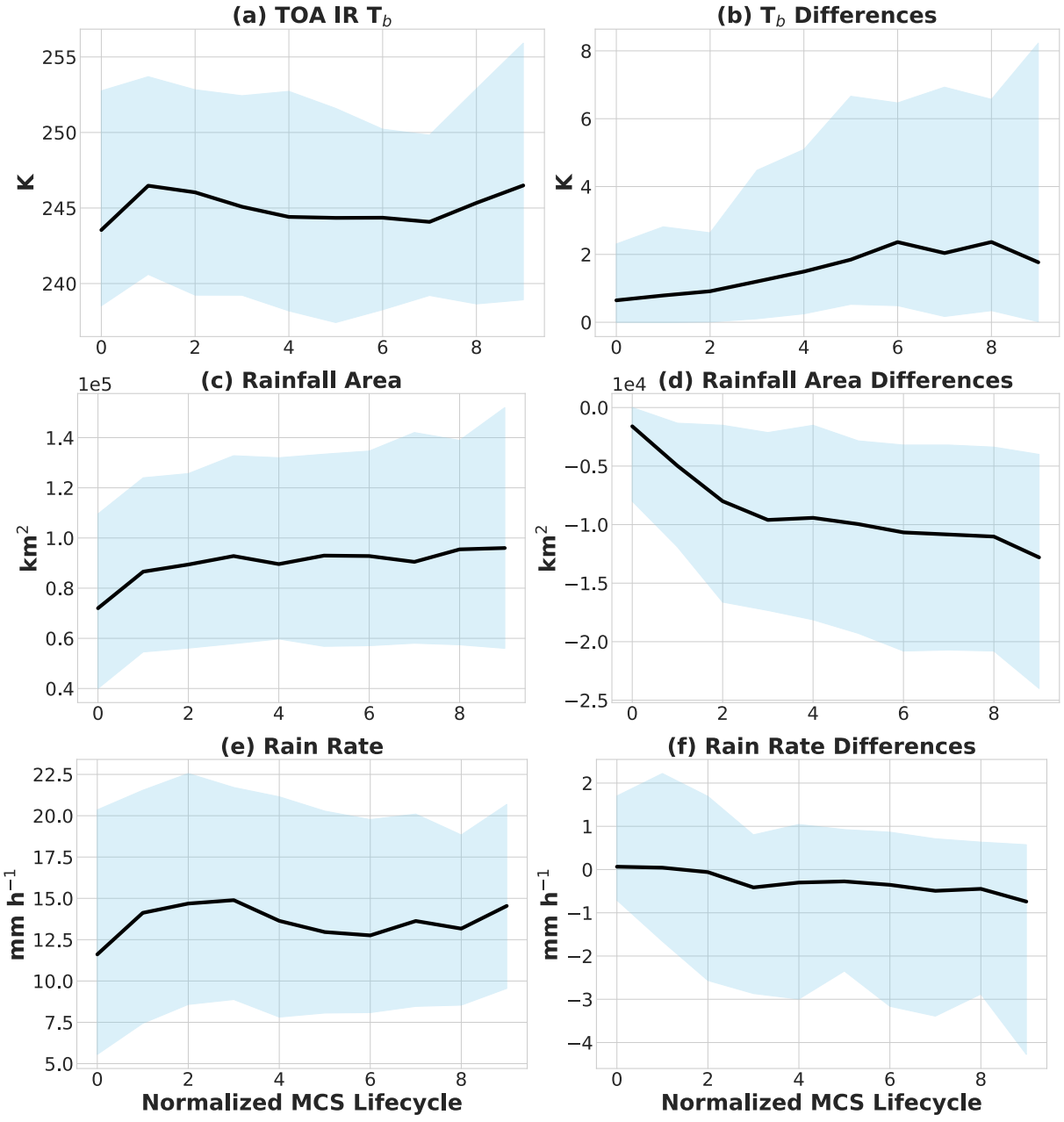

Figure 8. The lifecycles of (a) TOA IR T_b, (c) rainfall area, and (e) rain rate in the control run, and their changes (b, d, and f) following PRIME-MCSP activation. Simulations span July 1st, 2020, 03Z to July 3rd, 2020, 03Z.

5 Indirect Effects of the Scheme in Decadal Simulations

Before considering the indirect effects of the PRIME-MCSP scheme, we first compare the calling frequency of the scheme with real-world MCS occurrence frequencies. The comparison period spans from June 2000 to August 2008, coinciding with PRIME-MCSP runs and observed MCS track data from Feng et al. (2021). Figure 9a shows the MCS occurrence frequency using the observed global MCS track dataset, with color shading indicating the percentage of time the MCS cold cloud shield is present. Figure 9b illustrates the frequency of PRIME-MCSP scheme activation, defined by the percentage of timesteps on which the scheme is called. MCS frequencies generally exceed PRIME-MCSP activation frequencies (compare the color scales in Figures 9a and 9b). The relative spatial patterns show general agreement but with some regional discrepancies. PRIME-MCSP activation frequencies are relatively low over the Maritime Continent and slightly below those found in the ITCZ. Magenta rectangles in Figure 9 highlight areas where PRIME-MCSP frequencies strongly disagree with the MCS pattern, particularly over India and the Indian Ocean, with an expanded strong center further north over the Western Pacific.

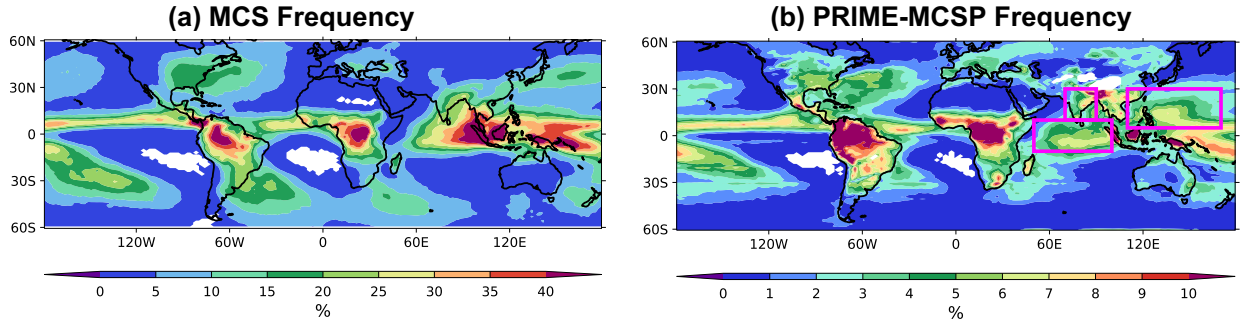

Figure 9. (a) Observed MCS occurrence frequency and (b) frequency of calling the PRIME-MCSP scheme in the decadal run. Magenta rectangles highlight regions of interest: India, the Indian Ocean, and the Western Pacific. The comparison period spans June 2000 to August 2008.

Figure 10 presents a comparison of the averaged global rain rate distributions as derived from satellite retrievals (GPCP), alongside those from the control, PRIME-MCSP, and PRIME-MCSP variable α runs over a 20-year period from September 1988 to August 2008. The Pearson correlation coefficients between the GPCP and these three simulations are 0.91, 0.91, and 0.92, respectively. These correlations indicate that the PRIME-MCSP scheme maintains the accuracy of global rainfall distribution.

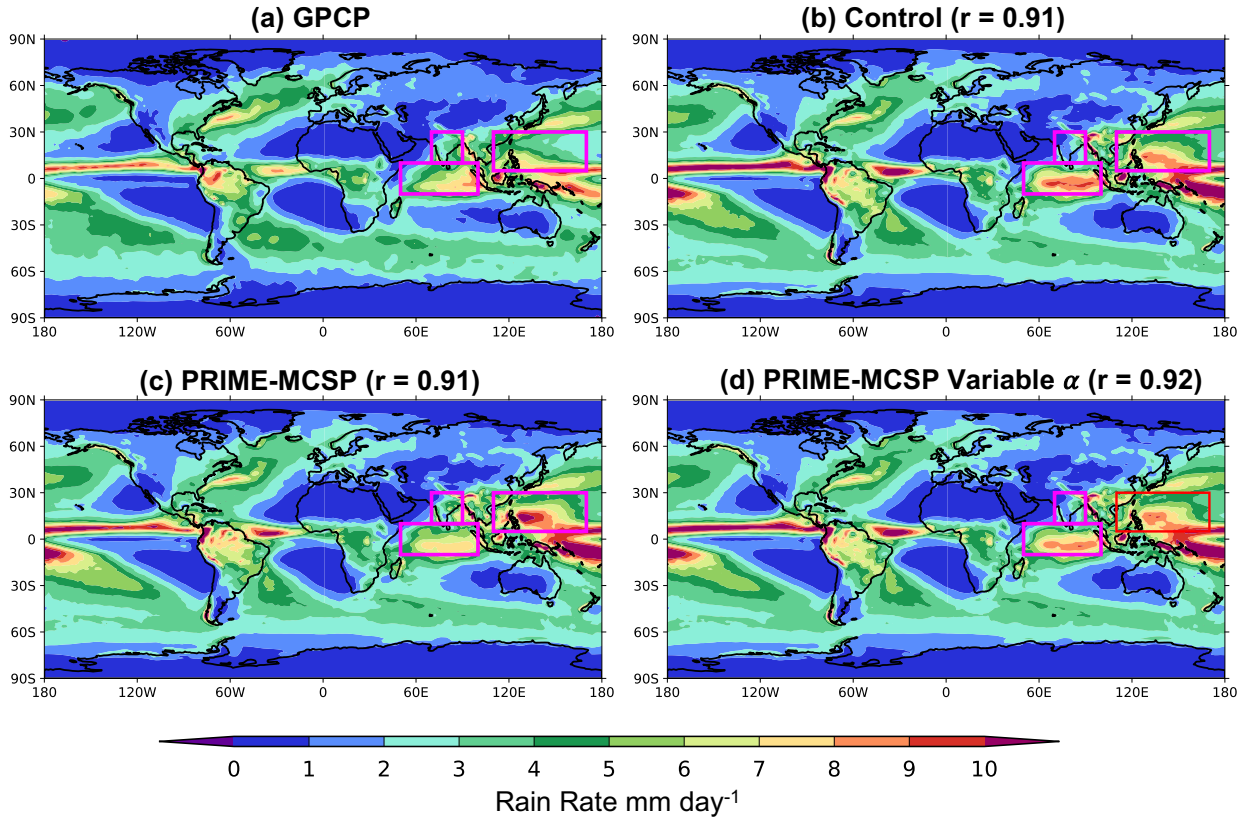

Figure 10. Average rain rate maps from (a) GPCP retrieval, (b) control, (c) PRIME-MCSP, and (d) PRIME-MCSP variable α runs. The Pearson correlation coefficient between the model runs and the GPCP retrieval is quoted for panels (b–d) as "r". All simulations and observations span September 1988 to August 2008.

Figure 11a presents the difference in rainfall between the control run and GPCP retrievals, with warm and cold colors indicating precipitation overestimation and underestimation, respectively. Predominantly, the control run overestimates rainfall across most tropical regions, especially within the ITCZ. Specifically, it overestimates rainfall over the Indian Ocean and Western Pacific, while underestimating it over India and the Bay of Bengal. These control run biases are consistent with Bush et al. (2014). Figure 11b demonstrates how PRIME-MCSP affects these biases, reducing the dry bias over India and mitigating the wet bias over the Indian Ocean, albeit amplifying it over the Western Pacific. The PRIME-MCSP variable α run generally mediates between the PRIME-MCSP and control runs, with a notable reduction in the wet bias over the Western Pacific compared to the PRIME-MCSP run, as indicated in supplemental Figure S2. However, improvements in rainfall accuracy over India and the Indian Ocean are more pronounced in the PRIME-MCSP run than in the PRIME-MCSP variable α run.

Figures 11c and 11d compare the absolute differences in rainfall biases (between the GPCP and model runs) before and after activating the PRIME-MCSP scheme, using a significance test based on 10,000 bootstrap resamples. Areas with significant changes (p values < 5%) in rainfall bias are marked with stipples, with cold and warm shadings indicating bias mitigation and amplification, respectively. The results suggest that improvements over India and the Indian Ocean are statistically significant. In contrast, the Western Pacific shows high internal

variability such that the apparent bias amplification in that region could be due to chance. The PRIME-MCSP variable α run shows a similar pattern to the PRIME-MCSP run but with a lesser magnitude of bias change and fewer significance stipples, indicating a balance between bias mitigation over the Indian Ocean and bias worsening over the Western Pacific, with a less significant improvement over the Indian Ocean compared to the PRIME-MCSP run.

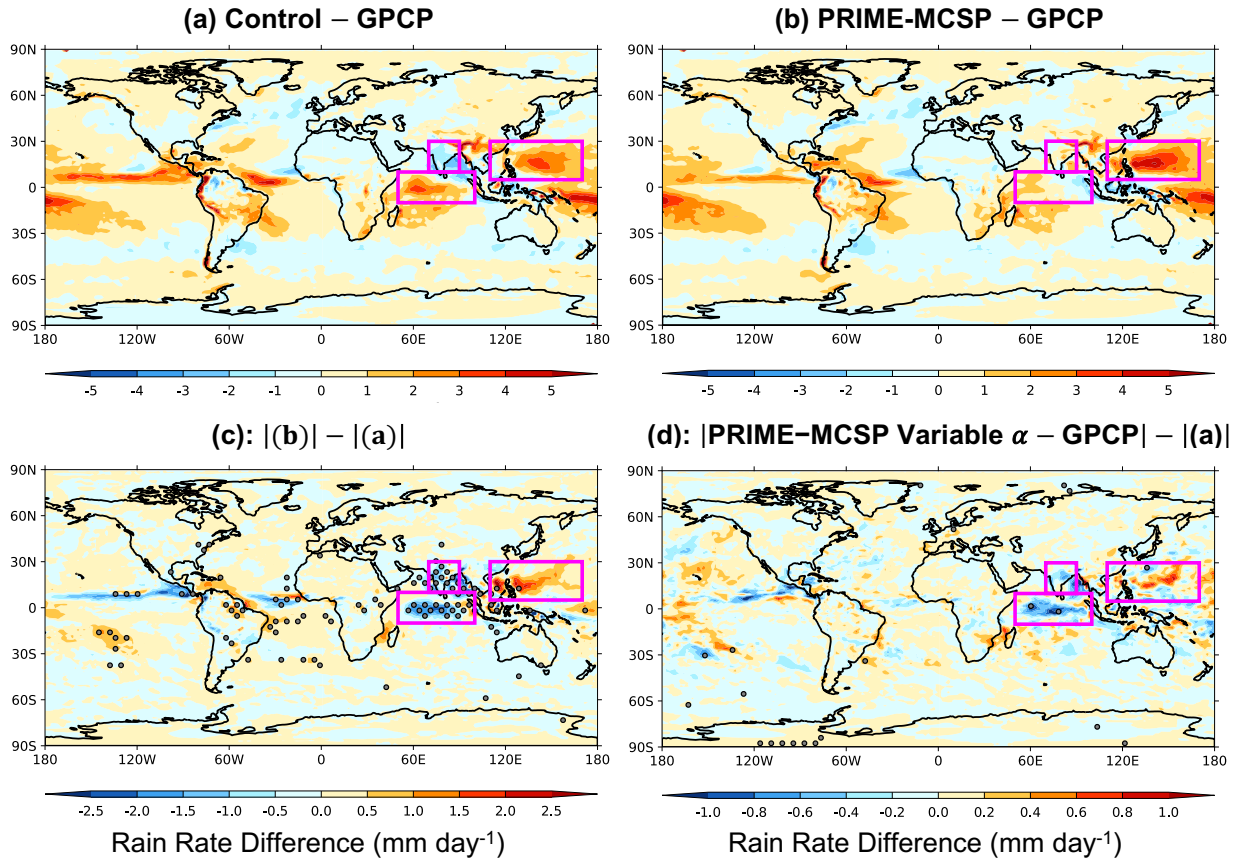

Figure 11. Rainfall difference between (a) the control run and GPCP, (b) the PRIME-MCSP run and GPCP, (c) the difference between the absolute values of (b) and (a), and (d) the same calculation as in (c) but for the PRIME-MCSP variable α run. The stippling in (c) and (d) indicates statistical significance, determined as described in the main text. Note the change of color scale between (c) and (d). All simulations and observations span September 1988 to August 2008.

In Figure 12, the annual cycles of precipitation seasonal cycles are used to diagnose further the rainfall changes over India and the Indian ocean in the PRIME-MCSP run and to compare with the control run and the CMIP6 ensemble simulations.

Over India, the control run significantly underestimates the rainfall, especially during the summer monsoon (Figure 12a). CMIP6 models agree better with the GPCP retrieval while overestimating the median precipitation from May to October (Figure 12b). The PRIME-MCSP run shows the closest agreement with the GPCP retrieval, outperforming both the control run and CMIP6 simulations, especially in correcting the underestimation of rainfall, as shown in Figure

12c. However, the IQRs in all these simulations are greater than those observed, highlighting the persistent model uncertainties across all models.

Over the Indian Ocean, the control run fails to capture the phase of the seasonal cycle and overestimates rainfall during all months (Figure 12d). CMIP6 performs better to agree with the observations in both timing and rainfall amounts from January to June, but significantly overestimates the precipitation from July to December (Figure 12e). The PRIME-MCSP run simulates both the phase and amplitude of the seasonal precipitation cycle, aligning closely with GPCP retrievals and markedly deviating from CMIP6 predictions (Figure 12f).

The PRIME-MCSP run suppassing CMIP6 predictions to agree with GPCP over the Indian ocean is particularly noteworthy given the run's coarser grid spacing relative to most CMIP6 simulations, suggesting the PRIME-MCSP scheme's upscaling effect plays a crucial role in capturing large-scale circulation patterns in this region. Consistently, the PRIME-MCSP variable α run also improves these seasonal cycles as for the PRIME-MCSP run, but with a muted amplitude alteration (shown in the supplemental Figure S3).

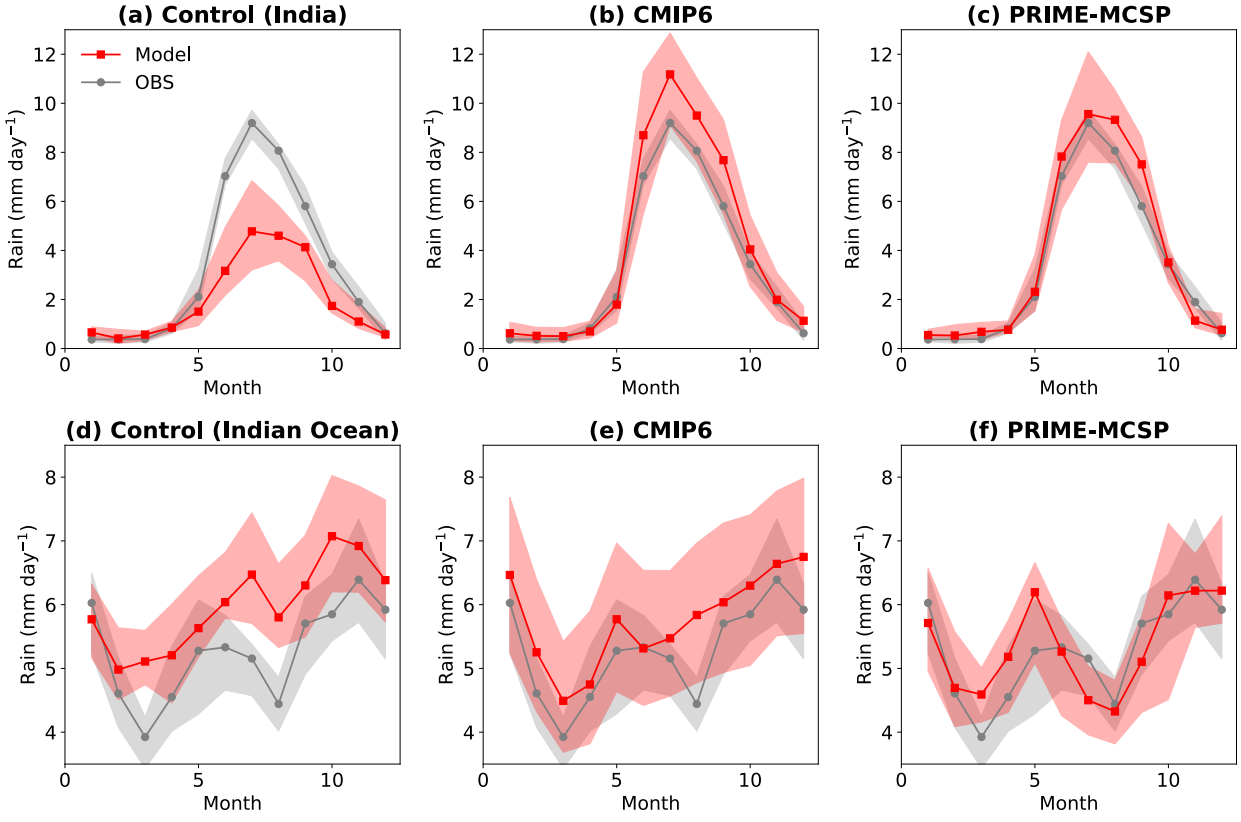

Figure 12. Simulated (red) and GPCP retrieved (grey) annual cycles of precipitation in the (a, d) control, (b, e) CMIP6, and (c, f) PRIME-MCSP run. The bands and lines indicate the IQR ranges and median values respectively. The India (a,b,c) and Indian ocean (d,e,f) regions are shown by the magenta boxes in Figure 10. All simulations and observations span September 1988 to August 2008.

The MJO plays a crucial role in influencing the annual precipitation cycle over India and the Indian Ocean, as proved in past studies (e.g., Hoell et al. 2018; Rushley et al. 2023). The

MJO's characteristics are analyzed for these climate runs in comparison with reanalysis, using the community software ESMValTool (Eyring et al. 2016b).

Figure 13 shows the symmetric wave cross spectra, derived from OLR and zonal wind data across the latitude range of 20°N to 20°S, following the methodology of Wheeler and Kiladis (1999). The spectral power density, depicted through color shading, highlights the presence of MJO signals. Specifically, Figure 13a identifies a peak at the MJO's characteristic period (20 to 100 days) and spatial scale (wavenumbers 1–2) with an orange color shading, indicating its typical spectral power density in reanalysis. The control run's spectra display a much weaker signal in this region. Conversely, both the PRIME-MCSP and the PRIME-MCSP variable α runs more successfully capture this spectral feature, indicating a more accurate representation of the MJO, with the PRIME-MCSP run exhibiting the closest match to reanalysis. Additionally, the Kelvin wave intensity is overestimated in the control run with the CoMorph-A convection scheme, but this overestimation is mitigated in the PRIME-MCSP run. This suggests that PRIME-MCSP might be promising in mitigating the pre-existing spectral bias inherited from the convection parameterization.

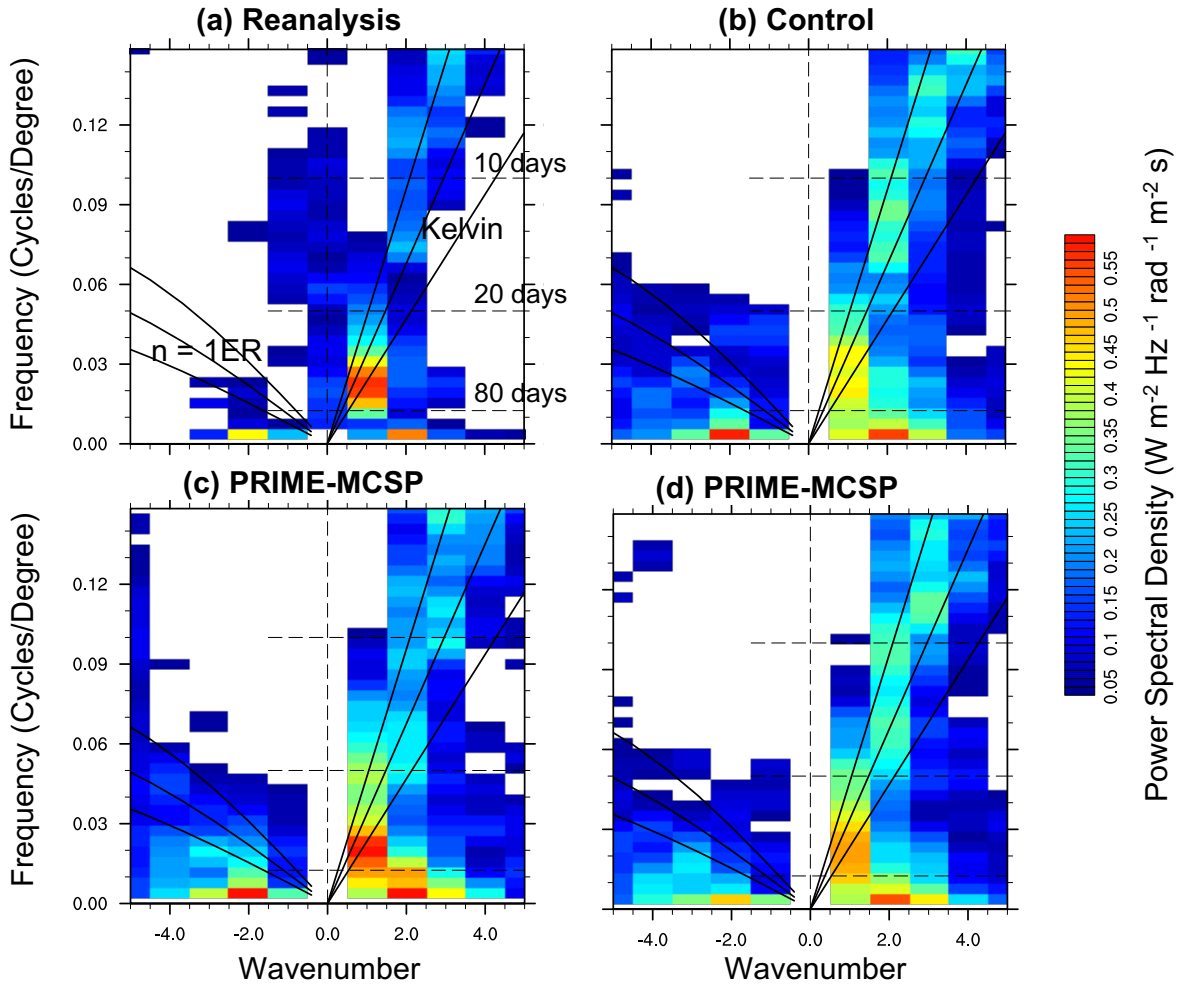

Figure 13. Symmetric wave cross spectra derived from OLR and zonal wind. The dashed lines, from top to bottom, indicate wave periods of 10, 20, and 80 days, respectively. The three black

lines on the left and right sides denote Equatorial Rossby (ER) waves and Kelvin waves, respectively. a) Reanalysis, b) Control simulation, c) PRIME-MCSP simulation, d) PRIME-MCSP variable α simulation. All simulations and observations span September 1988 to August 2008.

The MJO index is calculated following Wheeler and Hendon (2004) approach, which uses 15°S to 15°N averaged 850-hPa zonal wind, 200-hPa zonal wind, and OLR at the TOA. These daily fields in the reanalysis, control, PRIME-MCSP, and PRIME-MCSP variable α runs are filtered to leave the 20–100 days MJO components, before they are projected onto the same multiple-variable Empirical Orthogonal Functions computed from the reanalysis data. Two principal components are derived to depict the east-west and north-south progression of the MJO. The magnitude of the vector formed by these components serves as the MJO index, indicating the intensity of the MJO. When the MJO index exceeds a value of 1, these components are employed to categorize data into eight MJO phases, reflecting the spatial and temporal evolution of the MJO lifecycle.

Wintertime (November to April) MJO lifecycle composite maps are shown in Figure 14, again generated by ESMValTool. These maps use darker blue shading to indicate decreases in OLR, highlighting phases of enhanced rainfall and large-scale upward motion associated with the MJO. The sequence from Phase 1 (P1) to Phase 8 (P8) in Figure 14a illustrates the MJO's eastward propagation through its various phases in the reanalysis, with a consistent movement across the Maritime Continent. The control run (Figure 14b), however, shows discrepancies in capturing this propagation, particularly during Phase 6 (P6) when the anomaly dissipates too readily. The PRIME-MCSP and PRIME-MCSP variable α runs (Figure 14 c–d) both improve upon the control run's performance, with the former better at representing OLR anomalies before the MJO reaches the Maritime Continent and the latter being more accurate afterwards. Notably, the PRIME-MCSP variable α run depicts enhanced accuracy in P6, capturing the two strong centers of OLR anomalies over the Maritime Continent. This demonstrates the PRIME-MCSP scheme's effectiveness in improving MJO characteristics, aligning with findings from prior studies (e.g., Chen et al., 2021) and suggests sensitivity to variations of α in capturing spectral density and MJO lifecycles.

To quantify differences in wintertime MJO activity across the climate runs, histogram distributions of the MJO index are analyzed. A strong MJO event is defined as having an index greater than 1. According to this definition, the number of strong MJO events can vary between reanalysis and model runs. The control run exhibits too many weak MJO events (index less than one), as shown in Figure 15a. The PRIME-MCSP run reduces the occurrence of these weaker events (Figure 15b) while increasing the frequency of stronger events, indicating a mitigation of model biases in overestimating weak MJOs and underestimating strong MJOs. To assess the significance of Figure 15b, a Monte Carlo test was conducted, calculating the probability of changes in the 20-year total number of MJO occurrences between the control and the PRIME-MCSP run. This calculation was based on 100,000 resamplings using their respective annual counts of weak (index less than one) and strong (index greater than one) MJO occurrences. The significance test revealed that both the decrease in weak MJO occurrences and the increase in strong MJO occurrences are statistically significant, with p-values exceeding 94%. The comparison between the PRIME-MCSP run and reanalysis (Figure 15c) shows a closer alignment than that between the control run and reanalysis. The PRIME-MCSP variable α run

similarly improves the MJO index histogram distribution, aligning closely with reanalysis data (Figure 15d).

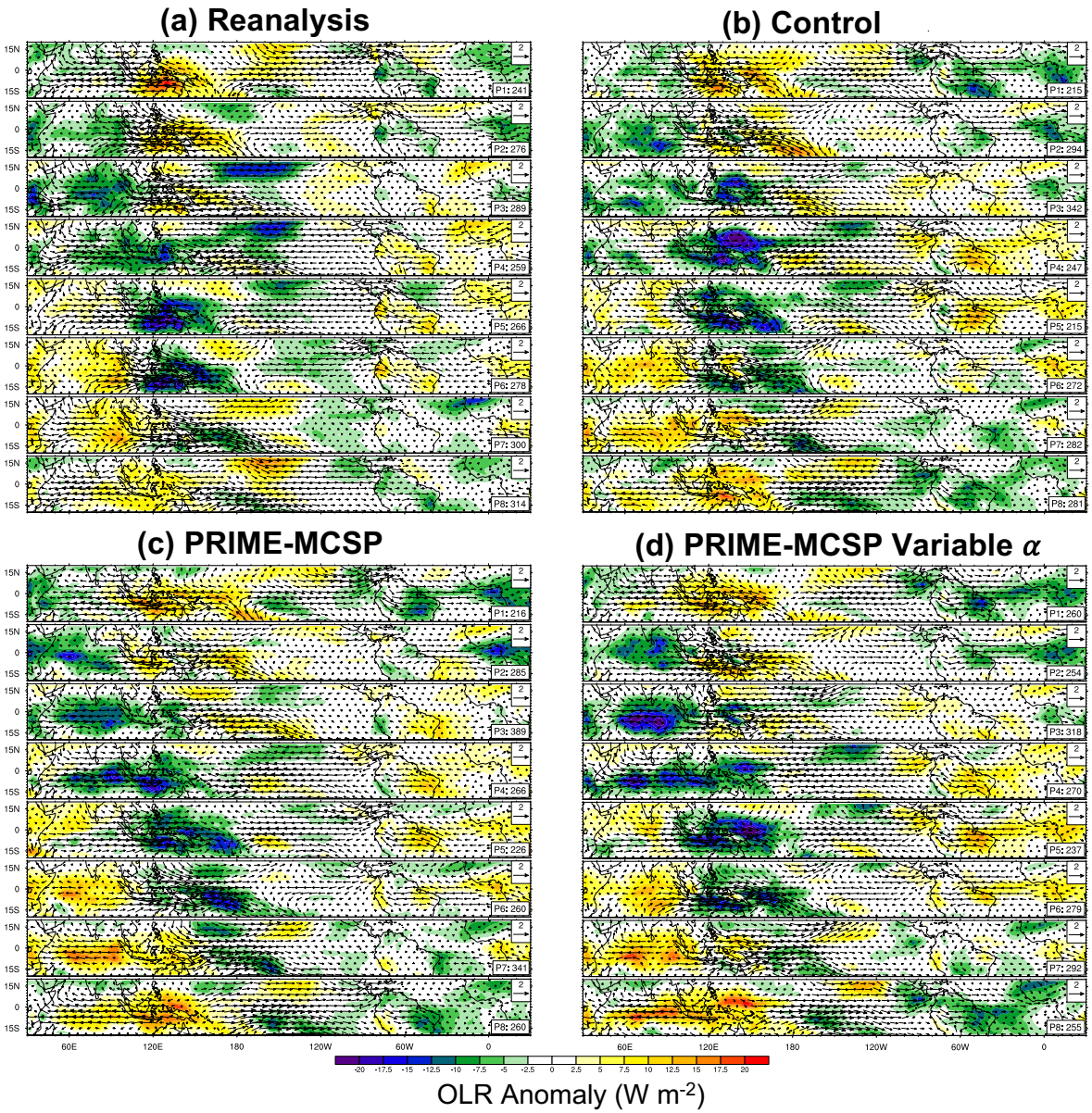

Figure 14. Wintertime (November–April) MJO lifecycle composites across different model runs: (a) Reanalysis, (b) Control, (c) PRIME-MCSP, and (d) PRIME-MCSP Variable α. The color shading indicates the OLR anomalies. Wind vectors represent the 850 hPa wind field. The subpanels, labeled P1 through P8, depict the sequential phases of the MJO lifecycle and the number of days identified as that phase, used to create the composite. All simulations and observations span September 1988 to August 2008.

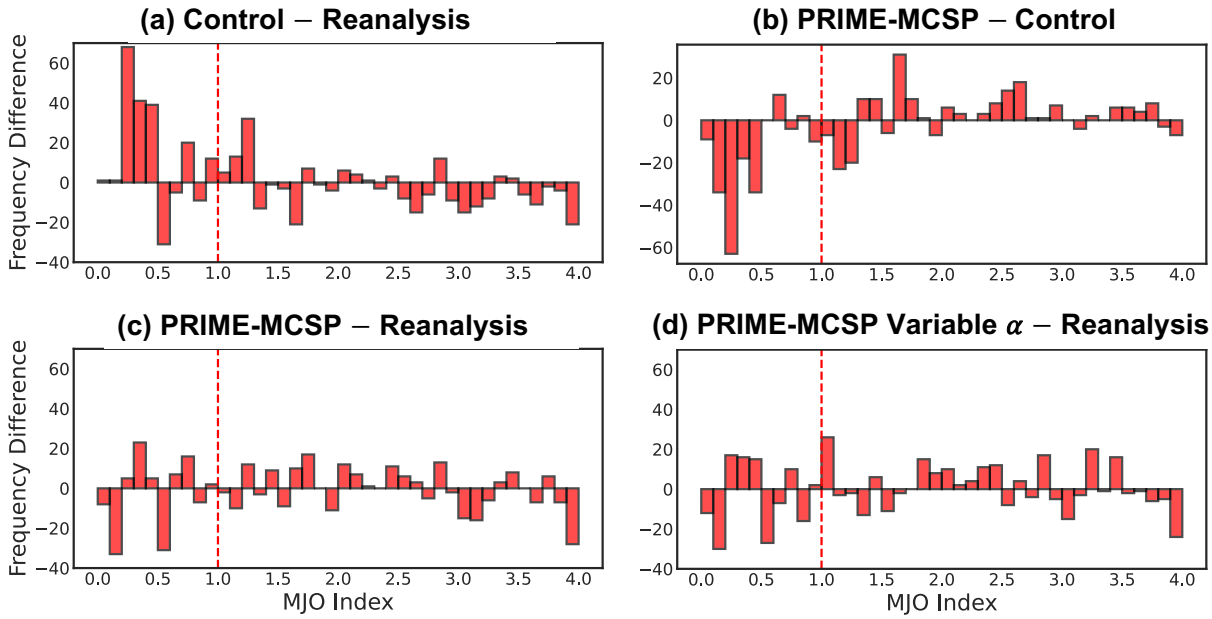

596

597 **Figure 15.** Comparative histogram distributions of wintertime (November–April) MJO index
598 differences. (a) between the control run and reanalysis, (b) PRIME-MCSP run versus control run,
599 (c) PRIME-MCSP run against reanalysis, and (d) PRIME-MCSP variable α against reanalysis.
600 The value in each bin represents the total number of MJOs that occur during the winter over the
601 20 years and fall within the index range.

602 **6 Conclusions**

603 This study implements the organized convection parameterization PRIME-MCSP in the
604 Unified Model in order to represent the stratiform heating associated with MCS. The scheme
605 incorporates several improvements over previous studies including:

606 1) Specialization of MCSP triggers: The PRIME-MCSP scheme features specialized
607 triggers for mixed-phase deep convection, incorporating ice condensate production into its
608 determination of whether the stratiform increment should be applied. This is achieved by only
609 triggering the scheme if the cloud top is above the freezing level. 2) Variable heating
610 partitioning: The study explores both a constant and a variable convective-to-stratiform heating
611 partitioning in the scheme, the latter being conditioned by cloud top temperature. 3) Leveraging
612 the mass-flux convection parameterization: The scheme's coupling with the Comorph-A scheme
613 is well suited to an MCS representation because CoMorph-A has a smooth numerical behavior in
614 time because of its allows convecting air parcels to ascend from any level, thereby promoting
615 continuity in the MCS evolution.

616 The scheme's evaluation is a comprehensive analysis of both its direct effects in weather
617 ensembles and its indirect effects in decadal simulations.

618 Direct effects: through an innovative use of MCS tracking, we showed that the scheme
619 acts to suppress MCS deepening and reduce MCS precipitation area. This is attributed to the
620 weakening of low-level mesoscale circulations associated with suppressed convective updrafts in
621 response to the stratiform lower-tropospheric cooling.

Indirect Effects: 20-year climate simulations assess the scheme's long-term impact, exhibiting a general agreement with global observed MCS frequencies, with regional variations over the tropical regions. Key results include 1) a reduction in precipitation bias across the Maritime time continent, effectively mitigating the dry bias over India and wet bias over the Indian Ocean; 2) The precipitation bias reduction is associated with a significant improvement in the representation of the precipitation seasonal cycle over the Indian and Indian Ocean, correcting a systematic bias observed across CMIP6 ensemble members; and 3) These precipitation improvements could be linked to the scheme's improvement on MJO spectra, aligning more closely with the reanalysis dataset by enhancing MJO intensity and continuing MJO eastward propagation during the post-Maritime Continent transit.

Despite these advances, the scheme's tendency to overestimate precipitation over the Western Pacific remains a challenge, echoing limitations in prior MCSP implementations (e.g., Moncrieff et al. 2019). Over the Western Pacific, Liu & Moncrieff (2017) found that MCS ascending airflows are often parallel to the environmental wind shear, in contrast with MCSP's slantwise layer overturning assumption. This suggests that the MCSP slantwise layer overturning paradigm might not apply to all MCSs. Additionally, the exploration of variable convective and stratiform partitioning proved to be a successful bias mitigation strategy over the Western Pacific but inadvertently reduced the improved precipitation representation over India and the Indian Ocean, indicating a spatially correlated bias pattern. Notably, Khouider et al. (2023) suggested that stochastic parameterization could potentially improve the representation of convective organization by refining the predicted mass flux of convective updrafts. This presents intriguing possibilities for future investigations into the stochastic parameterization of MCSP triggering and convective-to-stratiform partitioning probabilities, conditioned by various environmental patterns (Muetzelfeldt et al, 2024), which might reduce the Western Pacific's wet bias while maintaining the desirable improvements to seasonal precipitation predictability over India and the Indian Ocean.

Acknowledgments

This research is supported by the UK Research and Innovation (UKRI) Natural Environment Research Council (NERC) grant number NE/W005530/1 "Mesoscale Convective Systems: PRobabilistic forecasting and upscale IMpacts in the grey zonE (MCS: PRIME)". HMC was also funded by NERC grant number NE/P018238/1. Weather ensemble runs and decadal climate simulations were performed on the Monsoon2, a joint supercomputer system of the Met Office and NERC. Scheme assessments were carried out on the JASMIN UK high-performance computing clusters, funded by the Science and Technology Facilities Council on behalf of NERC. We extend our gratitude to Dr. Anne McCabe and Dr. Adrian Lock from the UK Met Office for their invaluable support in providing the necessary setup to conduct the Unified Model runs.

Open Research

Monthly global precipitation data are provided by the Global Precipitation Climatology Project (GPCP) at the National Center for Atmospheric Research (NCAR), available at https://climatedataguide.ucar.edu/climate-data/gpcp-monthly-global-precipitation-climatology-

project. CMIP6 simulated precipitation datasets are accessible via https://pcmdi.llnl.gov/CMIP6/. The observed global storm tracks dataset is available at https://doi.org/10.5281/zenodo.4244985. MCS tracks are generated using the PyFLEXTRKR software, available at https://github.com/FlexTRKR/PyFLEXTRKR. NCEP reanalysis data can be found at https://psl.noaa.gov/data/gridded/data.ncep.reanalysis.html. Please contact the authors directly for access to the PRIME-MCSP scheme and the model runs.

References

Barnes, H. C., M. D. Zuluaga, and R. A. Houze Jr. (2015), Latent heating characteristics of the MJO computed from TRMM observations, *J. Geophys. Res. Atmos.*, **120**, 1322–1334, doi:10.1002/2014JD022530

Becker, T., Bechtold, P., & Sandu, I. (2021). Characteristics of convective precipitation over tropical Africa in storm-resolving global simulations. *Quarterly Journal of the Royal Meteorological Society*, **147**(741), 4388–4407. https://doi.org/10.1002/qj.4185

Bush, S. J., Turner, A. G., Woolnough, S. J., Martin, G. M., & Klingaman, N. P. (2015). The effect of increased convective entrainment on Asian monsoon biases in the MetUM general circulation model. *Quarterly Journal of the Royal Meteorological Society*, **141**(686), 311–326. https://doi.org/10.1002/qj.2371

Bush, M., Boutle, I., Edwards, J., Finnenkoetter, A., Franklin, C., Hanley, K., et al. (2022). The second met office unified model/jules regional atmosphere and land configuration, RAL2. Geoscientific Model Development Discussions, 2022, 1–35. https://doi.org/10.5194/gmd-2022-209

Chen, C. C., Richter, J. H., Liu, C., Moncrieff, M. W., Tang, Q., Lin, W., et al. (2021). Effects of Organized Convection Parameterization on the MJO and Precipitation in E3SMv1. Part I: Mesoscale Heating. *Journal of Advances in Modeling Earth Systems*, ***13***(6). https://doi.org/10.1029/2020MS002401

Cheng, C. P., & Houze, R. A. (1979). The distribution of convective and mesoscale precipitation in GATE radar echo patterns. *Monthly Weather Review*, ***107***(10). https://doi.org/10.1175/1520-0493(1979)107<1370:TDOCAM>2.0.CO;2

Daleu, C. L., Plant, R. S., Stirling, A. J., & Whitall, M. (2023). Evaluating the CoMorph-A parametrization using idealized simulations of the two-way coupling between convection and large-scale dynamics. *Quarterly Journal of the Royal Meteorological Society,* **149**(757), 3087–3109. https://doi.org/10.1002/qj.4547

Davies, T., Cullen, M. J. P., Malcolm, A. J., Mawson, M. H., Staniforth, A., White, A. A., and Wood, N. (2005), A new dynamical core for the Met Office's global and regional modelling of the atmosphere, *Quarterly Journal of the Royal Meteorological Society*, **131**(608), 1759–1782

Eyring, V., Bony, S., Meehl, G. A., Senior, C. A., Stevens, B., Stouffer, R. J., and Taylor, K. E. (2016). Overview of the Coupled Model Intercomparison Project Phase 6 (CMIP6) experimental design and organization. *Geoscientific Model Development*, **9**, 1937–1958, https://doi.org/10.5194/gmd-9-1937-2016

Eyring, V., Righi, M., Lauer, A., Evaldsson, M., Wenzel, S., Jones, C., Anav, A., Andrews, O., Cionni, I., Davin, E. L., Deser, C., Ehbrecht, C., Friedlingstein, P., Gleckler, P., Gottschaldt, K.-D., Hagemann, S., Juckes, M., Kindermann, S., Krasting, J., Kunert, D., Levine, R., Loew, A., Mäkelä, J., Martin, G., Mason, E., Phillips, A. S., Read, S., Rio, C., Roehrig, R., Senftleben, D., Sterl, A., van Ulft, L. H., Walton, J., Wang, S., Williams, K. D. (2016). ESMValTool (v1.0)—A community diagnostic and performance metrics tool for routine evaluation of Earth system models in CMIP. *Geoscientific Model Development*, **9**(5), 1747–1802. https://doi.org/10.5194/gmd-9-1747-2016

Feng, Z., Leung, L. R., Liu, N., Wang, J., Houze, R. A., Li, J., et al. (2021). A global high-resolution mesoscale convective system database using satellite-derived cloud tops, surface precipitation, and tracking. *Journal of Geophysical Research: Atmospheres*, **126**(8). https://doi.org/10.1029/2020JD034202

Feng, Z., Hardin, J., Barnes, H. C., Li, J., Leung, L. R., Varble, A., & Zhang, Z. (2023). PyFLEXTRKR: A flexible feature tracking Python software for convective cloud analysis. *Geoscientific Model Development*, **16**, 2753–2776. https://doi.org/10.5194/gmd-16-2753-2023

Han, B., Fan, J., Varble, A., Morrison, H., Williams, C. R., Chen, B., et al. (2019). Cloud-Resolving model intercomparison of an MC3E squall line case: Part II. Stratiform precipitation properties. *Journal of Geophysical Research: Atmospheres*, **124**(2), 1090–1117. https://doi.org/10.1029/2018JD029596

Hartmann, D. L., H. H. Hendon, and R. A. Houze Jr. (1984), Some implications of the mesoscale circulations in tropical cloud clusters for large-scale dynamics and climate, J. Atmos. Sci., 41, 113–121. https://doi.org/10.1175/1520-0469(1984)041<0113:SIOTMC>2.0.CO;2

Hoell, A., Cannon, F., & Barlow, M. (2018). Middle East and Southwest Asia daily precipitation characteristics associated with the Madden–Julian Oscillation during Boreal Winter. *Journal of Climate*, **31**(21), 8843–8860. https://doi.org/10.1175/JCLI-D-18-0059.1

Houze, R. A., Smull, B. F., & Dodge, P. (1990). Mesoscale organization of springtime rainstorms in Oklahoma. *Monthly Weather Review*, ***118***(3). https://doi.org/10.1175/1520-0493(1990)118<0613:MOOSRI>2.0.CO;2

Houze, Robert A. (1989). Observed structure of mesoscale convective systems and implications for large-scale heating. *Quarterly Journal of the Royal Meteorological Society*, ***115***(487). https://doi.org/10.1002/qj.49711548702

Houze, R. A. (2004), Mesoscale convective systems, *Reviews of Geophysics*, **42**, RG4003, doi:10.1029/2004RG000150

Houze Jr, R. A. (2018). 100 years of research on mesoscale convective systems. *Meteorological Monographs*, 59, 17–1. https://doi.org/10.1175/AMSMONOGRAPHS-D-18-0001.1

Inverarity, G. W., Tennant, W. J., Anton, L., Bowler, N. E., Clayton, A. M., Jardak, M., Lorenc, A. C., Rawlins, F., Thompson, S. A., Thurlow, M. S., Walters, D. N., & Wlasak, M. A. (2023), Met Office MOGREPS-G initialisation using an ensemble of hybrid four-dimensional ensemble variational (En-4DEnVar) data assimilations, *Quarterly Journal of the Royal Meteorological Society*, **149**(753), 1138–1164, https://doi.org/10.1002/qj.4431

Kalnay, E., Kanamitsu, M., Kistler, R., Collins, W., Deaven, D., Gandin, L., et al. (1996). The NCEP/NCAR 40-year reanalysis project [Dataset]. *Bulletin of the American Meteorological Society*, **77**(3), 437–472. https://doi.org/10.1175/1520-0477(1996)077<0437:TNYRP>2.0.CO;2

Khouider, B., Goswami, B. B., Phani, R., & Majda, A. J. (2023). A shallow-deep unified stochastic mass flux cumulus parameterization in the single column Community Climate Model. *Journal of Advances in Modeling Earth Systems*, **15**, e2022MS003391. https://doi.org/10.1029/2022MS003391

Kooperman, G. J., Pritchard, M. S., & Somerville, R. C. J. (2014). The response of US summer rainfall to quadrupled CO2 climate change in conventional and superparameterized versions of the NCAR community atmosphere model. *Journal of Advances in Modeling Earth Systems*, **6**(3), 859–882. https://doi.org/10.1002/2014MS000306

Lauer, A., Bock, L., Hassler, B., Schröder, M., & Stengel, M. (2023). Cloud climatologies from global climate models—A comparison of CMIP5 and CMIP6 models with satellite data. *Journal of Climate*, **36**(2), 281–311. https://doi.org/10.1175/JCLI-D-22-0181.1

Lavender, S. L., Stirling, A. J., Whitall, M., Stratton, R., Daleu, C. L., Plant, R. S., Lock, A. & Gu, J.-F. (2024) The use of idealised experiments in testing a new convective parameterization: Performance of CoMorph-A. To appear in: *Quarterly Journal of the Royal Meteorological Society*. https://doi.org/10.1002/qj.4660

Leary, C. A., & Houze, R. A. (1979). Melting and evaporation of hydrometeors in precipitation from the anvil clouds of deep tropical convection. *Journal of the Atmospheric Sciences*, ***36***(4), 669–679. https://doi.org/10.1175/1520-0469(1979)036<0669:MAEOHI>2.0.CO;2

Liu, C. & Moncrieff, M. W. (2017) Shear-parallel mesoscale convective systems in a moist low-inhibition Mei-Yu front environment. *Journal of the Atmospheric Sciences*, **74**(12), 4213–4228. https://doi.org/10.1175/JAS-D-17-0121.1

Moncrieff, M. W. (2019). Toward a dynamical foundation for organized convection parameterization in GCMs. *Geophysical Research Letters*, **46**(14),103–14,108. https://doi.org/10.1029/2019GL085316

Moncrieff, M. W., & Liu, C. (2006). Representing convective organization in prediction models by a hybrid strategy. *Journal of the Atmospheric Sciences*, **63**(12). https://doi.org/10.1175/JAS3812.1

Moncrieff, M. W., Liu, C., & Bogenschutz, P. (2017). Simulation, modeling, and dynamically based parameterization of organized tropical convection for global climate models. *Journal of the Atmospheric Sciences*, **74**(5). https://doi.org/10.1175/JAS-D-16-0166.1

Muetzelfeldt, M. R., Plant, R. S., Christensen, H. M., Zhang, Z., Woollings, T., Feng, Z. & Li, P. (2024), Environmental Conditions Affecting Global Mesoscale Convective System Occurrence. Submitted to: *Journal of the Atmospheric Sciences*

Pendergrass, A. &, Wang, J. & National Center for Atmospheric Research Staff (Eds). Last modified 2022-11-07 "The Climate Data Guide: GPCP (Monthly): Global Precipitation Climatology Project." Retrieved from https://climatedataguide.ucar.edu/climate-data/gpcp-monthly-global-precipitation-climatology-project on 2024-03-13

Prein, A. F., Liu, C., Ikeda, K., Bullock, R., Rasmussen, R. M., Holland, G. J., & Clark, M. (2020). Simulating North American mesoscale convective systems with a convection-permitting climate model. *Climate Dynamics*, **55**(1), 95–110. https://doi.org/10.1007/s00382-017-3993-2

Rushley, S. S., Kang, D., Kim, D., An, S.-I., & Wang, T. (2023). MJO in different orbital regimes: Role of the mean state on the MJO's amplitude during boreal winter. *Journal of Climate*, **36**(13), 1–41. https://doi.org/10.1175/JCLI-D-22-0725.1

Schumacher, C., Houze, R. A., & Kraucunas, I. (2004). The Tropical Dynamical Response to Latent Heating Estimates Derived from the TRMM Precipitation Radar. *Journal of the Atmospheric Sciences*, **61**(12), 1341–1358. https://doi.org/10.1175/1520-0469(2004)061<1341:TTDRTL>2.0.CO;2

Schumacher, R. S., & Rasmussen, K. L. (2020). The formation, character and changing nature of mesoscale convective systems. *Nature Reviews Earth & Environment*, **1**, 300–314. https://doi.org/10.1038/s43017-020-0057-7

Varble, A., Zipser, E. J., Fridlind, A. M., Zhu, P., Ackerman, A. S., Chaboureau, J.-P., Collis, S., et al. (2014). Evaluation of cloud-resolving and limited area model intercomparison simulations using TWP-ICE observations: 1. Deep convective updraft properties. *Journal of Geophysical Research: Atmospheres*, **119**(24), 13,891–13,918. https://doi.org/10.1002/2013JD021371

Varble, A., Zipser, E. J., Fridlind, A. M., Zhu, P., Ackerman, A. S., Chaboureau, J.-P., et al. (2014b). Evaluation of cloud-resolving and limited area model intercomparison simulations using TWP-ICE observations: 2. Precipitation microphysics. *Journal of Geophysical Research: Atmospheres*, **119**(24), 13919–13945. https://doi.org/10.1002/2013JD021372

Walters, D., Baran, A. J., Boutle, I., Brooks, M., Earnshaw, P., Edwards, J., Furtado, K., Hill, P., Lock, A., Manners, J., & Morcrette, C. (2019). The Met Office Unified Model global atmosphere 7.0/7.1 and JULES global land 7.0 configurations. *Geoscientific Model Development*, **12**(5), 1909–1963.

Wheeler, M. C., & Hendon, H. H. (2004). An all-season real-time multivariate MJO index: Development of an index for monitoring and prediction. *Monthly Weather Review*, **132**(8), 1917–1932. https://doi.org/10.1175/1520-0493(2004)132<1917:AARMMI>2.0.CO;2

Wheeler, M., and G. N. Kiladis (1999), Convectively coupled equatorial waves: Analysis of clouds and temperature in the wavenumber-frequency domain, *Journal of the Atmospheric Sciences*, **56**, 374–399.

Whitall, M., Stirling, A., Lock, A., Lavender, S., Stratton, R. & Matsubayashi, K. (2022) The CoMorph convection scheme. UM Documentation Paper 043.

Yang, G.-Y., & Slingo, J. (2001). The diurnal cycle in the tropics. *Monthly Weather Review*, **129**(4), 784–801. https://doi.org/10.1175/1520-0493(2001)129<0784:TDCITT>2.0.CO;2

Zhang, G. J., & McFarlane, N. A. (1995). Sensitivity of climate simulations to the parameterization of cumulus convection in the Canadian climate centre general

827 circulation model. *Atmosphere - Ocean*, **33**(3).
828 https://doi.org/10.1080/07055900.1995.9649539

829 Zhang, Z., Varble, A., Feng, Z., Hardin, J., & Zipser, E. (2021). Growth of mesoscale convective
830 systems in observations and a seasonal convection-permitting simulation over Argentina.
831 *Monthly Weather Review*, **149**(10), 3469–3490. https://doi.org/10.1175/MWR-D-20-
832 0411.1

833 Zhang, Z., Varble, A., Feng, Z., Marquis, J., Hardin, J., & Zipser, E. (2024). Dependencies of
834 Simulated Convective Cell and System Growth Biases on Atmospheric Instability and
835 Model Resolution. Submitted to *Journal of Geophysical Research: Atmospheres*.

Journal of Advances in Modeling Earth Systems

Supporting Information for

Advancing Organized Convection Representation in the Unified Model: Implementing and Enhancing Multiscale Coherent Structure Parameterization

Zhixiao Zhang[1], Hannah M. Christensen[1], Mark R. Muetzelfeldt[2], Tim Woollings[1], Robert S. Plant[2], Alison J. Stirling[3], Michael A. Whitall[3], Mitchell W. Moncrieff[4], Chih-Chieh Chen[4], and Zhe Feng[5]

[1]Department of Physics, University of Oxford, Oxford, Oxfordshire, UK.

[2]Department of Meteorology, University of Reading, Reading, Berkshire, UK.

[3]Met Office, Exeter, Devon, UK.

[4]Climate and Global Dynamics Division, National Center for Atmospheric Research, Boulder, Colorado, USA.

[5]Atmospheric, Climate, and Earth Sciences Division, Pacific Northwest National Laboratory, Richland, Washington, USA.

Corresponding author: Zhixiao Zhang (zhixiao.zhang@physics.ox.ac.uk)

Contents of this file

Figures S1 to S4

Introduction

Figures S1–S4 are referenced in the manuscript and shown here. They are of secondary importance to Figures in the manuscript but provide useful context to results and conclusions in the study.

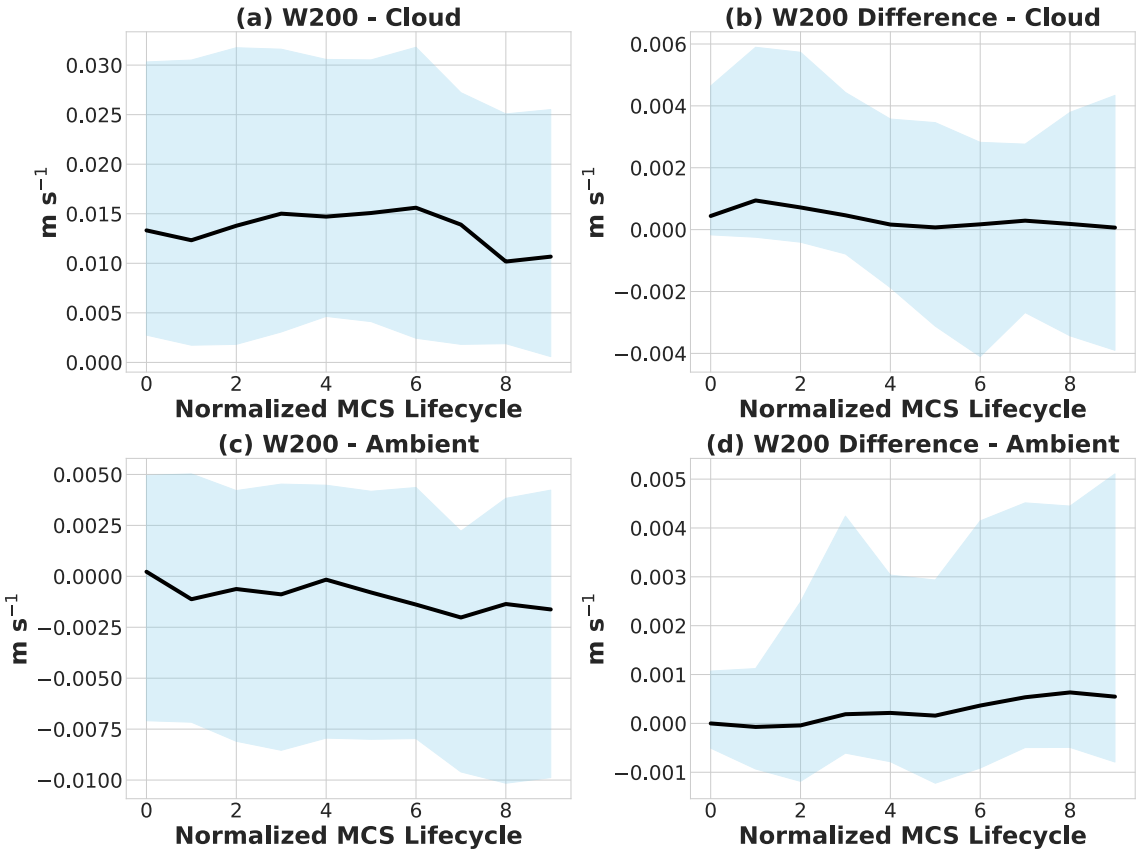

Figure S1. Similar to Figure 6 in the main paper. (a, c) 200 hPa vertical velocity in the control runs and (b, d) their changes following PRIME-MCSP activation, where a positive velocity indicates upward motion. Shaded areas and line conventions are as described in Figure 4b. Simulations span July 1st, 2020, 03Z to July 3rd, 2020, 03Z.

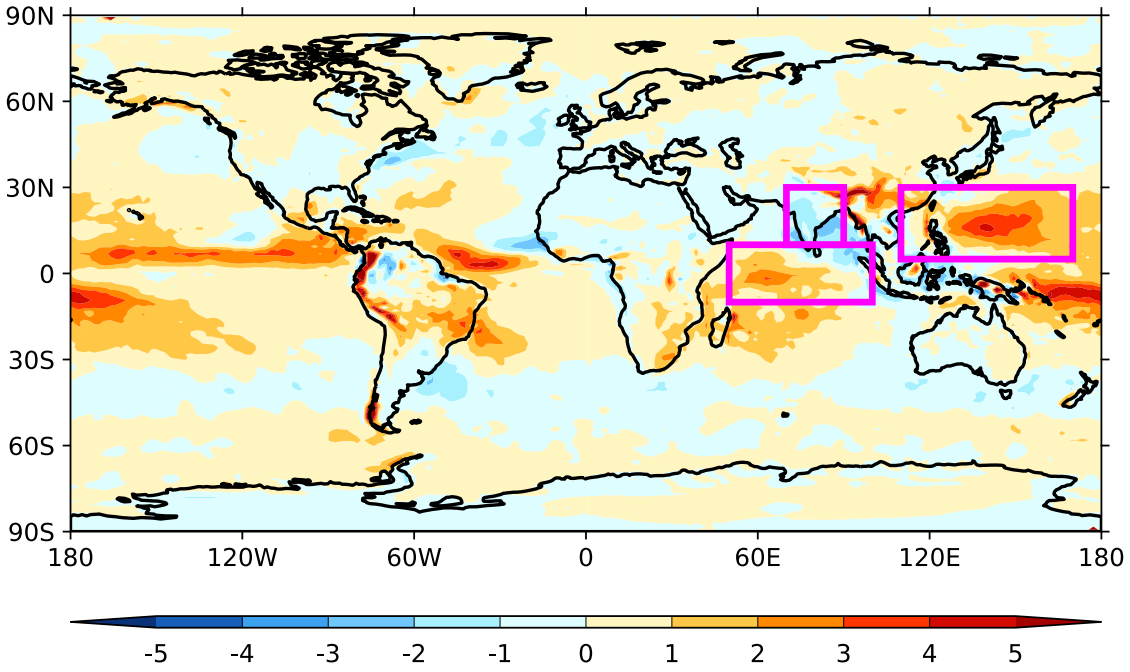

Figure S2. Rainfall difference between the PRIME-MCSP variable α run and GPCP. The simulations and observations span September 1988 to August 2008.

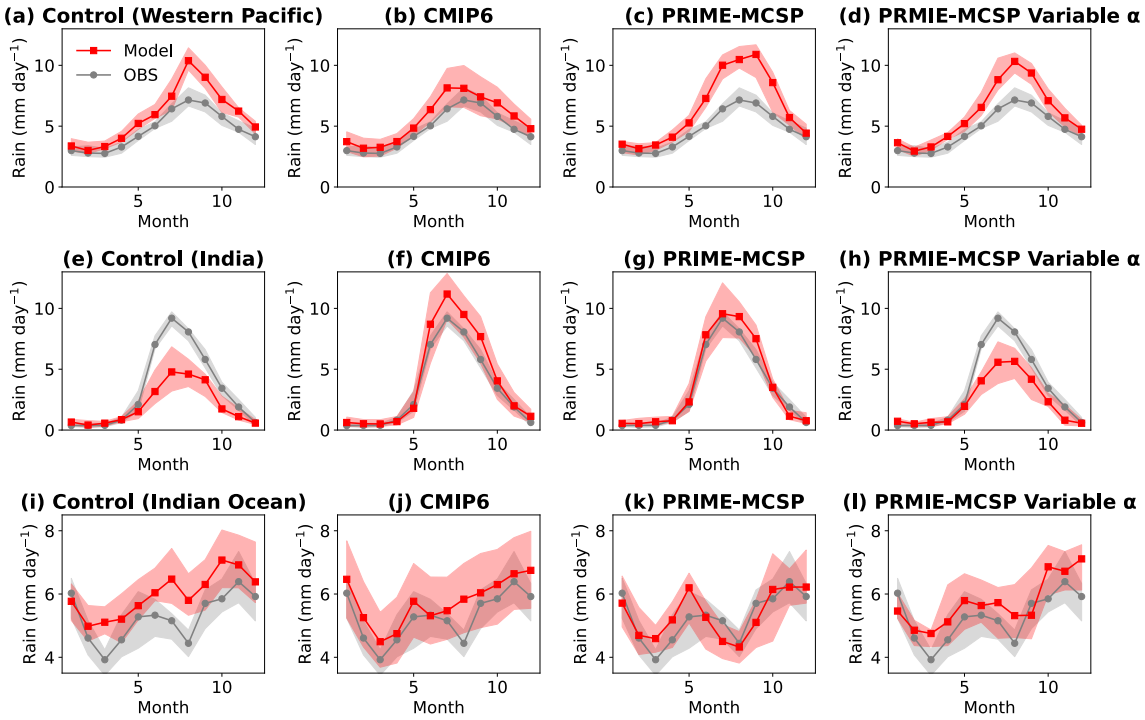

Figure S3. Similar to Figure 12 in the main paper. Simulated (red) and GPCP retrieved (grey) annual cycles of precipitation in the (a, e, i) control, (b, f, j) CMIP6, (c, g, k) PRIME-MCSP and (d, h, l) PRIME-MCSP variable α runs. The bands and lines indicate the IQR ranges and median values respectively. The Western Pacific (a–d), Indian (e–h) and Indian ocean (i–l) regions are shown by the magenta boxes in Figure 10. All simulations and observations span September 1988 to August 2008.

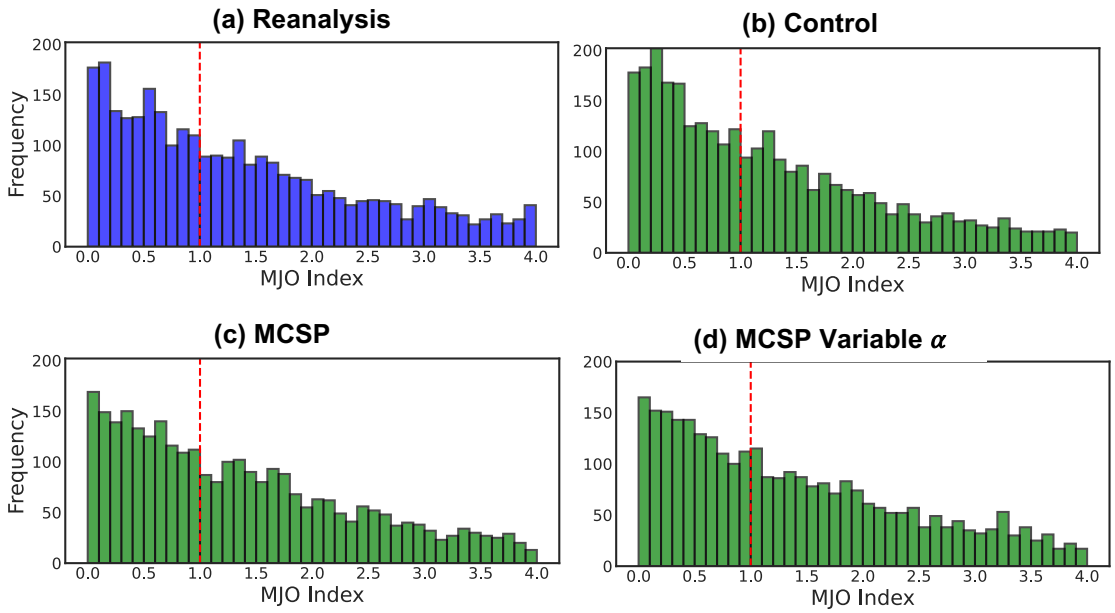

Figure S4. MJO index histogram distribution in (a) reanalysis data, (b) the control run, (c) the PRIME-MCSP run, and (d) the PRIME-MCSP variable α run. All simulations and reanalysis span September 1988 to August 2008.